2020

Development of single-particle counting assays with interferometric reflectance imaging

BOSTON UNIVERSITY

COLLEGE OF ENGINEERING

Dissertation

DEVELOPMENT OF SINGLE-PARTICLE COUNTING ASSAYS WITH INTERFEROMETRIC REFLECTANCE IMAGING

by

FULYA EKIZ KANIK

B.S., Middle East Technical University, 2009
M.S., Middle East Technical University, 2012
M.S., University of Massachusetts Lowell, 2015

Submitted in partial fulfillment of the

requirements for the degree of

Doctor of Philosophy

2020

Approved by

First Reader

M. Selim Ünlü, Ph.D.
Professor of Electrical and Computer Engineering
Professor of Materials Science and Engineering
Professor of Biomedical Engineering
Professor of Physics

Second Reader

Anna K. Swan, Ph.D.
Associate Professor of Electrical and Computer Engineering
Associate Professor of Materials Science and Engineering
Associate Professor of Physics

Third Reader

Chen Yang, Ph.D.
Associate Professor of Electrical and Computer Engineering
Associate Professor of Materials Science and Engineering
Associate Professor of Chemistry

Fourth Reader

Marcella Chiari, Ph.D.
Senior Research Scientist
Institute of Chemistry of Molecular Recognition
National Research Council of Italy
Milan, Italy

Be kind, for everyone you meet is fighting a hard battle.

John Watson (aka Ian MacLaren)

DEDICATION

Dedicated to

Arya Kanik

ACKNOWLEDGMENTS

I am deeply grateful to my advisor, Prof. M. Selim Ünlü, for taking me into his lab, patiently teaching me and supporting me for my entire time at Boston University. His trust and insight have helped me grow and become the engineer I am today. His enthusiasm and encouragement always inspired me, which I will take as an example in my future career. He went above and beyond what was required of him and supported me throughout the hardest times of my life during the last years of my Ph.D.. I cannot express enough my gratitude and respect for him.

I would like to thank my committee members, Prof. Anna Swan and Prof. Chen Yang. They helped guide my research in the right direction.

I want to thank my committee member, Dr. Marcella Chiari, for providing me with the great opportunity to work on a collaborative research project through which I gained extensive knowledge and experience. I am grateful for her guidance, insightful comments and immediate answers to my questions whenever I needed help.

I also would like to thank our collaborators Dr. Kahraman Tanriverdi and Prof. Jane Freedman. They provided me the resources, support and expertise to complete the research on microRNA studies.

I thank my current and former lab mates without whom none of this would have been possible. I couldn't have asked for a better and more supportive lab. I would like to especially thank to Dr. Derin Sevenler who mentored me when I first joined the lab and helped me throughout my research years. I am grateful to have colleagues that made our lab such a great workplace. I would like to thank Dr. Steve Scherr, Dr. Oguzhan Avci, Dr.

Jacob Trueb, Dr. Ayca Yalcin Ozkumur, Celalettin Yurdakul, Negin Zaraee, Allison Marn, Elisa Chiodi, Matthew Geib and Iris Celebi for their friendship, support, help and making working long hours in the lab fun. I want to especially thank Dr. Nese Lortlar Ünlü for her support, encouragement, sister-ship, delicious foods, hospitality, generosity and providing us a family-like environment.

I would like to thank my parents, Emine and Ahmet, for their constant support throughout my education. None of this would have been possible without the support of my parents. They deserve special thanks for invaluable help during our hardest times and taking care of Arya in the most needed times. Thank you for being always there for me and always trusting me. Arya couldn't ask for a better grandma and grandpa. I am the luckiest to have you.

Most of all, I thank my dear husband, Zafer, for his patience, endless love and devotion and making this journey much more enjoyable. I would not have made it this far without my husband and my parents.

Lastly, I thank my daughter, Arya, for making me a stronger and better version of me. I cannot imagine life without you anymore. Thank you for being my sunshine.

DEVELOPMENT OF SINGLE-PARTICLE COUNTING ASSAYS

WITH INTERFEROMETRIC REFLECTANCE IMAGING

FULYA EKIZ KANIK

Boston University, College of Engineering, 2020

Major Professor: M. Selim Ünlü, Ph.D., Professor of Electrical and Computer Engineering, Professor of Materials Science and Engineering Professor of Biomedical Engineering, Professor of Physics

ABSTRACT

Biomarkers are biological measures used for clinical assessment, whether an individual has a particular medical condition or to monitor and predict health states in individuals. Sensitive detection and quantification of various biomarkers are essential for disease diagnostics. The majority of biomarker-based diagnostics examines the presence and quantity of a single biomarker. Since the symptoms of many diseases are alike, multiplexed biomarker tests are highly desirable. Furthermore, detection of multiple biomarkers would improve the accuracy of diagnosis as well as providing additional information about the prognosis. Microarray platforms have the potential for higher level of multiplexing for biomarker detection. However, conventional microarray technologies are limited by the sensitivity of assays. This dissertation describes how single-particle interferometric reflectance imaging sensor (SP-IRIS) overcomes the sensitivity issues in biomarker detection and its applications to biomolecular and cellular biomarker detection assays.

SP-IRIS provides optical detection of individual nanoparticles when they are captured onto a simple reflecting substrate, providing single-molecule sensitivity. This technique can be

used to detect natural nanoparticles (such as viruses) without labels as well as molecular analytes (proteins and nucleic acids) that are labeled with metallic nanoparticles. Moreover, the advancements in technology make SP-IRIS ideal for the detection of low abundance biomarkers.

Utilization of light polarization in combination with plasmonic gold nanorods as labels enhances the signal-to-noise ratio in nanoparticle detection allowing for the use of low numerical aperture optics increasing the field-of-view, hence, the throughput and sensitivity. Additionally, the integration of a disposable microfluidic flow cell and dynamic particle tracking in kinetic measurements provide a robust, ultra-sensitive and automated diagnostic platform.

This dissertation focuses on the development of biological assays demonstrating effective use of SP-IRIS as a clinical diagnostic platform. We discuss the development of protein, nucleic acid and biological nanoparticle detecting SP-IRIS microarrays. We demonstrate four digital detection platforms for Hepatitis B, microRNA, rare mutations in an oncogene, *KRAS*, and virus-like particle detection with ultra-high sensitivity.

TABLE OF CONTENTS

LIST OF TABLES

LIST OF FIGURES

LIST OF ABBREVIATIONS

Anti-EBOV	Antibody against Ebola virus
Anti-HBcAg	Antibody against hepatitis B core antigen
AR	Anti-reflection
BNP	Bio-nanoparticle
CCD	Charge-coupled device
CMIA	Chemiluminescent microparticle immunoassay
CMIA	Chemiluminescent microparticle immunoassays
CMOS	Complementary metal oxide semiconductor
COC	Cyclic olefin copolymer
CV	Coefficient of variation
DI	Deionized water
DNA	Deoxyribonucleic acid
dsDNA	Double-stranded deoxyribonucleic acid
ECLIA	Electrochemiluminescence immunoassays
ELISA	Enzyme-linked immunosorbent assay
FDA	U.S. Food and Drug Administration
FOV	Field of view
FWHM	Full width at half maximum
GNR	Gold nanorod
HBsAg	Hepatitis B surface antigen
HBV	Hepatitis B virus

HepB	Hepatitis B
HRP	Horseradish peroxidase
IRIS	Interferometric reflectance imaging sensor
K_d	Dissociation constant
LED	Light emitting diode
LOD	Limit of detection
mAbs	Monoclonal antibodies
MEIA	Microparticle enzyme immunoassays
miR	microRNA
miRNA	microRNA
mRNA	Messenger RNA
NA	Numerical aperture
NAT	Nucleic-acid amplification test
OPD	Optical path difference
PBS	Sodium phosphate buffer saline
PCR	Polymerase chain reaction
POC	Point of care
PSA	Pressure sensitive adhesive
RIA	Radioimmunoassays
RNA	Ribonucleic acid
SDS	Sodium dodecyl sulfate
Si	Silicon

SiO_2	Silicon dioxide
SNR	Signal-to-noise ratio
SP-IRIS	Single-particle interferometric reflecting imaging sensor
SPR	Surface plasmon resonance
SPRi	Surface plasmon resonance imaging
SSC	Saline sodium citrate
ssDNAs	Single-stranded deoxyribonucleic acid
TBST	Tris-buffered saline, 0.1% Tween 20 surfactant
TSV	Through-silicon-via
VLPs	Virus-like particles
WHO	World Health Organization

1 CHAPTER ONE INTRODUCTION

COVID-19, an infectious respiratory disease caused by the coronavirus SARS-CoV-2, has spread globally and become a global pandemic in just over two months since its discovery in December 2019 [1]. During the COVID-19 outbreak, more than fifteen million people were infected worldwide as of 25 July, 2020 [2]. The development of therapeutics, vaccines, as well as reliable, widespread, and efficient diagnostics, became crucial more than ever. Researchers worldwide have put an immense amount of work into identifying the virus and sequencing its genes [3,4]. Currently, there are no therapeutics or vaccines approved by the United States Food and Drug Administration (FDA) [5]. At this point, diagnostics come into play with a more potent role since they can provide rapid implementations of control measures. Therefore, every day more and more testing has been performed.

Emerging diagnostics being developed for SARS-CoV-2 or other viruses mainly include detection of viral nucleic acid, viral protein antigens and antibodies, and viral particles [6–8]. These biological markers are defined as a subcategory of medical signs or indications of medical state observed from outside the patient [9]. Biomarkers are measurable changes in biological substances associated with normal or abnormal biological processes [10]. They can be cellular (viral or bacterial particles) or molecular (DNA, RNA, protein, metabolites). The very first step in diagnostics is the identification of one or more biomarkers for the particular biological process. Then, the diagnostic tools are developed for sensitive and specific detection of the particular biomarkers.

Proteins reflect the physical conditions of their environment. Since many

physiological changes are effective post-transcriptionally, their impact is not seen at nucleic acid level. Hence, proteins are more adaptive and dynamic in cellular physiology [11]. Proteomics has been used to search for novel biomarkers in biological fluids using protein and peptide profiling [12]. Protein biomarkers are crucial in diagnosis and prognosis of diseases since they actively respond to the critical changes in the body. Protein biomarker tests rely largely and most commonly on specific antibody-antigen detection which is an important subset of protein interactions.

Nucleic acid biomarkers are useful indicators for early diagnosis of cancer, infectious diseases and many other diseases. The ultra-low abundance of nucleotide biomarkers and genetic similarities make their detection extremely difficult. Additionally, detecting rare mutations ($1:10^3$ to $1:10^6$) requires exquisite discrimination between two highly similar sequences, one of which is significantly more abundant than the other.

Biological nanoparticles such as viruses and exosomes are essential cellular biomarkers for a range of medical conditions. Along with the infectious diseases, viruses are considered to be linked with many human cancers. Although the specific mechanisms leading to cancer subsequent to a particular viral infection with the particular viruses are not always clear and established, usually, a single virion is found to be responsible [13]. Using viral particles as biomarkers is advantageous because a more accurate detection free of manipulation can be obtained in their innate environment such as in serum or other bodily fluids without altering the physiological conditions. Biological sensors that detect cellular biomarkers with high specificity, without additional labeling, are promising because they reduce the complexity of sample preparation and may improve measurement quality by

retaining information about the nanoscale physical structure of the bio-nanoparticle (BNP). Figure 1.1 represents a general overview of aforementioned and additional biological materials while comparing them in terms of size. It provides broad visualization the biomarkers and their comparison with other materials.

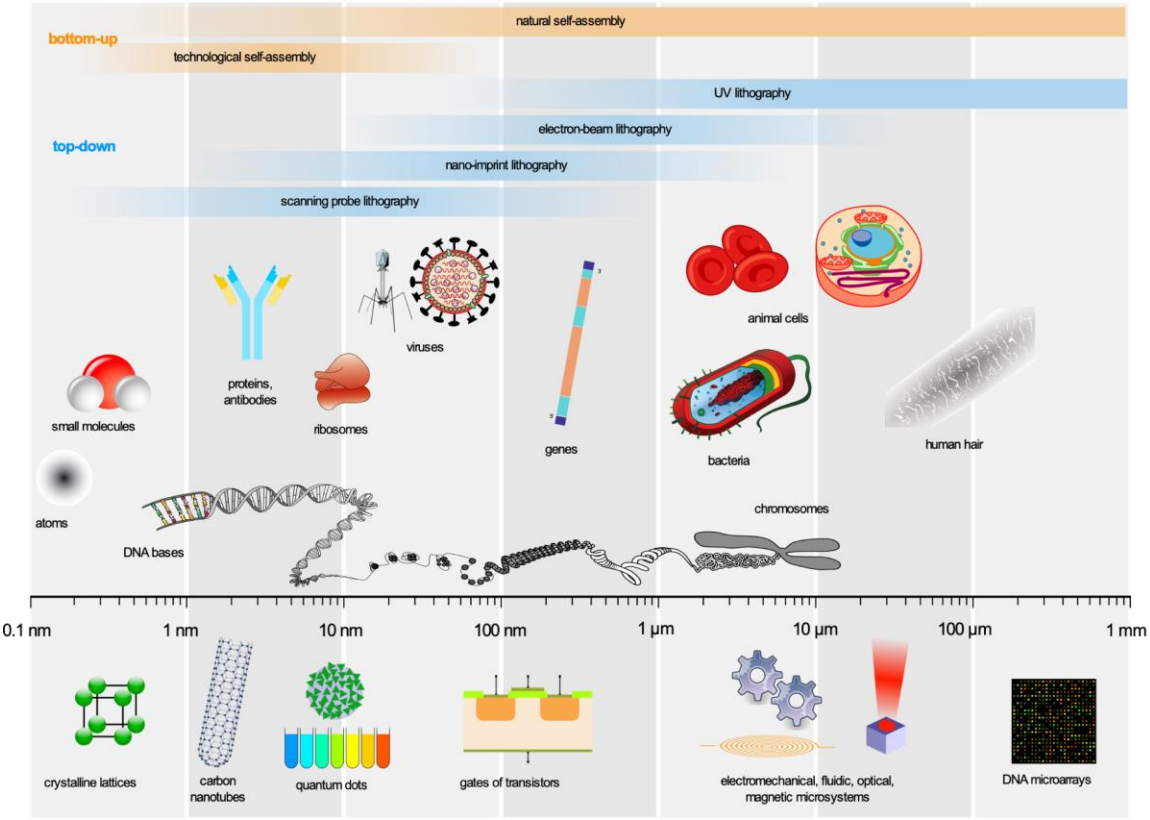

Figure 1.1 Comparison of biological and technological scales. Reproduced from [14].

The development of sensitive and easy to use platforms for the rapid detection of wide varieties of analytes such as proteins, nucleic acids, biological nanoparticles has been increasingly important in medical and environmental analysis. High-throughput screening methods in array technologies, molecular diagnostics, proteomics, infectious disease detection and drug discovery have been explored extensively [15–19]. For medical

diagnosis, it is critical to detect these biomarkers at very low concentrations. Therefore, sensitive detection of analytes is required for diagnostic tools. Microarray-based detection technologies offer the promise of highly multiplexed analysis of biomarkers if the low-sensitivity issues are resolved [20].

Interferometric Reflectance Imaging Sensor (IRIS), developed by our group, is a label-free, high-throughput and sensitive technique for the detection of variety of biomarkers. IRIS has demonstrated high-throughput detection and quantification of protein-protein binding, DNA-protein binding and DNA-DNA hybridization with high sensitivity and reproducibility [21–26]. IRIS in high-magnification modality, Single-Particle Interferometric Reflectance Imaging Sensor (SP-IRIS), is a simple, sensitive and multiplexed diagnostic platform based on detection of single particles [27,28]. Multiplexed and sensitive detection ability, microfluidics compatibility in combination with kinetic measurements make SP-IRIS a promising approach for a rapid detection platform. Recent significant advancements in SP-IRIS technology have allowed us to identify individual captured nanoparticles and digitally count the absolute number of nanoparticles captured onto a microarray [29].

Here we describe the development of a digital microarray approach that detects single-particles with high sensitivity allowing the application in multiplexed biomarker detection. This dissertation focuses on the applications of polarization enhancement of SP-IRIS expanding upon its current capabilities and applying it to different assays. We have developed highly sensitive, multiplexed, medically-relevant assays using SP-IRIS for protein, DNA and biological nanoparticle detection.

1.1 Overview of the dissertation

In this dissertation, we present development of four digital microarrays for protein, RNA and DNA, and BNP diagnostics.

Chapter 2 presents the optical system design and the data analysis techniques utilized in this dissertation. The Interferometric Reflectance Imaging Sensor (IRIS) for both biomass quantification and single-particle detection are described in detail. We further discuss sensitivity improvement with the polarization enhancement in SP-IRIS and the use of gold nanorods as the labels. Then, we explain how we do kinetic measurements and detection and tracking of each binding event during the experiments in real-time.

Chapter 3 focuses on the properties of a proper surface design for microarray applications and how we expand this knowledge in our digital microarray preparation. We further discuss the technologies that enabled sensitive kinetic measurements of nanoparticle binding and debinding. These are disposable microfluidic flow cell compatible with SP-IRIS chips and the custom software that performs nanoparticle detection and tracking in kinetic studies.

Chapter 4 describes a digital protein microarray for Hepatitis B (HepB) detection. We present a homogeneous detection approach where HepB viral antigen is mixed with antibody-conjugated gold nanorods and used in detection. The microarray yields ultra-high sensitivity for HepB detection in under an hour.

Chapter 5 expands the application of polarization-enhanced SP-IRIS to RNA and DNA detection. In the first section of the chapter, we present a digital microarray for small, non-coding RNA, microRNA, detection with attomolar sensitivity. We compare endpoint

and kinetic measurements where we utilize dynamic tracking technology mentioned in Chapter 2. We obtain an ultra-sensitive and multiplexed digital microarray for two types of miRNAs. In the second section of the chapter, we demonstrate a digital microarray for rare mutation detection in the gene responsible for colorectal cancer. We present preliminary results and suggest that polarization-enhanced SP-IRIS equipped with dynamic tracking technology is a promising approach for rare mutation diagnostics.

Chapter 6 focuses on the design aspects of solid-phase optical sensors for sensitive and label-free detection of biological nanoparticles. We apply SP-IRIS technology to the development of an assay for the detection of virus-like particles (VLPs).

Chapter 7 concludes the dissertation and presents the future work.

2 CHAPTER TWO THE INTERFEROMETRIC REFLECTANCE IMAGING

In this chapter, we describe the optical systems used throughout this dissertation. First, we explain the low magnification modality, IRIS, which is a multiplexed and label-free detection platform. IRIS is used to quantify biomass accumulation on a substrate. Second, we explain the high magnification modality, SP-IRIS, which is used for quantitative detection of single nanoparticles, particularly gold nanoparticles and biological nanoparticles which are selectively captured on the sensor surface. We present an overview of the two detection techniques, image analysis and data processing. Finally, we describe real-time tracking and detection of single nanoparticle binding during kinetic binding experiments.

2.1 Interferometric reflecting imaging sensor (IRIS)

Interferometric reflectance imaging sensor (IRIS) is a label-free biosensor that measures the optical path difference (OPD) as a result of biomass accumulation on the sensor surface. A silicon/silicon dioxide (Si/SiO_2) layered substrate is used to prepare the microarray format sensors [27].

2.1.1 Detection principle

The IRIS system depends on the interference of the normally incident electromagnetic waves on the layered substrate. An overview of the IRIS system, a typical IRIS image and height maps of some selected spots are shown in Figure 2.1. The layered substrate consists of a silicon wafer with a thermally grown silicon oxide layer on top (110 nm in thickness). Normally incident light from an LED is reflected from the both layers of

the Si/SiO_2 substrate. The reflectivity curves are fitted to spectral reflectance using the Fresnel equations as given below. The reflection coefficient of an oxide can be approximated as:

$$R = |r|^2 = \frac{r_1^2 + r_2^2 + 2r_1 r_2 cos2\phi}{1 + r_1^2 r_2^2 + 2r_1 r_2 cos2\phi} \quad (2.1)$$

where r_1 and r_2 are the Fresnel reflection coefficients of air, silicon dioxide and silicon, respectively. They can be calculated as

$$r_1 = \frac{n_2 - n_1}{n_2 + n_1} \quad (2.2)$$

and

$$r_2 = \frac{n_3 - n_2}{n_3 + n_2} \quad (2.3)$$

where n_1, n_2, n_3 are the indices of refraction for medium, silicon dioxide and silicon, respectively.

The optical phase difference between the two reflected waves from medium/SiO_2 and Si/SiO_2 interfaces are indicated with ϕ in Equation 2.1 which is given by

$$\phi = \frac{2\pi d}{\lambda} n_2 cos\theta \quad (2.4)$$

where λ is wavelength of the incident light, θ is the angle of incidence and d is the thickness of transparent film which is the biofilm layer with SiO_2.

The surface of the substrate is functionalized with biomolecules which are used as capture probes for the analyte of interest. During the binding experiments, the sensor is incubated with the analyte solution and the target (analyte) molecules bind to the sensor surface via capture probes, which creates a biomass accumulation. This accumulation

changes the OPD between the top of the transparent film and the top of the Si surface. A thicker transparent film results in a higher OPD, which appears as a characteristic and quantifiable shift in the spectral reflectivity curve along with the change in the intensity of the reflected light at the specific wavelength (Figure 2.1C).

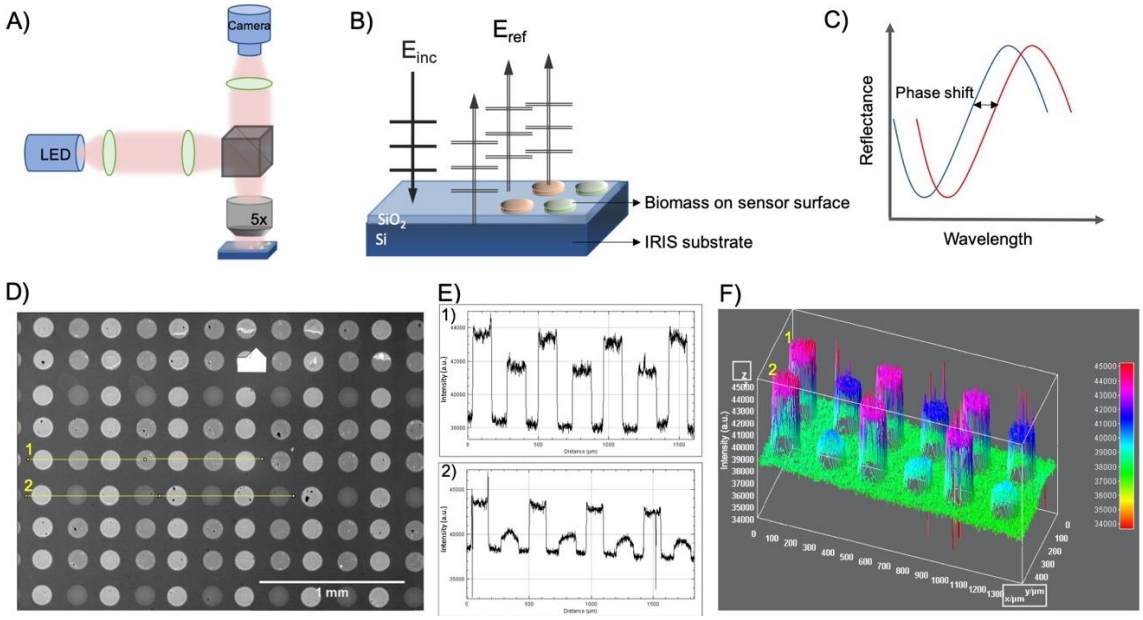

Figure 2.1. A) Schematics of the IRIS optical setup. B) Operating principle of IRIS showing the illumination of the Si/SiO2 substrate and the reflected light from the surface of different layers of the substrate along with the biomass on the surface. C) The phase shift detected at the camera as a result of accumulation. D) A typical IRIS image of the sensor surface with an array of antibody spots. E) Height profiles along the lines (1) and (2) in Figure 2.1.D. Antibodies at different concentrations create different heights, so do variations in the intensity at the camera yielding different gray values, as shown in the height profiles. F) 3D surface map of spots marked with the lines in Figure 2.1.D.

Equation 2.1 provides the OPD from spectral reflectivity at each pixel in the image. As the biomass accumulates on a given spot, the OPD changes. It is approximated that the refractive index of the accumulated protein is roughly equivalent to the SiO_2 layer [30].

The OPD is then used in the calculation of the thickness of the transparent film, assuming a constant refractive index through the biofilm layer and SiO2 which is taken as 1.45. Therefore, the effective thickness and concentration of the accumulated biomaterial concentration can be estimated in nanometers and ng/mm^2 on a given spot, respectively. Quantification experiments were performed by our group [31]. A known amount of DNA and protein molecules were deposited on the sensor surface and measured by the IRIS system where a conversion is generated. The conversion factors are for IgG 1nm = 1.2 ng/mm^2 and for DNA molecules 1nm = 0.8 ng/mm^2.

2.1.2 Data collection, image analysis and data processing

The optical setup fundamentally contains LEDs, an integrating sphere, a 50:50 beam splitter, an objective, a camera. Four-color LEDs are attached to the integrating sphere to obtain a uniform illumination source (low spatial coherence). The four colors are red (dominant wavelength, λ_D = 630 nm), green (λ_D = 525 nm), blue (λ_D = 460 nm), and yellow (λ_D = 595 nm). A 5X/0.15 NA objective (Nikon) is typically used. 5 MP CMOS camera (FLIR, Grasshopper3 GS3-U3-51S5M-C) with a pixel size of 3.45 μm is used for data collection. The low-magnification modality of IRIS provides a large, 2.8 mm x 2.1 mm field of view (FOV) using a 5x magnification with 0.15 numerical aperture (NA), making the technique very appealing for multiplexed applications.

The reflected light intensity measured at the camera is recorded for each pixel at the camera for each illumination wavelength. The intensity data is then processed by using custom MATLAB software, where the intensity values at each wavelength are normalized and fitted to a reflectivity curve for each pixel using Equation 2.1. For this, the thickness

of the transparent film is calculated. The thickness values of each pixel are mapped to a grayscale image (Figure 2.1).

Recently, IRIS has evolved into a more powerful detection technology for label-free biomolecular interaction analysis with 2x magnification, larger FOV of 7mm x 5 mm, automated sample handling and Python-based, user-friendly detection and analysis software.

The IRIS is used for quantification of DNA, protein adsorption on the surface, real-time monitoring of binding events, measuring binding rates and as a quality control step in microarray fabrication. Since the IRIS imaging platform can provide label-free and multiplexed quantification of molecular binding events in real-time, it is a versatile technique for many applications [32–34].

2.2 Single-particle interferometric reflecting imaging sensor (SP-IRIS) – Digital detection of single nanoparticles and kinetic measurements of nanoparticle binding

Single-particle interferometric reflecting imaging sensor (SP-IRIS) is adapted from the low magnification modality of IRIS. It advances the wide-field interferometric imaging to high spatial resolution with the help of a high-NA objective. It is used for detection of biological and synthetic nanoparticles on the sensor surface. In this modality, the signal stems from not only the interference of the light reflected from the layered substrate and the biological layer, but also the interference between the scattered field from the particle and the light reflected off the substrate. The instrument can be used to count individual nanoparticles captured on the sensor over a large sensor area [25,26,35]. SP-IRIS is a very

powerful tool for detection of both biological nanoparticles, such as viruses, and synthetic nanoparticles, such as gold nanoparticles, in a microarray format [24,36]. The ability to detect individual particles as well as quantify makes it attractive for clinical and research applications. Moreover, the system can be used in labeled and label-free form. Even though biological nanoparticles such as viruses are low in contrast and small in size, SP-IRIS performs sensitive detection of whole viruses from serum and blood samples as a label-free platform [37]. On the other hand, DNA or protein molecules can be labeled with gold nanoparticles so that they can be captured and counted on the sensor surface using SP-IRIS with the help of nanoparticle labels [23]. Besides, SP-IRIS can be used in a multiplexed manner in which multiple targets can be detected at the same time on the same microarray thanks to its large field of view and high enough sensitivity.

SP-IRIS is also used to measure binding kinetics. Quantifying the binding events on the sensor in a dynamic context is of high importance in many applications. For instance, in low-affinity binding events, performing measurements in real-time is advantageous since it is hard to detect the bound analyte present (before they debind) on the surface at any time of the assay. However, the ability to measure the binding events as they occur provides the possibility of actually counting the events and gives plenty of information about the nature of the bindings, such as dwell time. Most commonly, fluorophores, as labels, and fluorescence-based systems are used for quantifying biological markers and molecular interactions. However, such dynamic experiments cannot be performed with fluorescence-based systems due to the bleaching problems and excess signal coming from uncaptured fluorophore-labeled analytes flowing in the reaction chamber which masks the

signal coming from captured analytes on sensor surface. SP-IRIS can perform all these measurements in a multiplexed array format allowing many different probe-target interactions to be investigated in parallel, real-time and dynamically.

2.2.1 Detection principle

As in IRIS, SP-IRIS also uses a silicon substrate with a thin film of thermally grown oxide in 110 nm thickness. When a nanoparticle is on this substrate, the light scattered from the nanoparticle is interferometrically enhanced due to two reasons (Figure 2.2B). First, the light scattered from the particle in the forward direction (towards the substrate) is reflected by the layered substrate interface at silicon/silicon dioxide which then propagates back towards the detector along with the back-scattered light (towards the detector) where they interfere. Second, the total scattered-light and the reference reflected field interfere at the detector which creates an intensity pattern; hence, this is measured in the camera.

An interference pattern for a nanoparticle on a reflective surface is approximated as below

$$|\mathrm{E_{sca}} + \mathrm{E_{ref}}|^2 \cong |\mathrm{E_{sca}}|^2 + |\mathrm{E_{ref}}|^2 + 2|\mathrm{E_{sca}}||\mathrm{E_{ref}}|\cos\phi \quad (2.5)$$

where E_{sca} and E_{ref} are the scattered and reference fields, respectively and ϕ is the phase difference between the scattered and reference fields.

In a case where there is a large particle which is larger than the illumination wavelength, then its appearance is determined by the intensity of the scattered field, $|E_{sca}|^2$ in the image. In this case, the intensity of the field is scaled with the square of the particle volume. However, when smaller nanoparticles are imaged, since the size of the scattering particle goes down around half the wavelength of the illumination light, then, the visibility

of directly scattered light drops drastically. It becomes almost indistinguishable from the background and very difficult to detect with a non-interferometric imaging system. However, utilizing interferometric enhancement, as shown in Equation 2.5, the recorded intensity at the camera is dominated by the cross (interference) term which stems from the interference of scattered field with the reference field—the cross-term scales linearly with the particle volume [38]. As a result, by detecting this interferometric component, it is possible to detect nanoparticles that are much smaller than what would be possible using only scattered field alone.

With this approach, SP-IRIS can detect individual, low contrast, non-resonant particles in a multiplexed and label-free fashion [25]. For detecting biological nanoparticles, such as viruses, a microarray of capture probes is prepared on the SP-IRIS substrate to capture the target nanoparticles selectively. The biological nanoparticles are challenging to detect due to their small size and low-index difference with the surrounding medium. When biological nanoparticles bind to the surface, scattered light from the particles interfere with the reference field reflected from the layered substrate, which is the enhanced signal that is being detected at the camera. As a result, the captured biological nanoparticles appear as diffraction-limited dots on the image.

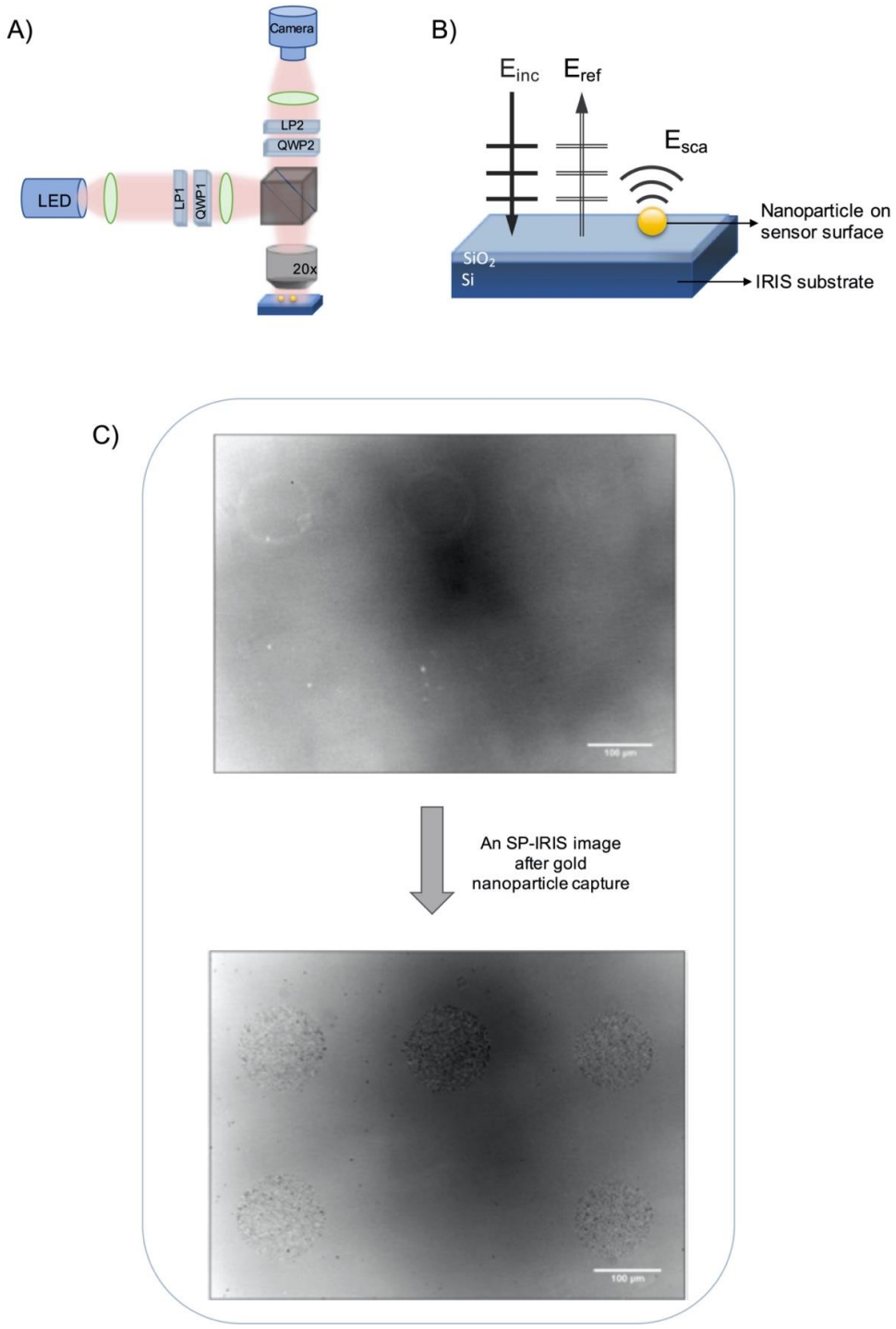

Figure 2.2 A) Schematics of the SP-IRIS optical setup. B) Operating principle of SP-IRIS showing the illumination of the Si/SiO_2 substrate and the reflected light from the surface of different layers of the substrate along with the nanoparticle scattering. C) A typical higher magnification IRIS image before (left) and after (right) nanoparticle incubation. Captured nanoparticles are seen as diffraction limited dots in the image.

2.2.2 Interferometric imaging of gold nanorods and polarization-enhanced SP-IRIS

Biological nanoparticles are directly detected using SP-IRIS, as mentioned above. Most of them, such as viruses or exosomes, above 70 nm in diameter, are distinguished from the background with the interferometric enhancement. Nevertheless, many biologically exciting analytes such as proteins or nucleic acids are too small to be detected at a label-free and single molecular level. Therefore, a label is required to make them visible and detectable through imaging. Conventionally, fluorescence dyes (fluorophores) are used for this purpose. However, there are many drawbacks associated with them, such as labeling burden, bleaching, emission rate, inefficiencies in the collection of the fluorescence signal. Additionally, sensitivity is the main issue when it comes to fluorescence assays. To obtain a meaningful signal that can be detected in typical fluorescence scanners, the number of fluorophores that should come together to emit the fluorescence signal required is very high, which causes sensitivity issues while working with low abundance samples [29]. Also, visualization of individual fluorophore-labeled molecules is very instrumentation and time expensive which makes it not applicable for many applications such as high-throughput microarray assays [39]. On the other hand, single nanoparticles are excellent labels when they are used for light scattering. Unlike fluorophores, nanoparticles perform without photobleaching in light scattering. Therefore, their use as scattering labels is not surprising [23,40,41]. However, their light scattering declines considerably when nanoparticles smaller than 100 nm in diameter are used, which requires either high-magnification microscope objectives, such as 50x/0.8 NA used in [23],

to visualize individual nanoparticles or some enhancement steps where other metals (usually silver) is introduced to grow their size and scattering [40]. The SP-IRIS instrument is capable of detecting individual gold nanoparticles (of order ~40 nm) directly. In an SP-IRIS image, individual immobilized nanoparticles are visible as diffraction-limited spots. Furthermore, the instrument can detect individual binding events of each nanoparticle instead of measuring only the analog ensemble signal (Figure 2.2C).

As a nanoparticle gets smaller in size, it gets harder to image. The nanoparticle contributes to the interference cross-term in Equation 2.5 in relation to the amplitude, $|E_{sca}|$, which scales with its volume and material polarizability. As the size of a nanoparticle goes down, the strength of its interferometric signal gets smaller proportionally with its polarizability which can be expressed as

$$\alpha \cong 4\pi\varepsilon_0 r^3 \frac{\varepsilon_p - \varepsilon_m}{\varepsilon_p + 2\varepsilon_m} \tag{2.6}$$

where α is the polarizability of the nanoparticle, r is its radius and ε_p and ε_m are the permittivities of the particle and its surrounding medium, respectively [42]. The scattered intensity produces a signal proportional to $|E_{sca}|^2$ which is proportional to ${\alpha_{sca}}^2$ which is also proportional to r^6. For small nanoparticles, the scattered intensity at the detector (I_{det}) can be associated with

$$I_{det} \propto |E_{sca}|^2 \propto {\alpha_{sca}}^2 \tag{2.7}$$

Therefore, the weak signal coming from the nanoparticle disappears at the detector. As shown in Equation 2.5, the signal coming from the cross-term is proportional to r^3. Thus, by detecting the cross-term, interferometric detection enables the detection of small

particles with improved sensitivity.

In our studies, we aim to use a label which is small enough to have a favorable diffusivity in solution during the experiments in the reaction chamber, and simultaneously large enough to have a signal signature above the noise floor. Background noise floor (coming from the thickness variations in the morphology of the surface and capture probes) is in the range of 1–2%. Therefore, an ideal label would have a normalized intensity of at least 5% of the local background. Furthermore, the necessity of using a high magnification objective for imaging small nanoparticles also brings smaller FOV in detection, which makes imaging extra time consuming to image a big detection area on a sensor surface with a small FOV in the order of couple hundreds of micrometers. Therefore, having a technique where we can have small nanoparticles for better diffusivity and big enough for throughput assays is necessary for our studies. Thus, the size of the nanoparticle is a critical parameter. For this purpose, polarization-enhanced SP-IRIS has been developed in our lab to take advantage of the asymmetric scattering behavior of gold nanorods by preferentially blocking the light based on its polarization state and have a 10-fold improvement in the visibility of the nanoparticles [29]. This improvement uses rod-shaped gold nanoparticles (nanorods) to label the target analytes in our assays. This way, we are able to utilize polarization-dependent scattering properties of rod-shaped gold nanoparticles. We use 25 nm x 71 nm gold nanorods (λ_{LSPR} = 650 nm from Nanopartz^{TM}, Loveland CO) for labeling nucleic acids and proteins in our experiments. This structure of the nanorods leads to distinctive physiochemical and optical properties due to electron confinement and high surface area. When the nanorods are illuminated with a light source, the electric field causes

the oscillation of the conductive-band electrons at the surface of the particle [43]. The free electrons oscillate along both the long and short axis of the nanorod [44]. These gold nanorods possess a shorter and weaker resonance band in the absorbance spectrum which attributes to the diameter of the nanorods with an absorption peak maximum around 530 nm and possess a stronger resonance band which attributes to the length of the nanorod with an absorption peak maximum around 650 nm and is due to the plasmon oscillation of electrons along the long axis of the nanorods [45]. These two plasmon resonance wavelengths are i) the primary longitudinal plasmon scattering the light which is polarized parallel to the longitudinal axis of the rod, and ii) the transverse plasmon scattering only the light being polarized along the minor axis. The optical scattering of the gold nanorods strongly depends on the polarization of illumination. When the nanorod is illuminated at the longitudinal resonant wavelength, it scatters light 25 times stronger at a polarization state with its major axis than aligned with its minor axes [29]. Therefore, the nanorods have the ability to perturb the polarization of the light much more strongly than the background reflections. Thus, when we use a set of polarization filters, we can selectively reduce the background without affecting the scattered light.

2.2.3 Data collection, image analysis and data processing

The polarization-enhanced SP-IRIS involves the use of circularly polarized light in a quasi-darkfield configuration. The polarization-enhanced SP-IRIS employs circularly polarized illumination in a Kohler configuration, which enhances visibility. The principle of the system is to illuminate the substrate with circularly polarized light and then to use an optical filter to block the circularly polarized component in the reflected light before it

reaches to the detector. Such an optical filter can be constructed using a quarter wave plate followed by a linear polarizer in the collection path. We use a linear polarizer and a quarter wave plate in the illumination path to obtain circular polarization which are depicted as LP1 and QWP1 in Figure 2.3, respectively. The illumination light passes through the linear polarizer and the quarter wave plate, which forms a circularly polarized light to illuminate the sample after passing through the beam splitter and the objective. An analyzer consists of the same components in the collection path together to block the majority of the reference light (LP2 and QWP2 in Figure 2.3). Circularly polarized light enters the quarter wave plate (QWP2) and exits linearly polarized which then nearly entirely blocked by the linear polarizer (LP2). With circularly polarized illumination, the excitation of each nanorod is the same regardless of its surface orientation. Thus, when we use gold nanorods, nanorods scatter and absorb this light anisotropically, resulting in an elliptically polarized field which can partially pass through the analyzer. Since the collection optics are configured to (mostly) block circularly polarized light, they will not entirely block the scattered light from any gold nanorods. As a result, strongly asymmetric scattering and absorbing particles emit elliptically rather than circularly polarized light, allowing it to partially pass through the analyzer, agnostic to particle orientation. Figure 2.4 shows how the visibility of nanorods is improved with the use of circular polarization. In order to achieve visibility, exposure time is increased to 150 ms, instead of 10 ms in the case of polarization. While the use of circular polarization enhancement dramatically reduces the total amount of collected light, the visibility of surface-bound nanorods is significantly enhanced. Shot noise, variability in the reflectance of IRIS chip, stray light and camera

read noise affect interferometric sensing, which causes random variabilities. These background fluctuations cause the reflectivity of the surface change by around 0.5–1% [29]. Therefore, to be able to differentiate a particle from its background, the normalized intensity of the particle should be above 0.5–1%. By partially blocking the reference light without blocking the scattered light, the visibility of the particles can be improved. By using gold nanorods for their polarization-dependent scattering and circularly polarized illumination, we enhanced the visibility of gold nanorods.

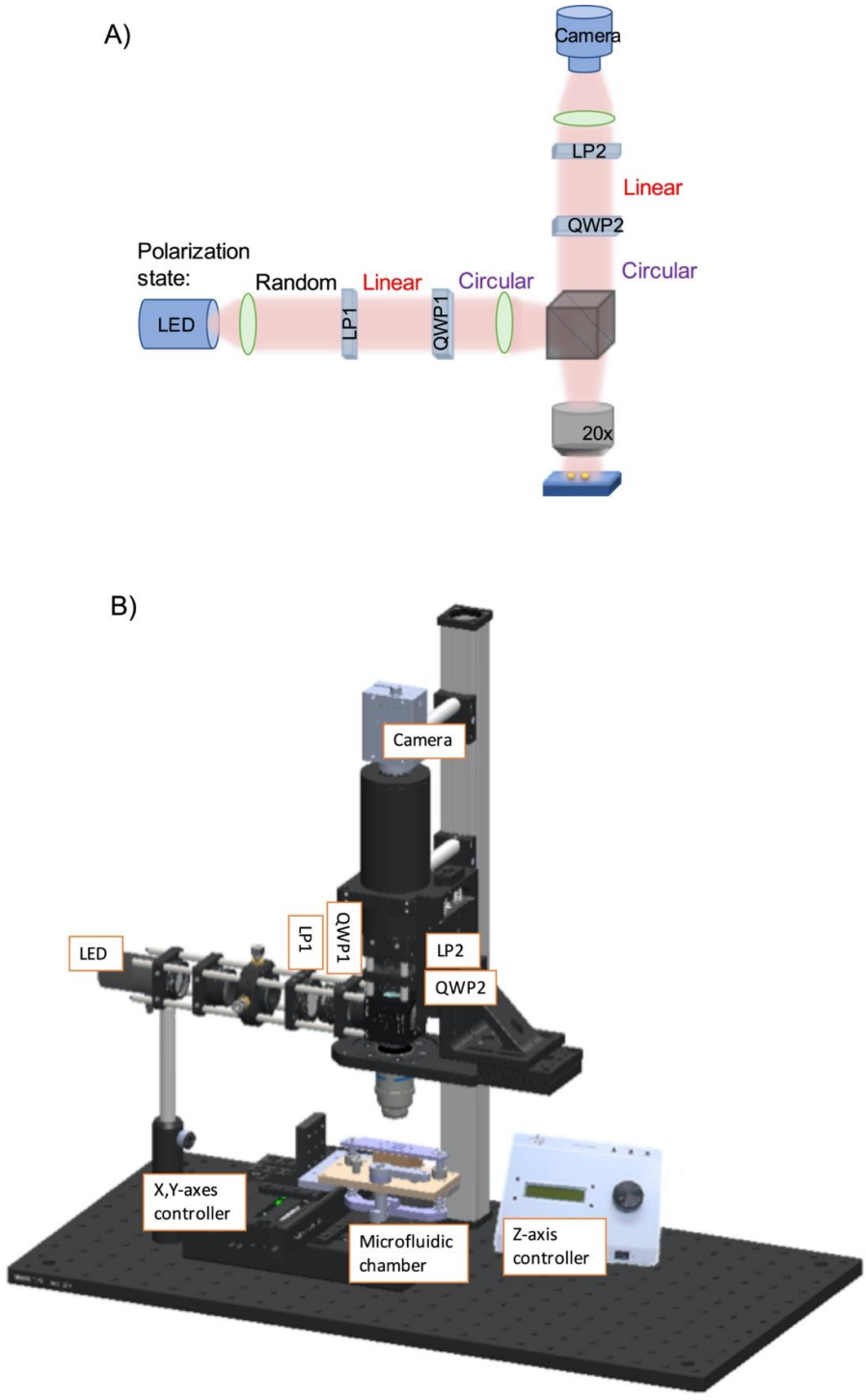

Figure 2.3 A) Schematic representation and B) render of the polarization-enhanced SP-IRIS detection instrument. The sample is illuminated with circularly polarized light, formed using a linear polarizer and quarter wave plate. An analyzer consisting of the same components blocks nearly all circularly polarized light returning from the substrate.

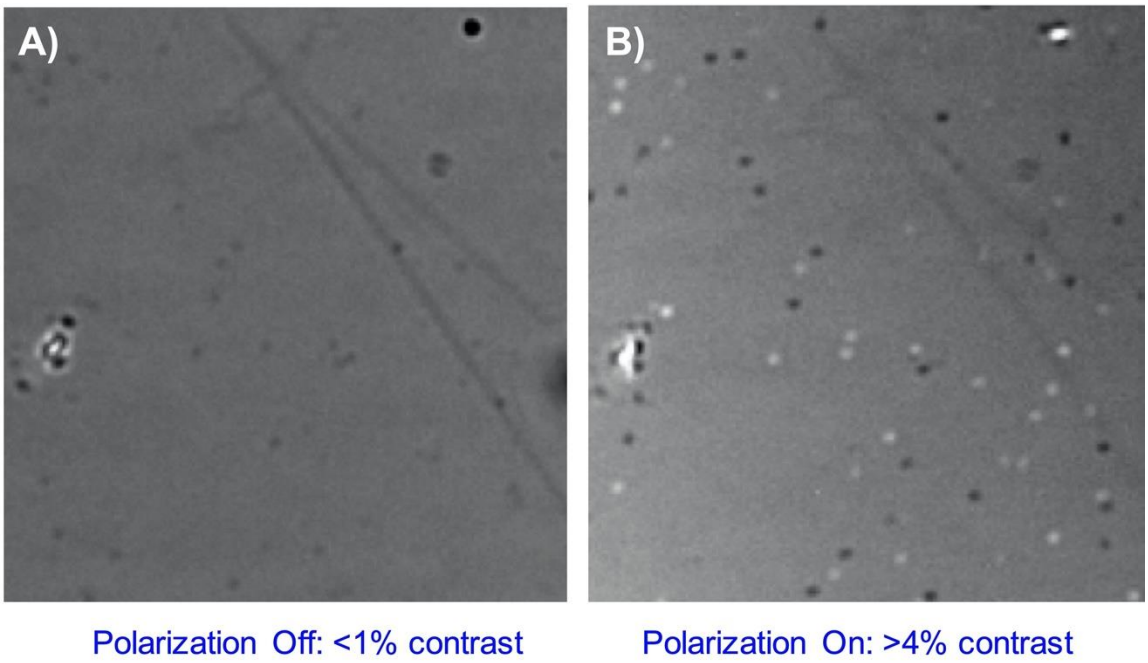

Figure 2.4 SP-IRIS images of 25 x 71 nm gold nanorods A) without circular polarization enhancement and B) with circular polarization enhancement. The visibility of surface bound nanorods is significantly enhanced. The appearance of nanorods with circular polarization enhancement is an arbitrary function of particle orientation.

In order to robustly detect all the nanorods regardless of their orientation on the surface, we use a z-stack approach previously developed for unpolarized SP-IRIS imaging [46]. The defocus problems can be because of the changes in the axial location of nanoparticles and heterogeneous defocus behaviors because of the small errors in chip alignment (on the order of tenths of a degree). Moreover, particle's orientation on the surface changes the relative phase of the scattered and reflected fields at the detector. Therefore, a phase delay will appear at the second quarter wave plate on the scattered field of the particle. Therefore, even in the same field of view, some nanoparticles can be in focus while others may be out of focus in different regions. To ensure the detection of each nanoparticle in the FOV with the optimal focus, a stack of defocus images which axially

scans the objective for 3 μm of focus positions in 250 nm increments around the nominal focus was acquired. Figure 2.5A shows a slice in this z-stack image of an antibody spot with captured 25x71nm gold nanorods (GNR) on a dry chip with the varying appearance of nanoparticles for different regions. Individual particles were registered through the stack of images over the extent of a given range of focal planes. The normalized intensities for each particle were calculated for each image in the stack. This produces a standard defocus curve representing the particles' response with respect to the change in z-location (defocus position) shown in Figure 2.5B. To do so, the center of the diffraction-limited image of each particle was identified in Figure 2.5A. The normalized intensity of the centers was measured as a function of focus position to measure experimental defocus profiles of immobilized nanorods with random orientations. The normalized intensities were calculated. Figure 2.5B shows normalized intensities for multiple particles marked in Figure 2.5A as a function of defocus. Figures 2.5C–D are the numerical simulations of gold nanorods with respect to the change in z-position. Experimental results are in good agreement with the simulated normalized intensity of 25x71 nm gold nanorods. Every particle is not visible in every focus position. For instance, the particles with the orientations at the angles 0° and 90° are not visible in the image at a given focal plane. By taking multiple images at different z positions around the nominal plane, we ensure that some signal will be collected for all labels regardless of their orientation and we are able to generate a final compressed intensity range image.

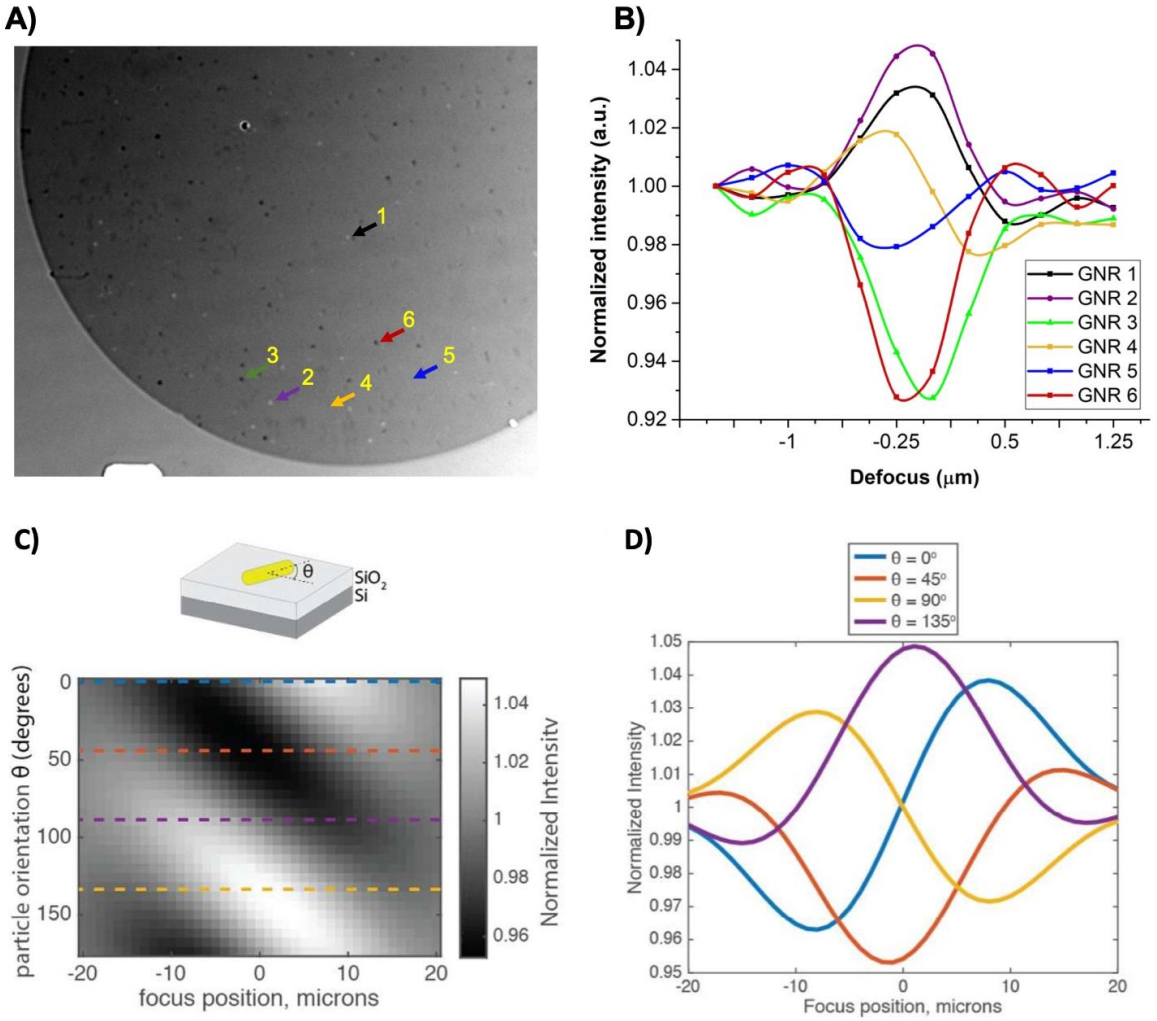

Figure 2.5 Validation of numerical simulations of gold nanorods (GNR). A) Circular polarization enhanced SP-IRIS dry images of gold nanorods on an antibody spot at a selected z-position. B) Measured normalized intensity of multiple gold nanorods marked on the image as a function of defocus. C) Simulations of normalized intensity of gold nanorods with different surface orientation angles θ=[0°,180°] as a function of defocus. D) Four simulated cross sections from (C). Figures (C) and (D) are adapted and reprinted with permission from ACS Nano 2018, 12, 6, 5880–5887. Copyright 2018 American Chemical Society [29].

Many parameters affect the optical visibility of nanoparticles on an IRIS substrate, including the particle size and elevation above the interface, immersion medium as well as collection NA and illumination wavelength. The phase difference is affected by the NA of the objective. The polarization enhancement is significant enough to enable the use of

objectives with an NA below 0.5, increasing the number of imageable microarray spots to at least nine. Polarization-enhanced SP-IRIS uses a 650 nm LED illumination source with a 10 nm FWHM bandpass filter and a low-magnification objective (20X/0.45 NA or 10x/0.3 NA) which allows for monitoring up to 12 microarray spots with 200 μm spot-to-spot distance in a single field of view (706.6 μm × 517.5 μm). A 1.1-inch format CMOS GS3-U3-123S6M-C (FLIR) monocolor camera is used to capture images of the chip. The maximum achievable optical resolution by a camera depends on the number of the photodiodes in the array and the size of the photodiodes relative to the magnified image. The equipped camera has a photodetector array of 4096 x 3000 pixels, with a pixel size of 3.45 μm. Correspondingly, when a 10x magnification objective is used, each pixel corresponds to 0.345 μm of the chip. Two samples (pixels) are required for each resolvable unit, meaning with 10x magnification, the camera can only detect features greater than 0.345 μm. Similarly, for a 20x objective, this value is 0.173 μm. With higher magnification, better resolution can be achieved; however, this results in a smaller field of view of the chip. These properties can be compared in Table 2.1 below. In order for the setup to not be limited by the capability of the camera (the electronic resolution), the optical resolution must also be considered. The Abbe resolution of the system, defined as $d = \frac{\lambda}{2NA}$, describes the optical resolution of the system. The electronic resolution should be at least equal to, or better than the optical resolution, resulting in a diffraction-limited system. Therefore, when the 10x/0.3NA objective is in use if the particles are closer than the Abbe limit (about 1.1 μm), then the particles would be indistinguishable and appear as a single diffraction-limited spot, which would cause undercounting in particle counting algorithm. Sevenler et

al. explain very well this phenomenon and the ways to overcome this limitation with the use of gold nanorods and polarization enhancement in SP-IRIS [29].

	1x	**10x**	**20x**
Projected size per pixel	3.45 μm	0.345 μm	0.173 μm
Field of view	14.1 mm x 10.3 mm	1.41 mm x 1.03 mm	707 μm x 517 μm

Table 2.1 Magnification dependency of projected size and field of view in SP-IRIS setup.

For in liquid measurements where the sensor is placed in a microfluidic chamber containing a solution and a layer of cover glass on top, a cover glass corrected objective needs to be used. The correction on the objective is used to compensate for spherical aberrations induced by the different path lengths traveled by high angle light passing through the cover glass and liquid layer. For this, a 20X/0.45 NA Nikon objective with variable aberration correction was chosen. Due to the change of the refractive index of the surrounding medium from air to buffer (from 1.0009 to 1.33–1.344) [47], the polarizability of the nanoparticles and scattering cross-section decline in liquid measurements (as in the Equation 2.6) compared to the dry chips. Therefore, scattered field diminishes drastically, so do the interferometric signal and visibility of the nanoparticles. Hence, 20x/0.45 NA objective was used in liquid measurements. Even though the nanorods are still detectable with 10x/0.3 NA objective, yet their visibility is much better with 20x/0.45 NA objective.

For data acquisition, an open-source microscope control application,

Micromanager, is utilized with custom scripts and plugins [48]. With 20x/0.45 NA objective, z-stack images were taken in 16 µm width with 2 µm increments. At each z position, four images are taken, and images are averaged to reduce the shot noise. Moreover, to further reduce the shot noise, a sparse pseudo-median filter is used to smooth the interferometric image of each frame of the z-stack. After acquiring the z-stack images via Micromanager, the image data were then processed using a custom analysis software called SPANDEX (Single Particle Analysis and Detection Experience). The application provides "digital" detection of the gold nanorods via single-particle counting. All images are normalized by the median value of all images. After determining the maximum and minimum grayscale value at each (x,y) pixel position, the difference is taken and the normalized intensity range (NIR) image is prepared. Each dot on the image are then designated as a particle. Uneven illumination, debris on the surface, or particle crowding can cause false negatives or positives. Particle detection and counting algorithm work in three steps: i) the cross-correlation of pre-processed differential image (max-min) with measured PSF of the imaging system is calculated, ii) correlation matrix is binarized with predetermined global threshold parameters to obtain keypoint candidates, iii) these keypoints are then filtered based on the size and area-to-perimeter ratio to include only the diffraction-limited spots. Note that the thresholding parameters for filtering correlation image and keypoints are manually obtained by hand-tuning once and then the same parameters throughout in all images. Figure 2.6A shows a typical SP-IRIS raw image of twelve DNA spots obtained with 20x/0.45 NA objective from an in-liquid experiment (before processing). Figure 2.6B shows a close-up image of one of the spots with captured

gold nanorods. Figures 2.6C and D are the processed images using SPANDEX and obtaining NIR difference image, respectively.

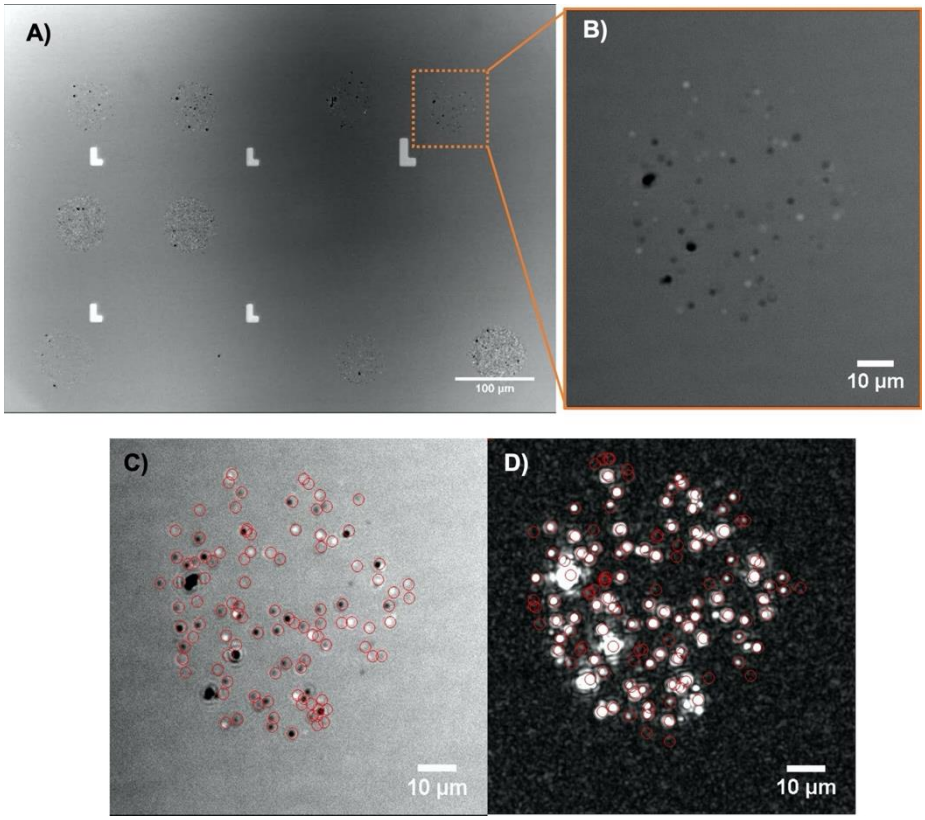

Figure 2.6 SP-IRIS image acquisition and processing. A) A typical SP-IRIS raw image of twelve DNA spots obtained with 20x/0.45 NA objective from an in-liquid experiment before processing, B) a close-up image of one of the DNA spots on the chip with captured gold nanorods. C) SPANDEX is used to detect the gold rods and D) NIR image is used to detect the locations of each gold nanorods.

2.2.4 Kinetic measurements of nanoparticle binding and real-time detection

The aim in binding assays is to evaluate the interactions between two molecules, such as DNA-DNA interaction, protein-protein interaction or antibody-antigen interaction. Measuring binding kinetics is always challenging due to variability in affinities and the low abundance of the target molecules in the sample. There are two critical components in

measuring affinities in binding assays: i) the reaction must be at equilibrium during the actual measurement, ii) concentration of one reactant (analyte) varies during the measurements. Therefore, an ideal binding assay must be responsive and sensitive enough to all these dynamic changes. Binding kinetics is usually measured while the biosensor is still immersed in a solution, while the assay is progressing. There are a couple of advantages of performing these measurements in liquid. First, drying out the substrate may result in irreversible biomolecular binding. Second, the morphology of biological nanoparticles, such as virus or exosome, may change if they are dried. Third, while drying the sensor, debris from solution i.e., salt or protein residue from buffers or serum, may stay on the surface which then may cause false negatives or positives in the detection of the actual target molecules on the sensor surface. In order to prevent all these sources of variability and acquire the data while the assay is running in 'real-time', in-liquid imaging is crucial. SP-IRIS enables imaging and kinetic measurements of binding and debinding of individual nanoparticles for molecular affinity measurements. With SP-IRIS, we can track the interaction between biological nanoparticles or target molecules, which are labeled with gold nanorods, and capture molecules on the sensor surface. Even if the interaction is weak, via real-time measurements, we can image the sensor surface throughout the measurements; hence, be much more sensitive than 'endpoint' measurements and observe how long the interactions last on the surface between target and capture molecules.

The experiments require a flow cell for dynamic reactions. The microfluidic chamber and assay design are detailed in Chapter 3. Mainly, dynamic detection is performed in a custom-designed fixture holding IRIS chip and an antireflection-coated

cover glass window on top. In typical binding assays, the IRIS chip is placed in the microfluidic chamber which is connected to a syringe pump. The analyte solution is injected into the chamber while recording the binding of the analyte. A flow rate of 2 µL-10 µL is used during the experiments. At each time point, a z-stack is recorded. Each time point is effectively a single stack of the entire field of view. During the time course of the experiment, a sequential series of image stacks are collected and used to create an hyperstack with time and z-position dimensions. Images acquired every 30 seconds during perfusion. Nanorods are visible as small, faint, diffraction-limited dots in the images which are detected in each frame independently using the custom software.

Kinetic measurements are done in two parts in our dynamic binding assays. First, detection of each binding event in each frame of the image stack is done, where the software detects the location of each nanoparticle. Second, tracking is done by following each bound nanoparticle overtime in consecutive images in the rest of the stack. This allows us to detect each particle digitally on the surface and track each and every binding event during the experiment. The main advantage of this technique is that it enables the detection of ultralow concentration by making it possible to visualize and detect binding-debinding events and short residential times of low-affinity analytes. Moreover, it makes it possible to measure both binding-debinding rates for given weakly-binding analyte-surface probe pair in the experiments. There are four major issues in end-point measurements or real-time with no-tracking assays while working with low affinity and low abundance samples. First, since the affinity is low, the dwell time of the target molecules is short after captured on the surface with surface probes. Therefore, at the end of the experiment, by chance,

there might not be any analyte bound on the surface. However, if tracking and detection are done in real-time, then, binding, short interaction period, and the analytes leaving from the surface can be captured in the real-time detection and assay can be successful. Moreover, in this way, particle tracking approach further increases the sensitivity of the assay since rare binding events are recorded over the course of the experiment. Second, in binding assays to determine k_{on} and k_{off}, binding-debinding rates, separately, the reaction should be at the equilibrium at the moment of measurement. To confirm this, the time required to reach equilibrium might be concise with low-affinity samples since too few particles are needed to reach equilibrium on the sensor with dilute target species [49]. However, digital detection and tracking each binding event individually during the binding assay removes the need for the system to reach equilibrium before accurate debinding rates can be measured. Third, endpoint measurements require a defined incubation time and a wash step at the end. To finalize the assay, the sensor is washed with an inert buffer to remove unbound analyte and other residues from the analyte solution, which may end up with also a dry chip. The wash step and drying may cause variability in assay results, such as false positives due to residence of labeling nanorods or false negatives due to residence salt from buffer covering the bound analytes. Last, if we do not use dynamic tracking in real-time measurements and just count the particles in each frame to obtain an instantaneous number of particles, then this would cause false positive or negative results. Not every interaction on the surface is binding. With tracking, we can recognize if a particle gets close to the surface and skips binding, whereas if it actually binds on the surface by tracking through the frames. Moreover, since there is a flow, some unbound particles are

visible in each frame as they pass and diffuse through the detection volume. If when these transient particles are close enough to the surface and counted, they would cause an increase in the instantaneous number of particle count in the frame as false positives. As a result, in order to address all these issues, a dynamic tracking algorithm was developed in our lab by Derin Sevenler and Jacob Trueb, which is explained in detail in the previous studies [50].

The postprocessing detection and tracking algorithm determines the spatial positions of particles and track them individually during the experiment [50]. Figure 2.7 depicts the tracking approach. First, different spatial positions of the captured particles are determined to spatially discriminate newly captured targets from previously captured ones on the surface in each video frame. A list of particles with (x,y) coordinates are recorded for each frame independent of other frames (Figure 2.7B). Second, this position list is compared with the next list for the next frame (Figure 2.7C). If a particle is in the same position in the next frame, it is called "match," meaning that they are the same particle. A clustering algorithm is used to have the tolerance to small translations between frames. Third, these lists are used to combine all the tracking information through the video (Figure 2.7D). This big list shows when a particle binds at which position if it debinds from the during the experiment. Last, an algorithm is used to eliminate false negatives and false positives. Then, this big list is used to plot the cumulative number of new binding events over the course of the experiment (Figure 2.7A). Dynamic tracking is used in our nucleic acid and BNP detection experiments, which is detailed in Chapters 5 and 6.

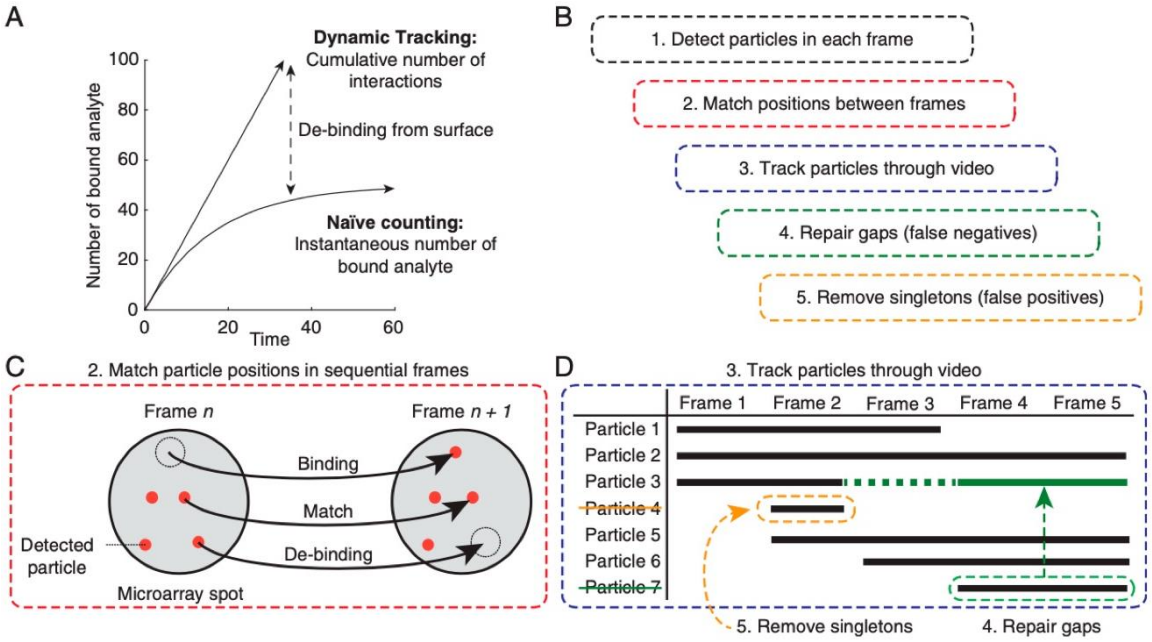

Figure 2.7 Particle detection, counting and tracking algorithm principle used in dynamic tracking. A) The plot for the number of bound nanorods over time. Naïvely counting the instantaneous number of bound analytes provides no additional information once equilibrium has been reached. Dynamic tracking differentiates binding of new particles versus debinding of old ones. Therefore, even at equilibrium, number of binding events increases. B) Work flow of the algorithm. C) Detection principle used in the algorithm showing that each particle in each frame is evaluated independently and this information is compiled to obtained the number and locations of binding, debinding and stationary particles. D) Finally, the algorithm tracks the contiguous series of frames in which each particle was observed and finishes with eliminating false negatives and false positives. Adapted from [50], Copyright (2019).

3 CHAPTER THREE THE DIGITAL MICROARRAY DESIGN

Microarrays are fundamental tools in biomedical research. Various solid-phase optical detection platforms have been recently reported for detecting broad varieties of analytes such as protein, nucleic acid biomarkers and biological nanoparticles. However, the detection of low abundance analytes such as rare nucleic acids or exosomes in complex media is still challenging. To achieve this, the bioassays are required to have high signal-to-noise ratio, dynamic range, sensitivity and low limit of detection. Proper design of the sensing area is crucial in surface-based biosensors for desired sensitivity. This chapter evaluates the advances in the compositional design and methods of surface modification in solid-phase optical biosensors to achieve the highest sensitivity and how we design our interferometric sensors for these types of applications.

3.1 Surface morphology and immobilization of the surface probes in optical biosensing

In the most general sense, label-free optical biosensors all utilize changes in scattering caused by either local or distributed changes in refractive index. Because the binding of nanoparticles to the sensor surface is detected as small local changes, the temporal and spatial variability of a system's baseline or reference signal limits the smallness of particles it can reliably detect. More generally, this source of noise limits the signal-to-noise ratio for any particle of interest. Hence, reducing this source of noise improves the sensitivity in nearly all cases.

Currently, optical sensors can employ a variety of support materials such as silicon,

glass, metals and polymers for different detection modes and architectures [51–53]. Single-molecule counting or digital detection enables high sensitivity. The selectivity of these assays relies on how properly the sensor surface is modified to recognize and capture the target among other molecules in medium. The sensitivity relies on the strength of the light-matter interaction at the sensing field [54]. It is desirable to simultaneously increase the signal and decrease the noise to achieve the best signal-to-noise ratio (SNR). The limit of detection (LOD) hinges on not only the affinity of the target for its receptors on the sensor surface, but also the capture efficiency during the measurements. Therefore, the design of the surface is crucial for sensor performance. When complex solutions (such as serum or whole blood) are used, the capture efficiency of the specific molecular or BNP targets can may lower. Cells and cellular components are optically inhomogeneous, stemming from heterogeneity across multiple length scales. As an example, cytoplasm has a refractive index of 1.38, whereas that of a cell membrane is around 1.48 [55,56]. Other structures in the cells, such as protein, have variable refractive indices ranging from that of the cell medium and up to as high as 1.53 [57]. The differentiation of target BNPs from such a complex background is a significant challenge in label-free detection of BNPs.

Proper surface functionalization enables high capture efficiency and selectivity by eliminating non-specific binding and reducing noise level. Even though, in principle, labeled and label-free detection techniques are very different, their performances are often affected by similar limitations. Figure 3.1 shows the most common surface functionalization and bioactivation steps of a generic sensor platform in biosensor manufacturing. The introduction of reactive functional groups enables the subsequent

surface immobilization of capture probes (Figure 3.1A). This step can be achieved via chemical derivatization or functionalization with a diverse range of chemical groups, self-assembled units, or polymers. Capture probes can be selected among various affinity reagents such as antibodies, nucleic acid, aptamers, etc. depending on the target of interest. In the development of the required surface chemistry, the only remaining concern is the affinity of the target structure towards the modified sensor surface, independent of the detection modality. The target structure influences the interaction with the biorecognition molecules on the sensor surface; nevertheless, these interactions in microarrays, such as antibody-antigen (Figure 3.1B), DNA hybridization (Figure 3.1C), virus surface antigen-immobilized antibody (Figure 3.1D), may or may not persist throughout the analysis period. Similar concerns are valid in three of the cases, apart from the target and detection techniques. Therefore, proper surface chemistry plays the most critical role in the realization of robust detection. A powerful detection can only be achieved when several conditions are satisfied; i) ultra-sensitivity (fg/mL – pg/mL range) since biomarker levels in biological samples are extremely low, ii) reduced noise level, high SNR (i.e. adequate correlation between target concentration and amount of signal), iii) excellent specificity.

In this section, we review the parameters playing a pivotal role in the sensor performance in optical detection technologies with a focus on imaging systems. We evaluate several factors affecting the biosensor performance, such as sensor surface area (Section 3.1.1), probe density (Section 3.1.2), orientation (Section 3.1.3), elevation and flexibility of surface-immobilized probes (Section 3.1.4) and morphology of the sensor surface (Section 3.1.5).

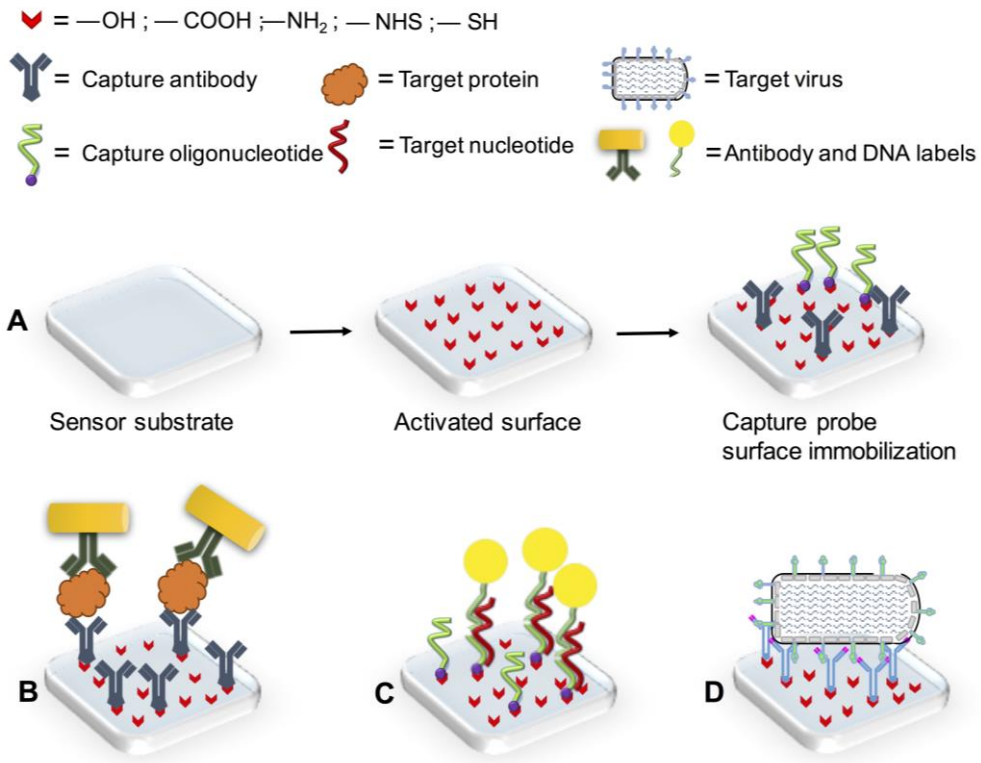

Figure 3.1 Conceptual illustration of a digital biosensor surface bioactivation with A) chemically active reagents and immobilized capture probes such as antibody and nucleic acid. Individual B) protein, and C) nucleic acid molecules are captured and labeled via nanoparticle-tagged antibodies and complementary nucleic acids, respectively. D) Natural nanoparticles such as viruses are captured on the sensor surface with the help of antibodies and detected label-free.

3.1.1 Surface area

The region where the surface capture probe molecules are immobilized defines the surface area on a solid-phase biosensor. The active sensor area typically limits the amount of target captured by the biosensor. Surface modifications redefines the surface area. By manipulating the surface area, dynamic range, sensitivity, response time, sample volume, and cost-effectiveness of the sensor platform can be controlled. If the field of interaction expands, the chances for the target molecules to have sufficient interaction with their affinity towards the surface-immobilized probes increases.

The duration for the target-surface interaction is limited in biosensors with flat-surfaces. The capture efficiency varies with the mass transfer limiting conditions and the assay feature size [58]. The speed of target transport to the capture surface limits the rate of target binding to the probes on the surface [59]. If the surface is prominent and accessible enough, target molecules can interact with the surface probes extensively in a given time. Increasing target-surface interaction frequency anticipates an improvement in target capture efficiency. Thus, sophisticated microfluidics are extensively used in biosensing. Merging sensing platforms to microfluidics provides an enhancement in sensing in many ways. First, the configuration increases the surface area if the interior surface of microfluidics is decorated with the surface probes. Second, multiplexed assays can be generated using multiple microfluidics or channels in parallel. Third, it provides a significant reduction in time for target-surface probe interaction by improving diffusion-limited hybridization kinetics [60,61].

Optical waveguide-based biosensors are strong candidates to be a capable biosensor to detect low copy numbered substances. In an integrated waveguide biosensor design, capillaries provide both fluid flow (sample solution) and light propagation via waveguiding and evanescent illumination [62,63]. The interior surface of the capillaries can be modified with the probe molecules such as DNA, proteins [64,65]. According to Ligler et al., when the biosensor response from the integrated waveguide is compared to a planar waveguide-based array biosensor, a significant reduction in LOD in protein sensing was achieved [62,66].

Optical sensors are confined to optically active sensor surface, therefore, only small

fraction of biomolecules in solution will interact with this field. Micro-ring resonators are one of the promising tools used in biosensing due to long-duration light-matter interaction on the surface due to demonstrated high sensitivity enabled by high-Q resonances in such structures [67]. They can be used in parallel for multiplexing; therefore, the sensitivity achieved in this type of optical sensors is comparable with that of refractometric techniques. Moreover, their micro-structured design enables them to be integrated into portable lab-on-chip platforms. With these properties, they have been utilized in many analyses, especially in medical and food safety applications [68,69]. The major challenge in achieving high sensitivity in ring resonator biosensors is related to the design and the definition of the surface area in fabrication. For planar materials, the majority of the optical field distribution is not accessible to the biological molecules where the only interaction between the biomolecule and optical mode occurs at the waveguide surface [70]. This limiting factor is usually overcome by novel designs to extend the surface area and amplify the interaction [71]. Rodriguez et al. have proven this approach with an alternative strategy by using porous silicon for the ring resonator, taking advantage of its large internal surface area, the availability for biofunctionalization, and tunable optical properties [67]. It was shown that porous silicon films have a surface area of more than 180 m^2/cm^3 providing a large area for target binding compared to the planar transducer materials [72].

Surface plasmon resonance imaging (SPRi) is a well-established technique among the surface-sensitive optical techniques and a reliable alternative to the conventional fluorescence-based microarray DNA detection techniques. Despite being very widespread, it suffers from limited sensitivity and being oversensitive to environmental changes [73].

For instance, in an average large-surface SPR biosensor, the conventional chip area provides a LOD in the range of ng/mL per biomarker. However, many biomarkers exist in bodily fluids at as low concentrations as fg/mL, which makes detection challenging [74]. The integration of the conventional SPR sensors with nanostructured surfaces enhances the sensitivity of the detectors. Nanostructured substrates are employed in many biosensor designs to obtain high capture efficiency and sensitivity by increasing surface area to have more interactions in unit time.

Moreover, the probe number increases with the increase in surface area; therefore, the chances of interacting with the low numbered target molecules increases. Malic et al. have shown that the integration of periodic two-dimensional gold nanostructures to the flat sensor surface improved SPR signal significantly by increasing target binding area and the coupling of localized and bulk surface plasmons provided by the nanospots [73]. A significant sensitivity improvement with a five-fold enhancement in the SPR signal has been achieved compared to the conventional SPRi biosensors. Reflective interferometers take advantage of the large surface area where the entire chip surface is utilized for sensing and large field of views are employed [75,76]. Nano-enhanced surfaces are also widely used in reflective interferometers, allowing for more interaction sites for the probes immobilized with the target molecules. An excellent example of nano-enhanced surfaces is the nanostructured Fabry-Perot interferometer (FPI) with embedded nanostructures in its cavity [77]. Gold-coated nanopores provide sensitive optical sensing compared to the conventional micro-structured FPIs. By nano-manufacturing the sensing area, the optical transducing signal is amplified four-fold without any instrumental optimization.

Enlarging the sensing area with integrated elements has an undeniable impact on target capture efficiency. Further, the microarray spots created in the sensing area also determine the biosensor performance. The spots are the regions on an array where the probe molecules are printed in defined positions with precise intervals. Usually, a microarray consists of multiple, even thousands, spots targeting either one type or multiple types of analytes. Assay miniaturization enhances the fractional feature capture capacity and target coverage uniformity, both of which are increased by decreasing the spot size [59]. This has been demonstrated in a study done by Dandy et al. in which various DNA probe spot sizes and corresponding probe densities were tested [59]. It has been shown that target hybridization efficiency in radiometric assays increased with the decrease in spot size. 60–80% of equilibrium hybridization efficiency was obtained in the smaller spots (10–100 μm in diameter), whereas the larger spots (100–1500 μm diameter) yielded 10–20% equilibrium efficiency [59]. Intriguingly, when the hybridization efficiency was estimated across a 2mm-wide, uniform spot, the efficiency increased only around the edges of the large spot. This has been elegantly explained as a variation of target transport across a large spot. The target is delivered to the edge of the spot with a higher rate [59,78]. The experimental and theoretical data suggest that this is a result of mass-transport-limited conditions in the larger spots. Conversely, smaller spots approximate to kinetically limiting behavior. As a result, in order to keep the binding uniform across the spot, indifferent to operation kinetics, and to have a uniform analyte flux on the spot for highest capture efficiency, the optimal spot size should be kept under 200 μm.

Zhao et al. also reported the limitations caused by the effect of mass-transport in

microarrays. They used a high-resolution molecular interferometric imaging (MI2) and observed an inhomogeneous distribution of analyte binding across a 100 µm-protein spot [79]. The analyte binds and depletes locally around the spot, and the analyte transport falls behind the binding because of the faster rate of analyte binding. This deceleration in the reaction causes a reduction in the amount of captured analyte [80]. This is considered as the primary limitation in microarray assays. The results clearly evidenced that to limit the mass transport effects, the necessary conditions for the spot size and the flow rate can be determined for uniform target binding across a spot for a given association rate for the target.

3.1.2 Probe density

The probe density across the sensing area is a controlling factor for the performance of the sensor, which directly affects the bulk of measurable signal. The frequency of the probes should be high enough to adequately capture the target molecules and sufficiently low to prevent steric hindrance and to meet the mass-transport limitations [58,81–83]. When the probes are immobilized on the surface at high concentrations, the distance between the probe molecules is short, which may diminish the accessibility of the probes. Thus, target molecules might not be adequately captured. For the same reason, the binding sides on the probes become less accessible for target binding. Hence, although free targets are present in the sample solution, due to the deficiency in interpenetration of the target through the probes, the target capture may not take place. On the other hand, if the surface concertation is too low, the chances of capturing target molecules also decrease. The probe density directly affects the competency in the binding of the target.

It has been reported that high probe density does not always carry in high efficiency in hybridization with target [78]. Peterson and coworkers investigated how DNA probe immobilization and density impact target capture using an SPR-based biosensor [78]. Single-stranded DNA oligos were used as the surface probes to capture similar size DNA targets. It has been shown that both the hybridization efficiency and the kinetics in binding rely strongly on the probe density. An improvement in hybridization efficiency from 15% to 95% was achieved by controlling the probe density in the sensing area. Surprisingly, the highest density yields the lowest efficiencies. This phenomenon has also been shown by Ramdas et al., where a fluorescence-based DNA microarray was prepared to detect rare cDNAs [84]. Although a linear dependence between target concentration and the signal intensity following pseudo-first-order kinetics was expected, instead, they obtained results fitting to a second-order kinetics model. This was explained with the effect of probe concentration spotted on the microarrays. After testing different probe concentrations, they showed that the impact of the increase in probe concentration on signal intensity is minimal.

The work done by De Avila et al. explicitly demonstrates that the performance of a sensor depends on the effective probe concentration, the surface area and the sample volume rather than the true affinities of the probes [85]. The effective probe concentration is defined as the probe concentration as if the surface-immobilized probe molecules are released in the sample volume. In this study, the authors compare concentration-limited versus ligand-depletion regimes for a DNA sensor. The concentration-limited regime occurs when the effective probe concentration is lower than the K_D value (inverse true affinity) of the probe for its target. When in fact, the ligand-depletion regime occurs when

the true affinity of the probe for its target is high with a low K_D and K_D is lower than the total number of target molecules (ligand) [85]. As a demonstration, when a 27-base DNA probe is used with its 27-base perfectly-matching complementary target, the true affinity of the probe is very high for its target (K_D is low). When the probe concentration changes, binding affinities, therefore, binding curves change. The source of the noticeable difference in the binding curves was shown as probe density on the surface. Since the true affinity of the probe for its target is comparably smaller than the effective concentration of the probe, the binding curves represent saturation when all the target molecules bind to all the probes on the surface. Hence, when the effective probe concentration increases, the apparent affinities increase. Therefore, the observed affinity is controlled by the probe density and the volume of the sample, which determines the LOD and specificity. In ligand-depletion regime, the observed affinity is more affected by the experimental setup than by the true affinity where specificity diminishes. Therefore, the experimental conditions should be considered to obtain a concentration-limited regime with good specificity and low LOD [85].

Antibody packing density is a significant parameter determining the activity of the antibody molecules. Since low densities may lead to structural unfolding, while high packing may cause steric hindrance, a sweet spot for high immobilization efficacy should be achieved [86]. Based on the ambient analyte theory, in microarrays with microspots, the concentration of antibody probes should be less than the concentration of target protein in the analyte solution [58,87]. Consequently, using systems with high SNR, the LODs in femtomolar range can be readily achieved in theory [79,88]. Nevertheless, the number of

studies reporting this sensitivity is limited due to the mass transport limitations in many current microarray technologies [80]. Therefore, depending on the fabrication constraints and the application requirements, the mass transport limitations should be reduced in optimization steps for any biosensor to obtain a kinetic-controlled reaction.

3.1.3 Orientation, elevation and flexibility of surface immobilized probes

Molecular interactions rely on the differences in thermodynamic equilibria. In the interactions occurring at an interface, surface energy minimization mechanisms step in and the influence of the interface, the conformation of the molecules at the interface, the geometrical structures and the chemical compositions of the biofilms play crucial roles in molecular binding. Hence, in all microarray-based technologies, the surface-immobilized probes must reach thermodynamic equilibrium conditions to have accessible and steric hindrance-free probe orientations [78].

It is given that to enhance specific binding and eliminate non-specific binding, the retainment of the functionality and the accessibility of the probes must be guaranteed after immobilization [89]. This is the major constraint for probe immobilization in biosensor preparation. In many protein assays, function and activity retainment is achieved by region-selective protein immobilization [90]. By changing the molecular orientation in immobilization, different structures on the surface can be obtained. Oriented immobilization refers to controlled immobilization of the antibodies to the surface so that Fab regions are well-exposed and revealed on the surface, remaining available for efficient antigen interaction. With controlled orientation, high target interaction is achieved, leading to enhanced sensitivity. Moreover, whole antibodies or a fraction can be immobilized

selectively for specific target capture. In this manner, unforeseen non-specific interactions can be eliminated to some extent.

The orientation of the immobilized proteins can be controlled with the power of surface chemistry. Chemically functional groups such as hydroxyl, carboxyl, thiol, amine and many others can be introduced to the sensor surface for robust covalent binding of the antibodies [91,92]. However, the surface should be activated in a controlled manner. Too low surface-active groups may cause low immobilization efficiency and loss of activity of the probe molecules or probe loss during the measurements [93]. Besides, if the surface is activated with too many functional groups, then it may cause excess binding of the antibodies to the surface with improper anchoring via covalent linkages causing loss of activity and non-specific interactions. Additionally, high-density surface probes give rise to steric hindrance and the repulsion between antibody molecules may cause deactivation. Three-dimensional matrices used for surface modification such as sol-gel structures provide improved oriented antibody immobilization. In a study by Orlov et al., magnetic nanoparticles-integrated nitrocellulose membranes provide a surface area with selective immobilization of antibodies. The sensor's limit of detection for prostate-specific antigen in serum was improved to 740 fM, which is comparable with the ELISA test with significantly enhanced dynamic range [94].

Previous studies have represented that the behaviors of single-stranded DNAs (ssDNAs) and double-stranded DNAs (dsDNAs) differ from each other in terms of orientation on a surface when they are end-tethered to the surface. Although the orientation of dsDNAs can be controlled with external forces such as electric field, it is hard to orient

ssDNAs [95,96]. It has been exhibited that for the single probe-single target systems, when the DNA probe length increases, the chances of a target finding a probe fragment increases; whereas, the chances of the target binding to the whole probe decreases [97–99]. Therefore, the sensitivity increases; however, the specificity decreases. Moreover, the kinetic studies for surface tethered-DNA hybridization have revealed that hybridization most likely starts from the ends of the ssDNAs. Thus, the sequences located in the center of the DNA probes stay bound to the target for a longer time compared to the ends of the probe throughout the experiments [99]. This suggests that proper orientation, accessibility and flexibility of the probes are the most crucial parameters in developing a biosensor.

DNA hybridization mainly depends on two factors: the probability of two complementary sequences finding each other and the rate of binding when they interact [100]. On a biosensor surface, high probe density, improper probe orientation or flexibility issues may impede interaction and the initiation of hybridization (nucleation). Among these issues, restricted interaction with the nucleation site may be the leading problem [101,102]. To test this argument, a 25-nucleotide probe was immobilized on an SPR sensor surface and two 18-nucleotide targets were used in measurements [102]. One of the selected targets is complementary to the upper part of the probe (18 high), while the second target is complementary to the lower part of the same probe (18 low), in which the nucleation site for the hybrid is close to the sensor surface. When both of the targets and the probe are free in solution, the binding kinetics are the same; however, when the probe is immobilized to the surface, a slower binding was observed between the probe and 18 low target compared to 18 high target [102,103]. The limited access to the hybridization site impedes faster

hybridization and the target molecules have to penetrate through the probe layer to reach the complementary portion of the probe [101]. As a result, the elevation of probe molecules is vital in biosensor applications to reveal the binding sites.

A schematic comparison of oligonucleotides with oligoethylene glycol linkers in different lengths is shown in Figure 3.2 [104]. The figure mimics the oligos immobilized in a density of 10 pmole per mm^2, equal to one molecule per 39 square angstroms. The oligos stay in a position where they can barely touch each other. While they seem stretched away from the solid-support in the figure, they are in a more compact structure while tethered to solid-substrate in reality. The probes are immobilized along with a spacer oligo, which prevents overcrowding, thereby, steric hindrance. Moreover, some of the oligos are modified with linkers ranging in 26, 60, 105 atoms length. Oligos with longer oligoethylene glycol linkers can reach further in the solution with the help of elevation which provides an advantage for capturing the target over their neighbors. The spacer length is also significant for an efficient hybridization. Beyond a certain length, the efficiency diminishes due to the over-interaction of the probes with each other, the spacer and the solid-substrate; hence, they become less accessible [105,106].

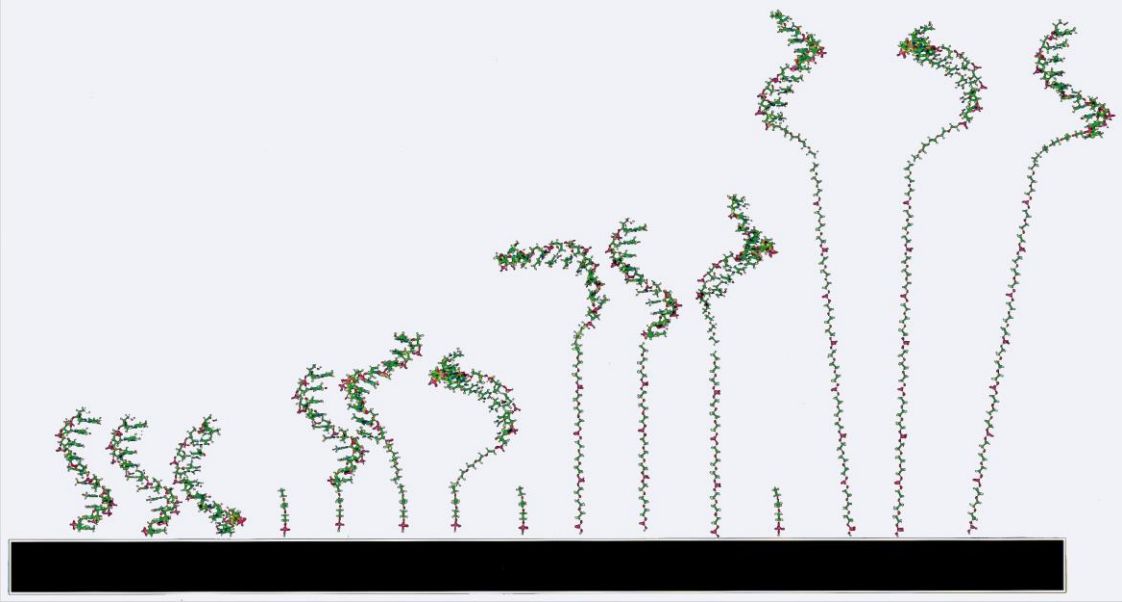

Figure 3.2 A schematic comparison of various length of oligoethylene glycol linker for DNA oligonucleotide probe elevation. Oligonucleotides are immobilized on the glass surface in a mixture with a spacer oligonucleotide. The linker lengths are 26, 60 and 105 atoms. Reprinted by permission from Springer Nature, Nat Genet, Southern, E., Mir, K., Shchepinov, M. Molecular interactions on microarrays. 21, 5–9 (1999). Copyright 1999 [104].

3.1.4 Morphology

Conventionally, optical sensing relies on small variations in scattering due to the local changes in the refractive index. Since the binding of a target creates a small local change on the surface, the sensing platform's baseline signal is the limitation in recognition of the labeled- or label-free targets. The temporal and spatial variability of the baseline signal determines the reliability in the detection of the smallest particle by the system. Therefore, this variability builds a noise which may wash out the optical change generated by the target by confining the SNR for the particle of interest. As a result, if this noise is reduced, the sensitivity in the measurement can be improved regardless of the sensor or the optical detection technique.

A proper detection requires a distinct signal coming from the target over the background. This can only be achieved by creating a smooth, uniform morphology at the sensing area. The sensor surface must maintain its integrity throughout the measurements and yet stay inert and selective to non-specific molecules in a heterogeneous sample. Therefore, the signal derived by the target can be distinguished from the background noise and surface roughness [107]. Scattering due to the non-uniform and fouling background may surpass that of the target, causing a reduction in sensitivity and resolution. Contrarily, the loss of sensor response cannot be explained correctly and the performance of the sensor may be misinterpreted.

The biosensor responses proportional to the target concentration can only be obtained with the sensor platforms free of background, solely relying on target-probe affinity. The interference reflectance imaging technique is a key approach in sensing small inhomogeneities on the layered supports [108,109]. It is widely applied in microarray-based biosensing for monitoring biological interactions [21,110,111]. As mentioned in Chapter 2, the binding of the target to the surface confers slight local changes in the reflectivity spectrum of the layered support behaving as an additional layer [24]. This can be exploited for quality checking, and to characterize and confirm the surface morphology, uniformity and evaluation of the probe density after immobilization [32,112]. Figure 3.4A and B show the images of 200x200µm regions on IRIS chips with highly non-uniform protein spots after an uncontrolled immobilization [107]. Micro-droplet arrayers are employed to prepare microarrays with uniform, periodic spots of biomolecules on various types of supports. However, certain parameters such as humidity, temperature, content and

concentration of the probes must be well-adjusted for a proper immobilization and spot quality. In the cases where the surface functionalization is not predictable, the surface coating may turn out to be rough and uneven, causing abrupt noise in the experiments. It might be hard to detect diffraction-limited features due to the high background. Large-sized, non-uniform, irregular spots may be formed. In comparison with Figure 3.4C, other spots hold small, diffraction-limited features, heterogeneities and random shapes. Small features originating from irregular spotting may interfere with the BNPs during the digital detection of viruses or exosomes. Small local changes to the optical signal may be absorbed by the background which diminishes the sensitivity. Besides the optical imaging challenges, improper spotting and the lack of quality control may cause a loss of activity in probes, non-specific interactions on the surface, and reproducibility issues sensor fabrication.

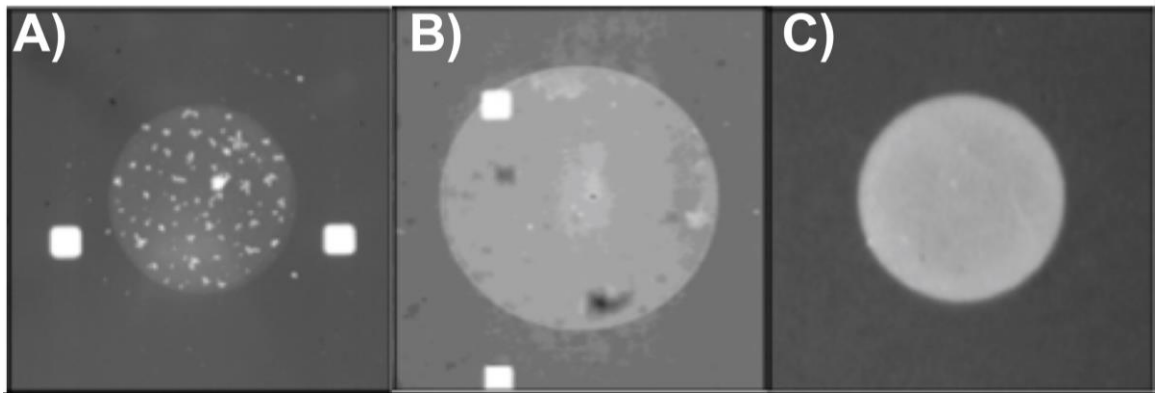

Figure 3.3 IRIS images of irregular (A and B) and a regular (C) protein spots generated by a micro-droplet arrayer. Uneven and inhomogeneous, irregular-shaped spotting may happen due to spotting solution and conditions even after several spotting optimizations. A) Remaining of salt on the spot, B) uneven immobilization of the protein and non-uniform drying of proteins throughout the spot may be obtained. Better selectivity and sensitivity may be obtained starting with a spot as in image (C) which is spotted uniform and homogeneous. [107].

3.2 SP-IRIS chips and cartridges

In the previous section, we have identified the requirements for an ideal sensor morphology. As well as the surface the sensor has, the measurement quality and success also depend on the imaging medium and how well the instrument can function in the selected medium. SP-IRIS platform can employ both dry (in-air) and in-liquid imaging. The former means that the detection is based on in-air imaging of dry chips that are pre-incubated with liquid samples in petri dishes and imaged afterward (end-point). The latter includes a microfluidic cartridge and liquid handling systems for sample flow. Dry or end-point measurements allow for a simple and straightforward application that does not include liquid handling or previously explained detection challenges stemming from the nature of the in-liquid measurements. Nevertheless, manually incubating the chip with the sample solution and letting it dry lead to morphology problems such as residue remaining from the wash buffer, nonspecific surface binding of nanoparticles during wash, variability in the surface, or wash quality due to user dependency or unevenness in the drying of the surface. Therefore, in-liquid measurements are preferred in applicable cases.

3.2.1 Microfluidic cartridge and through-via chip design

The early generation of SP-IRIS cartridges were for the detection of label-free viruses; therefore, they were meant to be disposable, assembled and cheap. The first-generation cartridge was multi-level laminate-based. The channel was formed in between the planar Si sensor chip and multi-level plastic adhesive films with a rigid acrylic base (Figure 3.4A). This version cartridge enables controlled flow rates. It utilizes a square Si/SiO_2 chip.

The second-generation cartridge consists of a paper-based fluid handling as well as a multi-level laminate design (Figure 3.4B). It utilizes a rectangular Si/SiO_2 chip. It employs a sample reservoir and an absorbent pad, which create a capillary-driven flow and removes the need for a syringe pump to flow the sample solution in the cartridge. As a result, this version cartridge stands alone and provides minimal sample exposure risk.

On top of being not very cost-effective, these two generation cartridges limit the quality of the images due to the plastic/polymer window material, alignment problems and difficulties in applying anti-reflection coatings. Based on these experiences, the next and last generation of SP-IRIS chip and cartridge were designed.

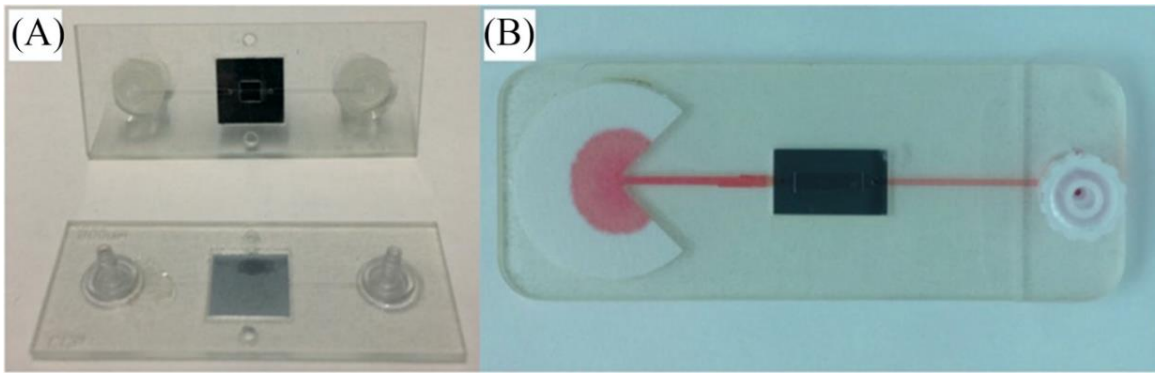

Figure 3.4 Early generations of SP-IRIS cartridges for label-free virus detection. A) First-generation disposable, laminate, active floe cartridge. B) Second-generation disposable, laminate, passive cartridge. Reproduced from Ref. [37] with permission from the Centre National de la Recherche Scientifique (CNRS) and The Royal Society of Chemistry.

To satisfy both high-quality and cost-efficiency demands, a new chip/cartridge configuration has been designed for in-liquid particle detection [113]. The new design still uses Si substrate with thin thermal oxide as the sensor chip. Uniform layers of oxide are grown on the Si substrates via a self-limiting thermal oxidation process. Si substrates are commonly used in optical imaging due to their applicability in biological applications,

comprehensive knowledge in manufacturing, compatibility with a wide range of materials for surface modification, as well as light absorption property to prevent stray light.

The new generation, innovative through-silicon-via (TSV) SP-IRIS chips and the cartridge design offers a low-cost and high-optical quality solution for microfluidic SP-IRIS experiments. TSV chips possess through holes cut directly into the chip on each side of the chips, which are drilled on using laser micromachining (at Potomac Photonics). This way, the chip can be easily integrated with the cartridge. The TSV chips are designed for high-throughput nanoparticle analysis in a microfluidic channel.

The TSV chips are in a rectangular design with dimensions of 25 mm × 12.5 mm. Figure 3.5A shows a wafer consisting of new generation TSV SP-IRIS chips which is a single 6-inch wafer (110 nm thick oxide on Si) yielding 42 individual chips. Wafers are manufactured by Silicon Valley Microelectronics, Inc. and diced to the appropriate size at Boston University. Each chip has a 6 mm × 8 mm middle region for the microarray spots, which allows for packing ~760 spots with 250 μm spot center-to-center distance in rows and columns. The sensor chip holds two holes on each side of the rectangle for inlet and outlet for fluidics. A microfluidic channel is formed by placing a cover glass (0.7 mm thick) on top of the sensor chip by using a 200 μm-thick pressure-sensitive adhesive (PSA) gasket (Grace Bio-Labs) adhesive layer in between the cover glass and the TSV chip (Figure 3.5B). Through holes in the chip substrate allow the sample solution to flow directly on top of the chip by being pumped into the incubation channel, eliminating the need for multiple laminate layers to create a fluid path over the chip edge as in the previous generations. As a result, TSV chips can utilize a simple incubation channel disposable consisting of a single

transparent polymer film coupled to a laser-cut PSA layer (the spacer or adhesive layer). This simplified design makes these disposable parts very cost-efficient compared to the multi-level laminate design.

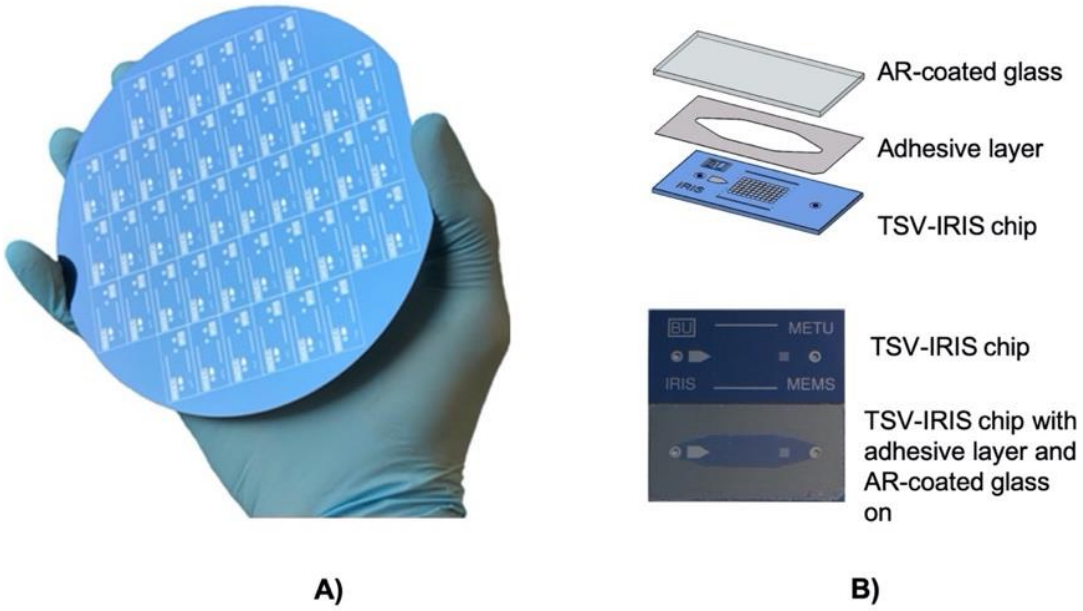

Figure 3.5 A) New generation SP-IRIS chips with through holes on a 6 in wafer. B) Illustration of assembly of TSV SP-IRIS chip (top) and photograph (bottom) of single TSV-IRIS chip with anti-reflection coated glass and adhesive layers to form microfluidic channel.

The cover glass is anti-reflection (AR) coated on one side to reduce the effect of reflections from the air/glass interface, which can significantly affect the image quality in polycarbonate or cyclic olefin copolymer (COC) based windows. In our studies, we have used two types of spacer: one with double-sided sticky and one with single-sided sticky. The former spacer has adhesive on one side for attachment to the cover glass. The single-side adhesive channel layer permits easy removal of the disposable sensor chip from the spacer/glass assembly. This enables re-use of the spacer/glass assembly with a different sensor chip, or additional handling of the used chip if necessary. The channel height and

material can be easily tailored to need. We have identified double-side pressure-sensitive adhesives (PSA) with a carrier layer in between as a suitable alternative for thinner channels down to 130 μm, in which case, the whole cartridge is single-use.

Depending on the components of the chip/cartridge i.e., single/double-sided spacer, cover glass thickness, AR coating properties, the cost of the cartridge is about under $10 for 100s to 1000s chip which can be further reduced to $2 for larger production volumes.

3.2.2 Fixture design

The assembled cartridge consisting of the glass/channel/chip unit is placed in a custom-made fixture [113]. The fixture is a cam-actuated clamping fixture, as shown in Figure 3.6. It is compatible for the use with a 20x, 0.45 NA objective with a working distance of 4.5 mm. It connects the cartridge to the fluidic system. The fixture contains three main parts connected to an aluminum base plate. The fluidic manifold (Figure 3.6A(a)) includes an O-ring interface between the microfluidic chip and the external pump. The chip is placed on top of the O-rings on each side of the chip (red pieces in Figure 3.6B) where the inlet and outlet holes are present. The second part is a removable clamping plate with a viewing window (Figure 3.6A(b)), which gets attached to a spring-loaded mechanism and applies a downward force to the top of the cartridge to have a seal against the O-rings underneath. Providing enough of the pressure is essential to have a seal to avoid any leakage at the interface with fluidic pump. The fixture has two states – a loading state (Figure 3.6A and C) and a clamping state (Figure 3.6D). In the former, after removing the clamping plate, the chip can be easily placed on top of the O-rings. In the latter, a force is applied evenly to the top of the disposable cartridge by rotating the cam handle clock-wise.

The cartridge gets squished and sealed between the clamp plate and top surface of the manifold. The third part is a rotary cam (Figure 3.6A(c)), which controls the position of the removable clamping plate. The user can switch between the clamping state and the loading state by rotating the cam handle by 180 degrees, which activates a cam follower connected to the spring carriage.

Figure 3.6B shows a cross-section of the fixture. Two vertical channels are placed in line with the fluidic ports on the cartridge. 1/16” ID FEP tubing is used to connect the microfluidic channel to an external pump where the fluid travels. The tubings are inserted into the manifold from inlet and outlet ports until the tube ends are nearly co-planar with the top surface of the manifold. Tubings possess flangeless chromatography fittings from Upchurch Scientific (Oak Harbor, WA) to lock them in place at the interface. O-rings (0.070” Thickness, 1/16” ID x 3/16” OD) are used at the interface between the back of the chip and the tip of the tubes which seal perfectly and fill in the gap between the tubes and the manifold. As a result, fluid does not get in touch with the fixture parts; it only goes into the microfluidic cartridge owing to the perfect seal. To flow the fluid into the channel, a syringe pump (PHD 2000) from Harvard Apparatus (Holliston, MA, USA) and silicon tubing (FEP Nat 1/16” × 0.010” × 20 ft) from Upchurch Scientific, IDEX Health and Science (Middleborough, MA, USA) are used.

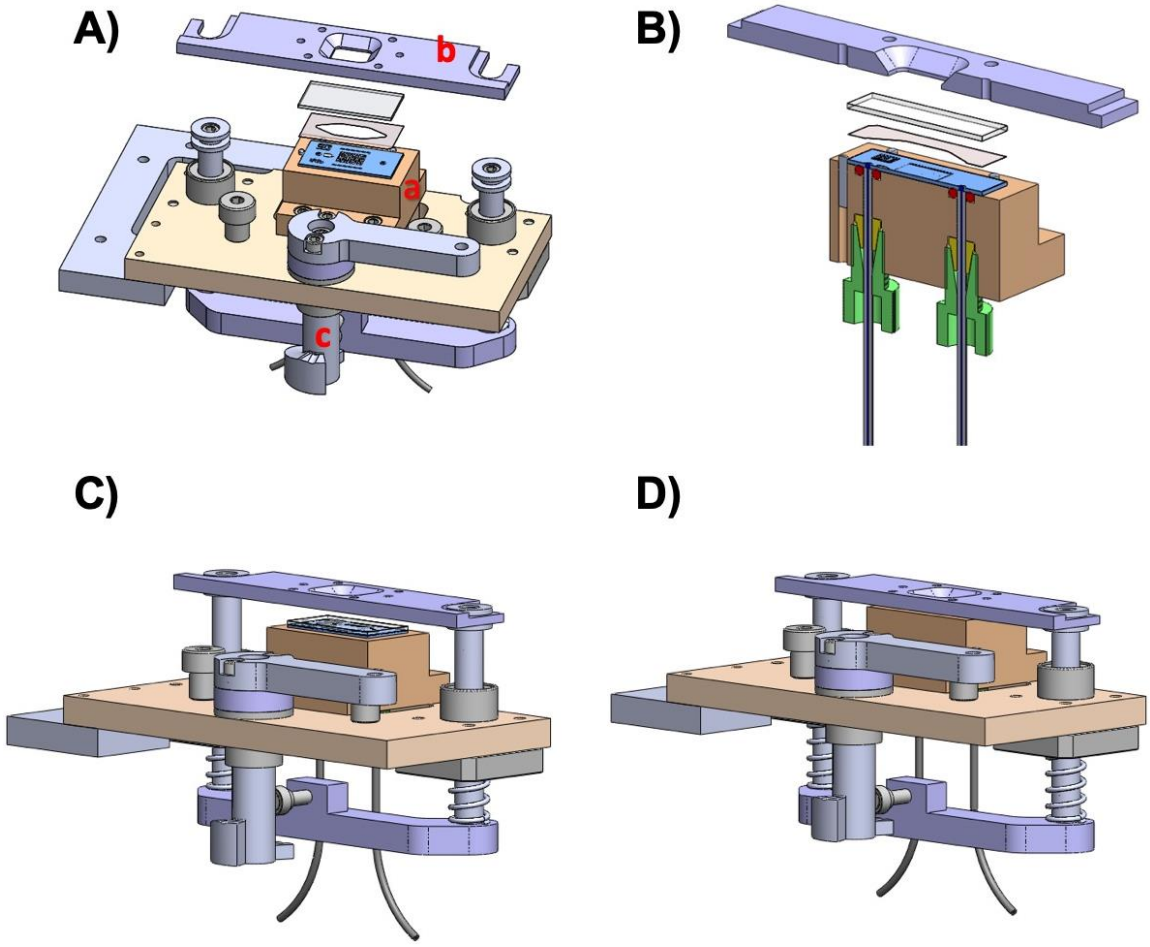

Figure 3.6 A) SolidWorks models of cam-actuated clamping fixture and the chip assemble in loading mode. B) Cross-sectional view of the fixture. The cross-section shows the fluidic path and connections, where the cartridge is placed on the fluidic manifold. C) The fixture with the chip placed before rotating the Cam handle and applying the clamping force. D) The fixture after rotating and clamping the plate on the chip and locking springs into a compressed configuration.

3.3 Sensor preparation

As mentioned before, SP-IRIS substrates, 6-inch silicon wafers with a patterned thermally grown silicon dioxide of 110 nm, were purchased from Silicon Valley Microelectronics (Santa Clara, CA, USA) and diced into 25 mm × 12.5 mm × 0.5 mm rectangles. The chips were cleaned by sonicating in acetone, rinsed with isopropanol and

deionized (DI) water and dried under nitrogen. In this section, we describe the preparation of the chip surface for biomolecule immobilization and the generation of protein and nucleic acid microarrays.

3.3.1 Surface chemistry

In order to capture the target molecules on the surface of the layered IRIS Si/SiO_2 substrate, first, it has to be functionalized for specific target binding. The surface chemistry used to modify the substrate should meet the requirements of availability of functional groups for probe attachment, no non-specific binding to the surface, stability against environmental changes, and also ideally be low cost, robust and easily prepared [114]. In order to do so, the IRIS chip surface is modified with a 3D polymer coating which is MCP (copoly-DMA-MAPS-NAS) from Lucidant Polymers (Sunnyvale, CA, USA). The polymer is commonly used to coat glass, silicon, or other hydroxylated surfaces for microarray applications described in detail elsewhere [115]. MCP-2 copolymer for antibody surface probe immobilization in protein microarrays, and MCP-4 copolymer for amine-terminated oligonucleotide (ssDNA) surface probe immobilization in nucleic acid microarrays were used. Each monomer forming the MCP-2 and MCP-4 (copoly-DMA-MAPS-NAS) copolymers has a different function: dimethylacrylamide (DMA) enables self-adsorption to the SiO_2 substrate, 3-(trimethoxysilyl) propyl methacrylate (MAPS) provides covalent binding to the substrate through silane functional groups, and acryloyloxysuccinimide (NAS) presents NHS ester groups which are utilized in biomolecule probe covalent immobilization. These active groups react with the primary amines in the protein structure or amine end of the modified oligonucleotides to form

covalent bonds. They differ only in the co-monomer ratio: 97:2:1 in MCP-2 and 89:10:1 in MCP-4. The fraction of amine-reactive sites of MCP-4 is five times larger than that of MCP-2 [116]. These polymers were shown to have increased probe density compared to 2D coatings involving silane chemistry and also very low non-specific binding [117]. Figure 3.7A shows the generic structure of MCP copolymers coated on a glass surface. When polymer gets in contact with a liquid, hydration occurs and it gets swollen in fluidic environment. Figure 3.7B shows a general representation of a 3D form of the polymer with antibodies attached to them. As shown in the schematic figure, immobilized antibody surface probes are distributed in the liquid environment owing to the elevated and flexible arms of the polymer. Yalcin et al. have shown that the polymer swells 7–20 nm in liquid solution, which elevates the immobilized probe molecules that are already attached to the polymer and makes them more available for surface reactions [33]. The polymer density close to the surface is higher due to the silane interactions. The chains far from the glass surface have a less dense organization which are more elevated and flexible, making the surface excellent for biomolecule capture, as discussed in the earlier sections of this chapter.

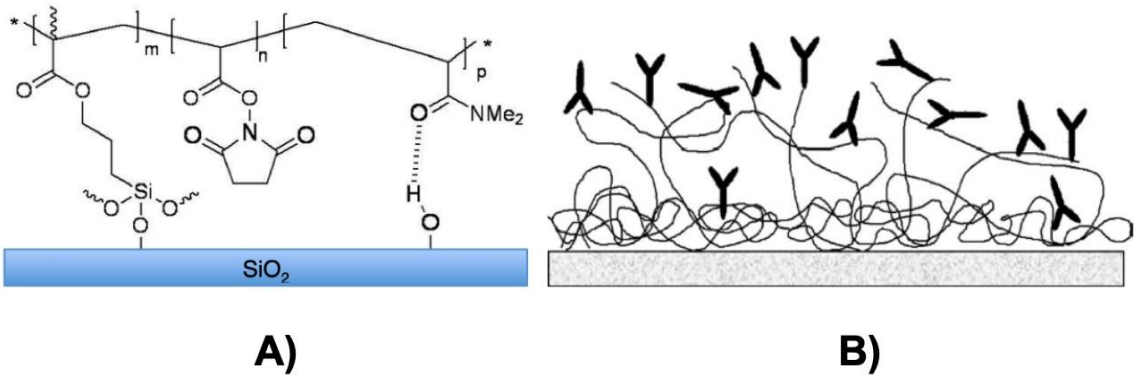

Figure 3.7 A) Chemical structure of the Lucidant copoly(DMA-NAS-MAPS) copolymer coated on a glass surface [33]. For MCP-2 and MCP-4 copolymers m:n:p monomer ratios are 97:2:1 and 89:10:1, respectively. B) Schematic representation of the copolymer used in immobilization of antibody surface probes in a fluidic environment. Reprinted from Anal. Biochem. 332, M. Cretich, G. Pirri, F. Damin, I. Solinas, M. Chiari, A new polymeric coating for protein microarrays, 67–74., Copyright 2004, with permission from Elsevier [115].

Furthermore, in order to obtain more hydrophobic surfaces, MCP-2F copolymer (from Lucidant Polymers). The lower surface energy of MCP-2F prevents spreading and merging of the spots. Figure 3.8 shows the chemical structure of MCP-2F copolymer coated on the surface.

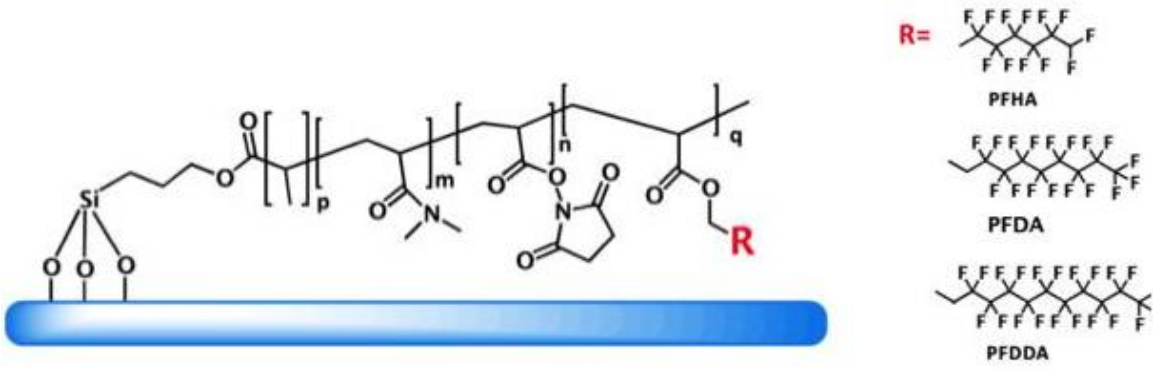

Figure 3.8 A) Chemical structure of the Lucidant MCP-2F copolymer coated on a glass surface [118].

3.3.2 Surface preparation

The Si/SiO_2 chips are oxygen plasma treated before polymer coating, which forms a hydroxylated surface for polymer to adhere to the substrate. The chips are treated by plasma ashing with oxygen plasma at 300 sccm and 500 W for 10 min. The polymer solutions are prepared according to the manufacturer's directions. Briefly, 50x polymer stock solution is diluted with the Coat-On solution from Lucidant Polymers. The chips are immersed in this polymer solution for 30 min. Then, they are rinsed with DI water at least six times remove extra unbound polymer and dried with nitrogen. Last, the polymer coated chips are baked at 80ºC in the vacuum oven for 15 min and stored at room temperature in a desiccator until spotting.

3.3.3 Microarray fabrication

A Scienion S3 SciFlexArrayer (Berlin, Germany) spotter was used to create an array of surface probes. The micro-printer is capable of repeatedly producing droplets between 150–300 pL with the dispenser used (PDC 60) and placing them in a grid with an accuracy of ~20 µm. The instrument provides high precision and accuracy in spotting thousands of spots on the chip surface with a user defined pitch (200–250 µm in our studies) between the spots. A typical droplet of 180–250 pL creates a spot of ~90–150 µm diameter. Any desired pattern of spots of surface probes can be created on the surface. The polymer coated chips are placed in the spotter chamber and antibody/nucleic acid solutions were placed in the reservoir. The surface probes are spotted periodically onto the surface of the chip by the spotter.

In protein and virus microarrays, antibodies specific to the target protein or virus are used as surface probes. In nucleic acid microarrays, amine-modified ssDNA oligonucleotides complementary to the target nucleic acid are used as surface capture probes. Surface probe solutions are always prepared freshly prior to each spotting session. The spotter uses about 3 μL of the sample solution and at least 8 μL of surface probe solution is prepared for every condition. For protein arrays, the humidity of the spotter humidity chamber is kept at 57%, while for nucleic acid microarrays, it is kept at 67%. After spotting on the chips, the sensor chips are kept in the humidity chamber at 67% humidity overnight to allow the surface probes to immobilize and covalently bind to the polymer on the surface. After polymer coating, the surface exhibits functional groups for the easy immobilization of molecules of interest. The binding between the biomolecule and the solid surface during immobilization is strong enough to retain the molecule on the surface during the entire biosensing experiment. Moreover, the local chemical environment allows the immobilized molecules to retain the native conformation and its functionality after immobilization. Following the overnight immobilization, the chips were blocked the next day using 150 mM ethanolamine in 0.1 M Tris buffer saline pH=9.0 to quench the remaining NHS groups in the polymer to deactivate it for the rest of the experiments. The chips are then washed with washing buffers to get rid of the unbound surface probe molecules.

For blocking, antibody-spotted chips are immersed in the ethanolamine containing buffer solution for 1h at room temperature. Then, they are rinsed with Nanopure DI water. To block nucleic acid-spotted chips, the ethanolamine buffer solution is warmed up to 50

ºC in a hybridization oven. Nucleic acid-spotted chips are immersed in the warm buffer for 15 min. Then, the chips were washed using warm 4xSSC buffer containing 0.1% SDS for 2 min while on the shaker at medium speed. The chips are then rinsed with DI water, dried with nitrogen. The chips were stored in a desiccator under vacuum at room temperature until they are used in two weeks.

4 CHAPTER FOUR A DIGITAL PROTEIN ASSAY FOR HEPATITIS B DETECTION

In this chapter, we will focus on methods for hepatitis B (HepB) detection. We will then present our results demonstrating the potential of SP-IRIS for providing rapid HepB antigen detection at the single-molecule level.

4.1 Motivation for HepB detection

Hepatitis B viral infection is caused by hepatitis B virus (HBV). It is contagious through blood and body fluids, and attacks to the liver. HBV infection can lead to both acute and chronic disease, which are mainly acute hepatitis, fulminant hepatitis, chronic hepatitis, cirrhosis and liver cancer [119,120]. World Health Organization (WHO) estimates that HBV had worldwide significance with annual mortalities over above 880,000 in 2015 [121]. Moreover, WHO estimates that more than 257 million people had chronic HepB infection in 2015 [121]. Although an effective vaccine is available against HBV infection, it is still a global health problem that early diagnosis can be very beneficial for early treatment before the infection causes further liver diseases.

HBV screening tests carried for diagnosis of the disease or biological validation of the blood or blood components in patients and blood donors are done via [122]:

- Tests targeting the detection of a component of the virus (for instance, hepatitis B surface antigen (HBsAg) or HBV DNA),
- Tests looking for an antibody as a biomarker of the exposure to the virus (for instance, antibody against hep B core antigen (anti-HBcAg)),
- Tests looking for indirect results such as damage in liver (alanine

aminotransferase).

Among these screening strategies, the safest choice is detecting HBsAg, which is approved by the FDA for diagnostics. HBsAg is a reliable biomarker of viral hepatitis both for early detection of infection and for monitoring response to antiretroviral therapy. The HBsAg is the first protein that appears in the serum after the incubation period, which verifies acute HBV infection. In the first 1–12 weeks of infection, surface antigens start to be produced in patients. Both HBsAg and HBcAg are produced in excess amounts by the infected hepatocytes. Blood tests usually look for the viral DNA. Technological developments have led to recent new opportunities for testing and treatment. Chronic HBV infection testing or testing before transfusion is done by an initial serological test to detect HBsAg followed by nucleic acid amplification test (NAT) for detection of HBV DNA viral load to help guide treatment decisions [123]. One of the main and worldwide applied screening strategies is to test the sample for HBsAg which is used for the longest time and considered as the primary test by WHO [124].

4.2 Detection strategies and limitations of current HepB diagnostics

HBsAg can be detected using rapid diagnostic tests (RDTs) in lateral flow, flow-through or simple agglutination assay formats. Laboratory-based immunoassays to detect HBsAg include traditional radioimmunoassays (RIA), polymerase chain reaction (PCR), enzyme-linked immunoassays (ELISA), as well as newer technologies such as electrochemiluminescence immunoassays (ECLIA), microparticle enzyme immunoassays (MEIA) and chemiluminescent microparticle immunoassays (CMIA) [125]. These technologies are quite expensive, need established infrastructure. Hence, the development

of convenient, affordable and effective diagnostic technologies, which address medical needs in low-resource settings, is significant. Despite being widespread and heavily used, it is difficult to adapt to low-resource settings for these technologies because of their laborious and time-consuming structure [126]. The focus of this chapter is on the generation of an affordable and highly sensitive diagnostic assay for HepB detection. However, in order to better understand the limitations of commonly used technologies, we will go into details of the most common wet-bench techniques and rapid diagnostic tests in the next sections.

4.2.1 Enzyme-linked immunosorbent assay (ELISA)

ELISA is a type of solid-immunoassay and one of the most common serological diagnosis techniques used in HepB screening. Generally, commercial ELISA kits use monoclonal antibodies (mAbs), as well as polyclonal antibodies [127]. To detect HBsAg mutants, some assays are composed of multiple mAbs in the capture phase together with a polyclonal conjugate phase. Antigen sandwich ELISA kits rely on capturing and detecting the viral antigens in the patient sample. In sandwich HepB ELISA kits, a mAb against the target viral antigen is immobilized onto the microtiter plate surface. When the patient sample is added to the microwell plate, HBsAg is captured on the surface. The resulting antigen-antibody complex is tagged with another antibody on the surface. This antibody is specific to a different epitope of HBsAg and is linked to an enzyme, horseradish peroxidase (HRP). Then, the substrate for the enzyme, 3,3′,5,5′-tetramethylbenzidine (TMB), is added to the plate and the signal emitted from this reaction is measured using a microplate reader. Figure 4.1 shows the principle of ELISA test schematically [128].

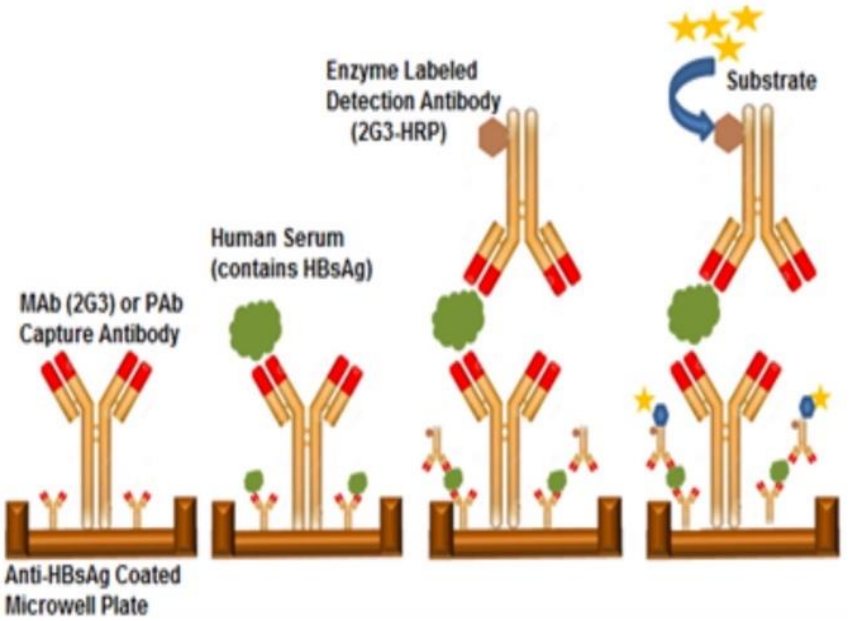

Figure 4.1 Diagram of antigen sandwich-ELISA for the detection of HBsAg. Adapted from [128].

Even though ELISA is widespread, it suffers from lengthy and complicated multi-step procedures requiring specialized personnel and equipment. These drawbacks pull it back from being used in the field. In addition, temperature-sensitive reagents required for the multi-step protocols make it difficult to adapt to low-resource settings. Furthermore, ELISA has limited sensitivity compared to other techniques and does not provide multiplexed testing.

4.2.2 Polymerase chain reaction (PCR)

PCR is based on nucleic acid amplification that can quantitatively detect minute amount of viral HBV DNA present in the sample after amplifying it. HBV is an enveloped DNA virus with unique features. It contains partially double-stranded DNA which replicates by reverse transcription of an RNA intermediate, the pregenomic RNA (pgRNA).

The DNA genome is extracted from the patient samples for PCR amplification using specific primers and DNA polymerase enzyme. PCR has been shown to have very sensitive and specific the detection of HPV [129,130]. However, HBV has a highly variable DNA genome which shows variations quite often with a much higher mutation rate compared to other DNA viruses [131,132]. The drugs used for the treatment of chronic HepB also cause mutations in the long-term. Therefore, increased sensitivity and accuracy are required. Real-time PCR is widely used for detection of HBV owing to its increased accuracy, wider linear range and reproducibility [129,133]. However, due to the mutations, a number of primers required for different genotypes may vary for accurate detection. If there is a mutation that causes a mismatch between primer or the probe of a commercial DNA quantification kit and the target HBV DNA, then the actual viral load of the sample might be underestimated. Furthermore, amplification and detection steps make the protocol about 6h long which is not very practical for the user. Commonly, these techniques are expensive, time-consuming, multi-step, including DNA extraction and require special equipment as well as specialized laboratory-settings and personnel.

4.2.3 Lateral-flow based tests

Lateral-flow assays are immunochromatographic tests which have a significant role among point-of-care (POC) testing techniques. They provide rapid and inexpensive detection of disease biomarkers [134,135]. Generally, lateral-flow assays contain a sample pad, conjugation pad and reaction membrane. They depend on the wetting of the sample pad with the sample and reacting with the colloidal nanoparticle on the conjugation pad and the changes in the colorimetric signal owing to the presence of the target in the sample

solution [136]. The nanoparticles are usually gold nanoparticles or fluorescently-labeled microbeads and the sensitivity of the lateral-flow assay depends on the amount of the particles captured and aggregated during the sandwich-type immunoassay. A typical lateral-flow immunoassay design and strip results are shown in Figure 4.2.

In many parts of the world, the rapid strip tests based on lateral flow immunoassay are currently the most commonly used HBV POC diagnostics [137,138]. Especially for the testing of chronic HepB virus infection, lateral-flow immunoassays are cost-effective in resource-limited areas. Moreover, it can be multiplexed for the simultaneous detection of HepB HBsAg, HBcAg and HepB [139]. However, since there are variations in accuracy and sensitivity among different brands or among the same brand's tests, lateral-flow assays still suffer from sensitivity issues [140].

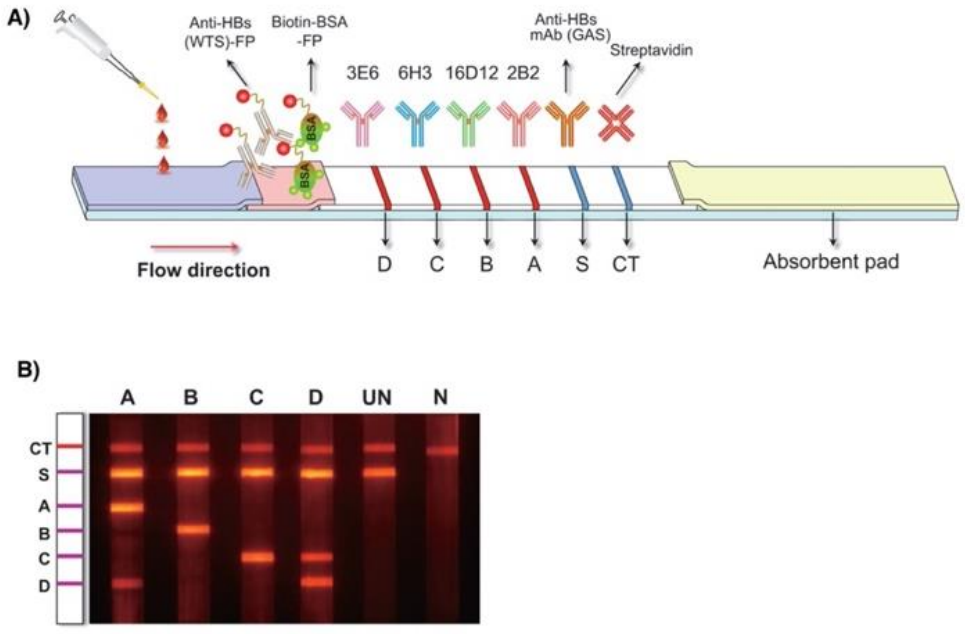

Figure 4.2 A) Representation of a lateral-flow assay for HepB detection and genotyping. B) The photographs of fluorescence imaging of the multiple assay strips using a customized luminoscope reader showing the genotyping results. Adapted with permission from Anal. Chem. 2015, 87, 10, 5173–5180. Copyright 2015 American Chemical Society [141].

Table 4.1 summarizes the diagnostic approaches for HepB detection mentioned so far. The recommended detection limit for HepB tests by the Food and Drug Administration of USA (FDA) is 0.5 ng/mL which is equivalent to 0.125 IU/mL [142]. Therefore, an ideal HepB detection system should be rapid, inexpensive, sensitive enough to meet the FDA's and WHO's recommendations, easy to apply at low resource settings.

Technique	Commercial brand (if any)	Target	LOD	Comments	Ref.
ELISA	na	HBsAg	0.5 to 0.7 ng/ml (0.125 – 0.175 IU/mL)	Serum samples. Intra-assay and inter-assay CV were found to be 3.96% and 5.85% for the designed assay and 4.5% and 9.29% for the commercial kit, respectively.	[143]
ELISA	na	HBsAg	1 ng/mL (0.25 IU/mL)	Antigen tested in 1% BSA-PBS. Sensitivity is not comparable with FDA standards.	[127]
Chemiluminescence (CMIA)	ARCHITECT® HBsAg QT Assay by Abbott	HBsAg all mutants and genotypes	5.2 mIU/mL	Undiluted serum sample. Automated. Chemiluminescence detection requires special equipment. Can test for mutation. 35 min assay time.	[144]
Electrochemiluminescence	Elecsys HBsAg II Assay by Roche Diagnostics	HBsAg	0.2 ng/mL (0.05IU/mL)	Undiluted serum sample. Automated. The total duration of the assay is 18 min.	[145]
RT-PCR	na	S and C regions of the HBV genome	47.6 ng/mL (11.9 IU/mL)	Blood sample. In good agreement with the Roche and Daan commercial PCR kits, however, underestimated a major amount of patient samples.	[129]
RT-PCR	Cobas HBV test using the Cobas 4800 by Roche	HBV genotypes	6.937 IU/mL	Plasma samples. Requires specialized instrumentation. FDA approved. Sensitive and accurate detection of all known genotypes and precore mutant.	[146]

PCR	RealTime HBV by Abbott	HBV Genotypes	10 IU/mL	Serum or plasma samples. Needs to be used with the Abbott *m*2000 System DNA reagents and with the Abbott *m*2000*sp* and *m*2000*r*t instruments for the quantitation. Best for chronically HBV-infected individuals	[147]
Lateral-flow assay	Determine HBsAg 2 by Abbott	Major HBsAg mutants	0.13 IU/mL.	The only rapid test used in plasma, serum and fingerstick whole blood to meet the minimum EU and WHO requirements	[125]
Lateral-flow assay	na	HBsAg and genotypes	10–40 ng/mL (2.5–10 IU/mL)	Serum or plasma sample. Can do genotyping. Assay duration 20 min and additional reading time. Not applicable to many genotypes due to the limitations of mAbs.	[141]
Lateral-flow assay	na	HBeAg, HBsAg, anti-HB	1 ng/mL (0.25 IU/mL)	Serum samples. Multiplexed and automated. Comparably cheaper than traditional ELISA and Abbott technologies. Quantitative POC.	[140]
Lateral-flow assay	na	HBsAg	0.06 ng/mL (0.24 IU/mL)	Tested the samples in PBS + 0.1% Tween 20 (PBST) buffer. Signal enhancement with nanoparticle modification in labeling. 10 min assay time. comparable results with ELISA.	[148]

Table 4.1 Comparison of current detection methods for HepB detection.

4.3 Objective

Our aim in this study is to develop a HepB immunoassay and verify the performance of SP-IRIS system to quantify hepatitis viral protein, HBsAg.

4.4 Experimental section

4.4.1 Reagents and Apparatus

HBsAg protein (Subtype ad – 30-AH15), polyclonal anti-HBsAg antibody (Subtype ad/ay – 70-HG15S), monoclonal anti-HBsAg antibody (10-H50A) were obtained from Fitzgerald Industries International (Acton, MA). MCP-2 copolymer from Lucidant Polymers (Sunnyvale, CA, USA)were used for chip surface functionalization. For antibody functionalization, 15 nm by 40 nm carboxyl-modified gold nanorods – OD50 (carboxyl-PEG5000-SH) (CGC5K-15-50) were purchased from Cytodiagnostics, Inc. (Burlington, ON Canada) for dry measurements. 25 by 71 nm carboxyl gold nanorods (C12-25/650-(carboxyl)-(50)) were purchased from Nanopartz Inc. (Loveland, CO) for in-liquid measurements. Protein dilutions were done in stain buffer which contains 2% fetal bovine serum (FBS) and <0.09% sodium azide (BD Biosciences, San Jose, CA). For antibody-gold nanorod (GNR) conjugation, 1-ethyl-3-[3-dimethylaminopropyl] carbodiimide hydrochloride (EDC), N-hydroxysulfosuccinimide (sulfo-NHS), blocker bovine serum albumin (BSA), trehalose for spotting stability, activation buffer 2-(N-morpholino) ethanesulfonic acid (MES) buffer (10 mM, pH 5.5), coupling buffer 1x phosphate buffer saline (PBS) (pH 7.4), surfactant for washing buffer 10% Tween-20, ethanolamine for blocking the chips after spotting and Tris-HCl buffer (pH 9.0) were purchased from Sigma Aldrich (St. Louis, MO).

NanoDrop 2000c Spectrophotometer from Thermo Fisher Scientific (Waltham, MA) was used for characterization of nanoparticles. Scienion S3 SciFlexArrayer (Berlin, Germany) spotter was used to create an array of antibody surface probes. Hamilton PHD 2000 syringe pump was used in liquid experiments.

4.4.2 Conjugation of GNRs with anti-HBsAg antibody

Conjugation of the antibody to gold nanorods was achieved via covalent attachment of antibodies to nanorods using carbodiimide chemistry [149]. In this approach, antibodies are covalently bound to the rods through primary amine groups. Zero-length crosslinker EDC and stabilizer NHS were used to have the covalent conjugation [150,151]. First, carboxyl groups on nanorods were activated with EDC and a stabile succinimide ester were formed with NHS; therefore, nanorods were ready to conjugate with the amino groups of the antibodies yielding a stable amide bond. GNR suspension was used as OD50 in pure water. Prior to the conjugation, fresh EDC/NHS mix solution in MES buffer was prepared at 30 and 36 mg/mL concentrations, respectively. 10 µL of GNR in water was mixed with 10 µL of EDC/NHS solution and incubated for 30 min at room temperature. Washing buffer was prepared as 1xPBS with 0.05% Tween-20 (PBST). 1 mL PBST was then added to the GNR mixture. The mixture was vortexed thoroughly and centrifuged down at 6500 g for 30 min. After removing supernatant, 10 µL of polyclonal anti-HBsAg antibody at 1 mg/mL concentration in PBS was added to the solution and incubated at 4 ºC overnight. Next day, 1 mL of 0.1x PBST was added into the solution and the solution was centrifuged at 6500 g for 30 min. Finally, to block the possible remaining active sites on the surface of GNRs, 50 µL of 0.1x PBST with 1% BSA was added to the solution. The conjugation was

characterized and confirmed using a spectrophotometer. The mixture was then washed with PBS and stored at 4 ºC for further use.

4.4.3 Fabrication of SP-IRIS microarrays

IRIS chips were cleaned by sonicating in acetone, rinsed with isopropanol and DI water and dried under nitrogen. They were functionalized with the copolymer MCP-2 from Lucidant Polymers. Anti-HBsAg antibodies were used to capture HBsAg on the IRIS substrate. Scienion sciFLEXARRAYER S3 piezoelectric robotic arrayer was used to create an array of antibodies. Antibodies were spotted at a concertation of 3 mg/mL in PBS with 25 mM D(+) trehalose. BSA was used as the negative control probe and spotted at 2 mg/mL concentration along with the antibody spots. The periodicity of the spots and the humidity in the spotting chamber (set to 57%) were optimized in order to prevent merging of neighboring spots. The antibodies were spotted periodically onto the chip by the spotter. A microarray pattern was designed for twelve replicate spots for each protein. The space between the spots (pitch) was set as 250 μm. After spotting, the antibody-spotted chips were kept in the spotter chamber at 67% humidity overnight at room temperature to allow time for the antibodies to immobilize on the surface. Following the immobilization, the chips were incubated in blocking solution of 0.1 M Tris buffer with 50 mM ethanolamine (pH=8.5) for 1 h to quench the excessive NHS groups left after immobilization. NHS groups are active for further possible reactions. Therefore, it is important to block them after the completion of immobilization. Otherwise, it may cause further crosslinking; thus, a decrease in the efficiency in protein immobilization due to the less availability of the probes or proteins. Then, the chips were washed with 1xPBST for 5 min following with

1xPBS rinse. The spotted chips were kept in a desiccator under vacuum until further use.

4.4.4 Assay procedure

After blocking, washing and drying, HBsAg detection was done in a heterogeneous assay format. The IRIS protein microarrays were first incubated with HBsAg ad protein diluted in stain buffer (FBS) for 2 h. Incubations were performed in 24-well plates with 250 μL of sample solution per well. Chips were washed just once with PBS for 1 min and dried. Chips were then incubated at room temperature on the orbital shaker with the antibody-functionalized GNRs in PBS for 2 h at a concentration of about 10 picomolar (10^8 particle/mL), again in a 24-well plate. Finally, chips were washed twice in PBS or 2 min each, dried, and imaged endpoint as described in Chapter 2. In-liquid measurements were done in homogeneous fashion in the microfluidic chamber where the antibody-GNR conjugates were mixed with HBsAg prior to the incubation. Incubation was done in the microfluidic chamber while real-time tracking the particle binding.

4.5 Results and discussion

4.5.1 Nanorod label selection

The initial step for the development of an immunoassay that utilizes gold nanorods for single-molecule counting is to functionalize gold nanorods that are stable and provide a strong optical signal. The selection procedure was described in Chapter 2. We have conducted the conjugation experiments primarily with 15x40 nm rods. In addition to these nanorods, 25x70 nm rods also provide plasmonic resonance at red wavelength and good visibility (SNR) with polarization enhancement and used in-liquid experiments.

To decrease steric hindrance and improve diffusion of the nanorod to the surface of

the sensor, the smallest detectable nanorod is desirable. Very small nanoparticles are not stable enough in protein conjugations. The antibody-GNR conjugate is not very durable when smaller nanorods are used for conjugation. Also, small nanorods do not provide sufficient optical signal for a high SNR. On the other hand, while large nanorods provide great SNR, they suffer from aggregation after protein conjugation in protein assays. Since antibody-GNR conjugate stability is durable with 15x40 nm nanorods and provides enough detectable signal, 15x40 nm GNRs were selected for dry measurements. Note that, to increase the visibility in liquid measurements, 25x71nm GNRs are preferred. The same protocol for conjugation is used. Initial experiments demonstrated that a nanorod with nominal dimensions of 15x40 nm was imaged with an SNR of 15 (with 20X magnification SP-IRIS system), while 25x71nm GNRs have that of 25. Even though the 25x71 nm have a higher SNR, the 15x40 nm rods were chosen for further development of the protein detection assay in dry experiments because they are smaller in size and are more stable with fewer aggregates. Figure 4.3 shows images of 15x40 nm and 25x71 nm nanorods that have an SNR of 15 and 25, respectively.

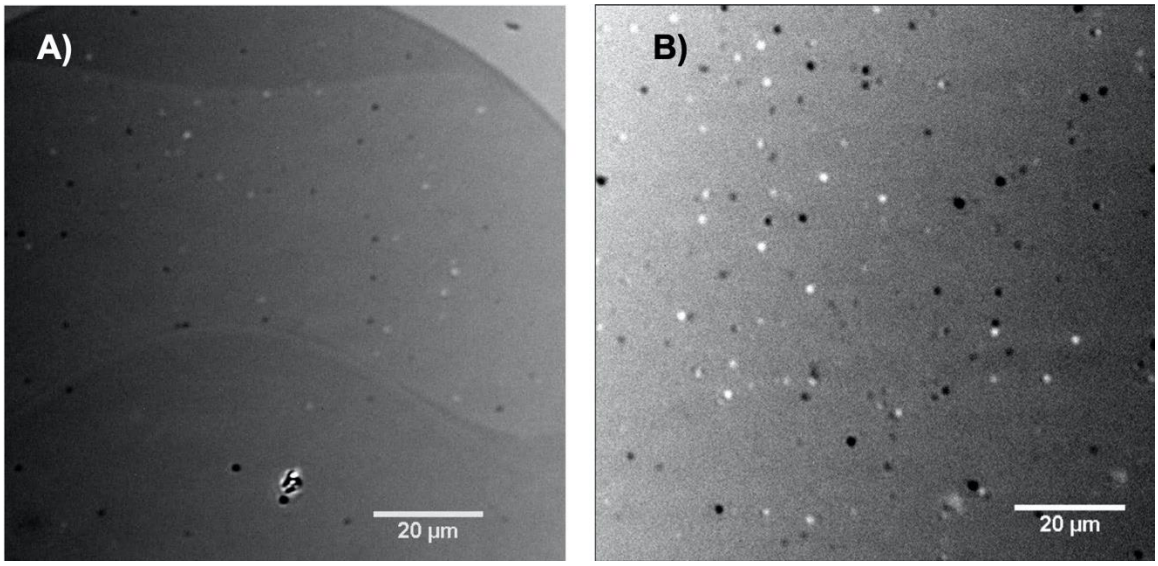

Figure 4.3 SP-IRIS images of A) 15x40 nm rods and B) 25x71 nm rods captured on antibody spots.

4.5.2 Development of SP-IRIS protein assay

We have developed a microarray-based immunoassay for the detection of hepatitis B surface antigen from FBS. This protein detection differs from some viral diseases where detecting the presence of the virus is all that is needed and can be accomplished through nucleic-acid amplification. Here, we constructed an assay that consists of antibodies against HBsAg. Figure 4.4 is a schematic showing the preparation of the immunoassay. Pre-immobilized antibodies are used in antigen capture on the sensor and secondary antibody-conjugated gold nanorods are used for labeling.

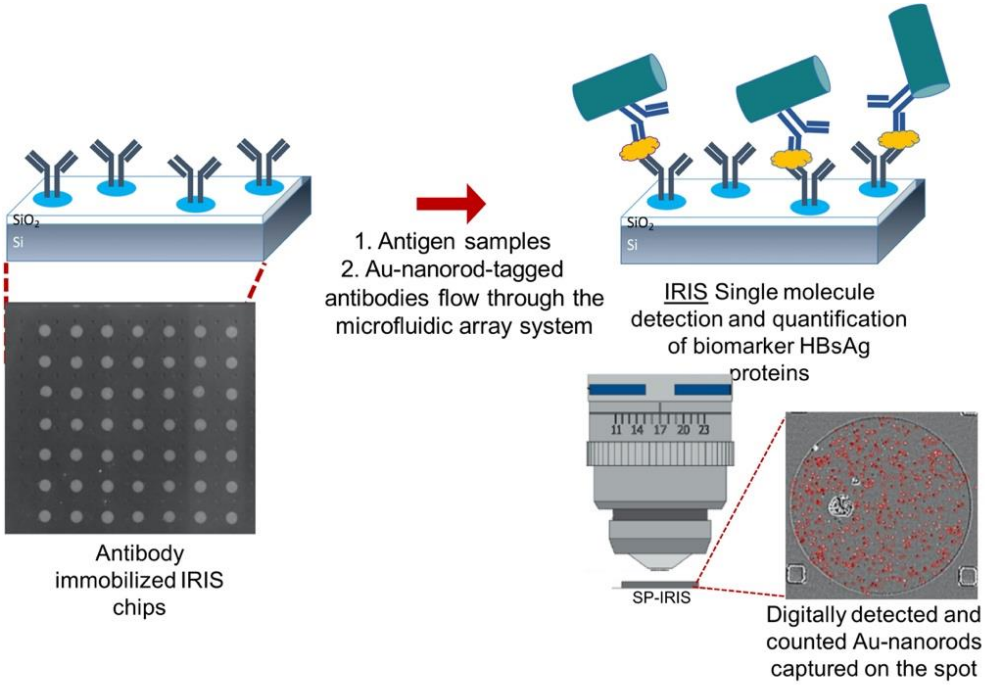

Figure 4.4 Schematic representation of the HBsAg microarray preparation and data collection processes.

Antigen-antibody binding assays can be done in a heterogeneous or homogeneous fashion. The former scheme requires a separation step where the bound analyte stays on the chip surface through capture probes and the unbound analyte gets removed with a wash step. On the other hand, the latter one is a single-step process and there is no separation step [152]. Heterogeneous assays provide the advantage of a removal of the substances which may cause non-specific interactions during the experiments. It is also advantageous for complex systems where multiple and large target molecules are present. However, it adds up a washing step as a separation step. Homogeneous assays are usually preferred for the detection of small analytes since they rely on the changes as a result of binding, such as changes in confirmation or rotational movement of a surface probe [152]. They suffer from the interference effect of the media used in the assays.

Here, we experimented with both heterogeneous and homogeneous approaches for our assay design. Figure 4.5 shows the steps for our immunoassay for HBsAg detection. In homogeneous assay scheme, HBsAg antigen was mixed with antibody-GNR conjugate in FBS prior to the experiments. The mixture is added onto the capture antibody spotted-chips and the chips were incubated for 2h at room temperature. After washing the chips with PBS and drying them, endpoint dry measurements were done. They were imaged using polarization-enhanced SP-IRIS using 10x / 0.3 NA objective. Six FOVs were scanned and stitched together, and the image in Figure 4.5 was obtained. This was completed in less than 10 min. Moreover, using SPANDEX custom software, the particles on every spot were detected and counted in 3 min as shown in the last image in Figure 4.5. We take the images with SP-IRIS and load them to SPANDEX, the software automatically identifies the spots in the image and counts the number of targets bound to each condition.

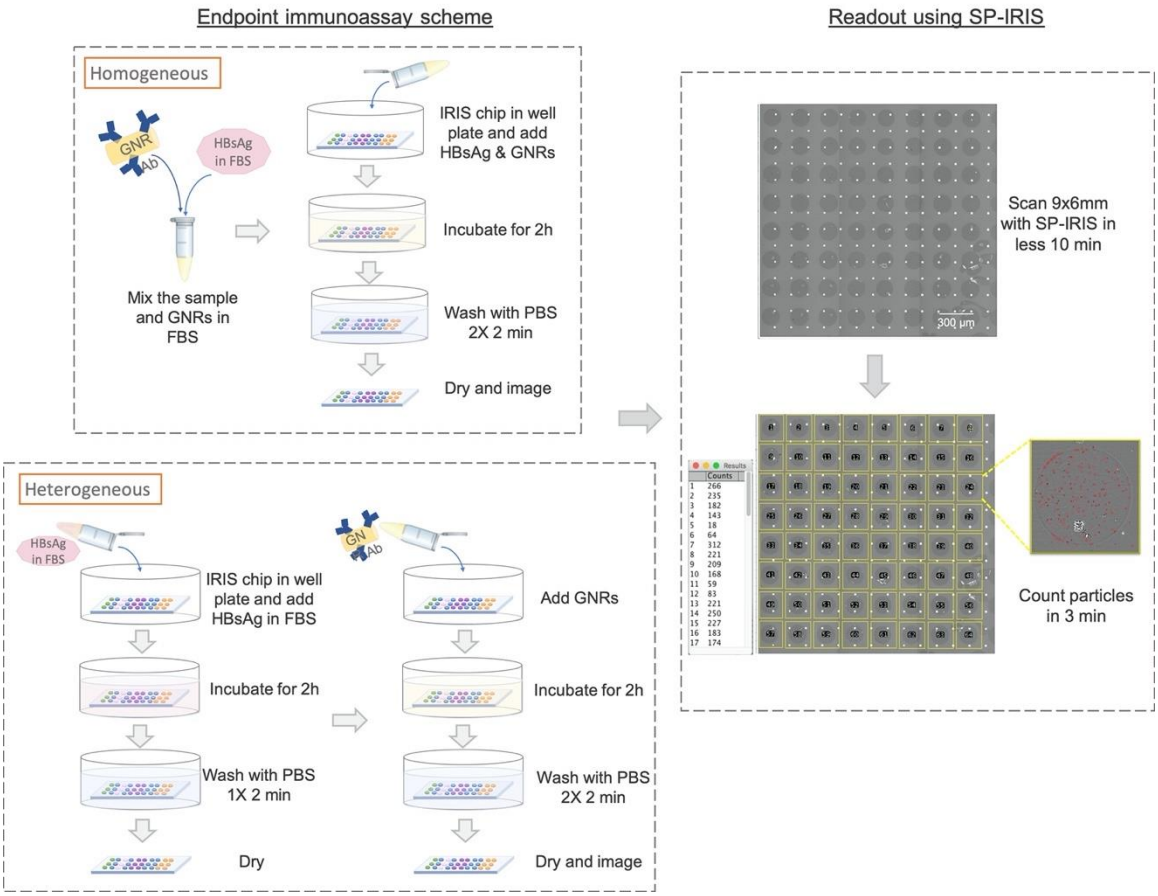

Figure 4.5 Assay scheme representation for incubating samples and collecting results with SP-IRIS in two different assay approach

We compared homogeneous and heterogeneous assay approaches in detection of 0.1, 1.0, 10 ng/mL HBsAg detection. GNR concentration was kept constant in the experiments as 10^8 particles/mL. We observed excess binding on negative control spots (BSA spots) in homogenous assays. Additionally, at lower concentrations, homogenous assay did not reveal a distinguishable signal. Therefore, we selected the heterogeneous scheme for the rest of the microarray development.

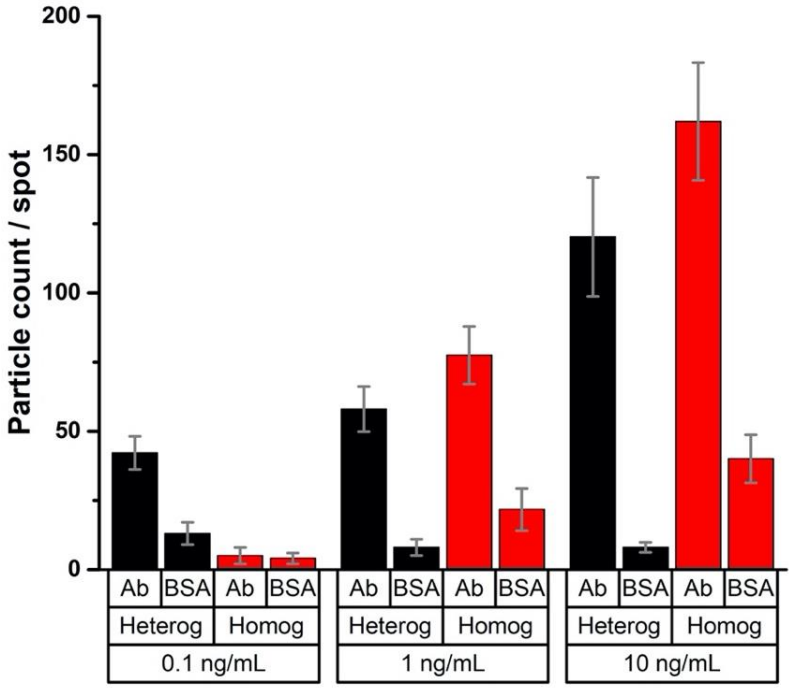

Figure 4.6 The comparison of heterogeneous and homogeneous HBsAg immunoassays. Particle counts were recorded in homogenous (red columns) and heterogenous (black columns) assays on antibody (Ab) and negative control (BSA) spots. The error bars show the standard deviation for n=5 replicate spots.

4.5.3 Optimization of assay conditions

Assay conditions were optimized to maximize the signal and minimize non-specific binding in FBS. 3.0 mg/mL was found to be the optimum antibody concentration for spotting which yielded the best spot morphology, homogeneity and protein capture efficiency in binding experiments.

The buffer used for washing after GNR labeling affects the sensitivity. as wash buffer, PBS, PBS with 0.1% Tween-20 (PBST), PBS with 0.05% BSA (PBSB) and PBST with 0.05%BSA (PBSTB) were used. Figure 4.7A compares the particle counts for 1 ng/mL HBsAg detection. PBS was chosen as the wash buffer.

To determine the ideal incubation time, particle counts were measured as a function of incubation time for the antigen. The maximum particle count was obtained at 120 min incubation of 10 ng/mL HBsAg and 2h was selected as the optimum antigen sample incubation time.

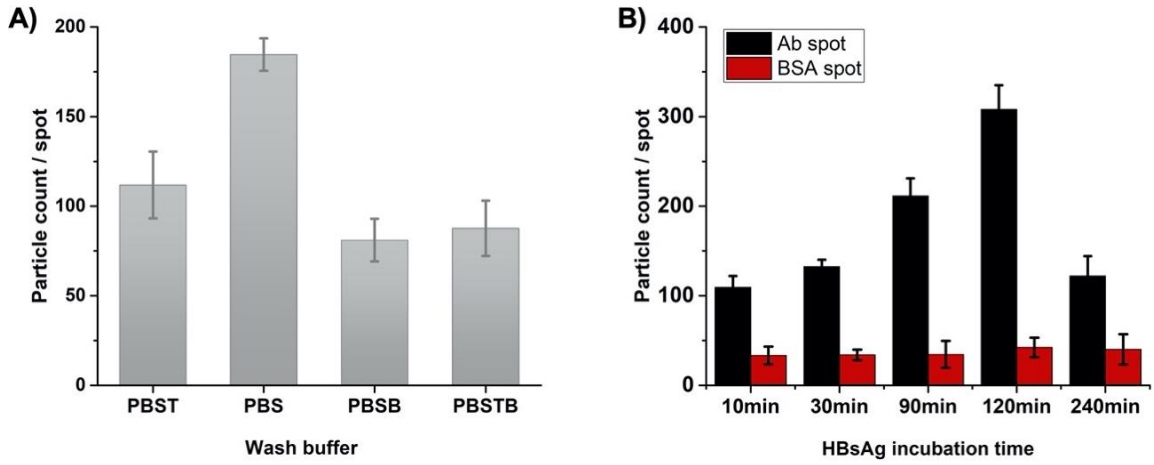

Figure 4.7 A) Effect of wash buffer used after labeling of 1 ng/mL HBsAg-incubated chips. B) Effect of HBsAg incubation time for 10 ng/mL HBsAg. The error bars show the standard deviation for n = 5 replicate spots.

4.5.4 Calibration curve and analytical characteristics

At optimum conditions, quantitative analysis of HBsAg was conducted in FBS for concentrations ranging from 0.1 pg/mL to 100 ng/mL. Figure 4.8A shows average particle counts per antibody and BSA (negative control) spots as a function of antigen, HBsAg, concentration. An HBsAg concentration of 0 in the plot corresponds to blank FBS sample incubation. To obtain the average particle count per spot (about 150 µm in diameter), we first sum the particle counts on every six antibody spots and then obtain the average of the summations on each IRIS chip for three chips. The standard deviations of all the summation counts on each chip are shown as error bars for the corresponding sample concentration.

As depicted in the plot, the average particle counts for the antibody spots increased with increasing HBsAg concentration consistently, while the counts on the control spots remained relatively the same. Figure 4.8B shows log-log plot of the calibration curve of the particle counts versus HBsAg concentration. It was well fitted by a linear relationship from 0.1 pg/mL to 100 ng/mL with a correlation coefficient of R^2=0.98 and the linear regression equation of y = 0.1721x + 1.8482. The limit of detection (LOD) was found as 0.072 pg/mL which corresponds to 0.29 mIU/mL. The LOD was calculated using the mean and standard deviation of blank samples to set the limits as done in the previous studies [153,154]. The assay's coefficient of variation was about 13%. These analytical characteristics represent the ability of our ultra-sensitive microarray for reliable detection of HBsAg within the whole range of clinically relevant concentrations.

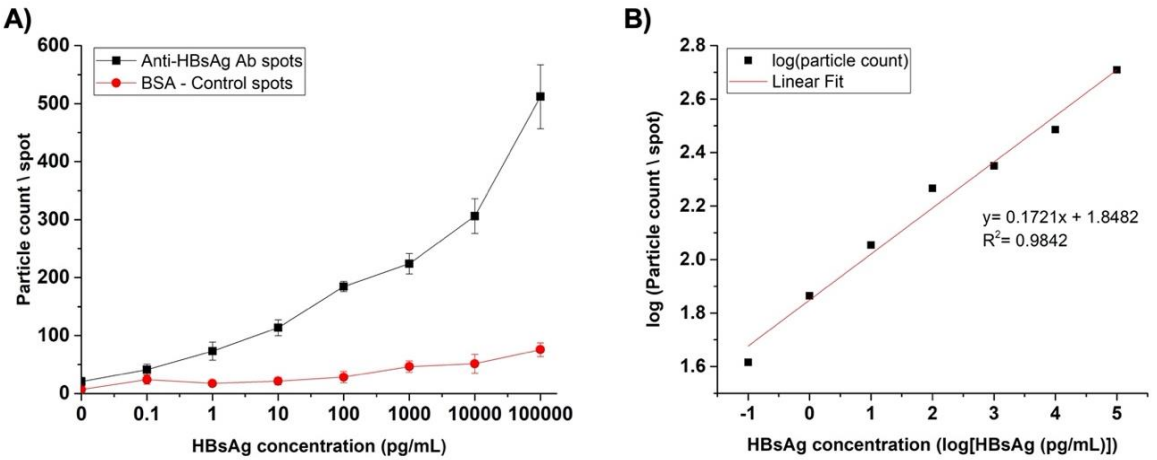

Figure 4.8 A) The calibration plot for HBsAg detection on anti-HBsAg ab spots (n=18). B) log-log plot of the average particle counts per spot for antibody spots based on HBsAg concentration.

When our immunoassay is compared to the commercial assays in Table 4.1, even though our assay has a superior sensitivity for HBsAg, detection time becomes limiting. It is still very efficient, takes a shorter time than a PCR application and comparably sensitive. Nevertheless, we need an assay that provides both sensitive and rapid detection. Therefore, we have developed an in-liquid assay for HBsAg detection. The antibody-printed chips were placed in the microfluidic chamber mentioned in Chapter 3 after assembling the AR-coated cover glass using a double-sided spacer. Homogeneous assay scheme was followed. Prior to the experiments, HBsAg was mixed with GNRs in FBS and loaded in a syringe. The mixture was injected into the microfluidic chamber by a syringe pump at a flow rate of 5 µL/mL for 2 h. Real-time particle detection was done while chips were incubated in the chamber with 10,100 pg/mL and 1 ng/mL of HBsAg. Figure 4.9 shows the binding curves for HBsAg-ab-GNRs at different concentrations. Note that the curves show the cumulative binding of the conjugates in the given time, therefore, the total binding may differ from the stationary calibration curve depicted in Figure 4.8 which represents the total counts at antigen-ab-GNR equilibrium at the end of 2h incubation. The results show that by comparing the binding rates, we can accomplish quantitative detection in 20 min. However, at lower concentrations than 10 pg/mL, we were not able to collect distinguishable data and this method was not found as sensitive as the endpoint immunoassay measurements.

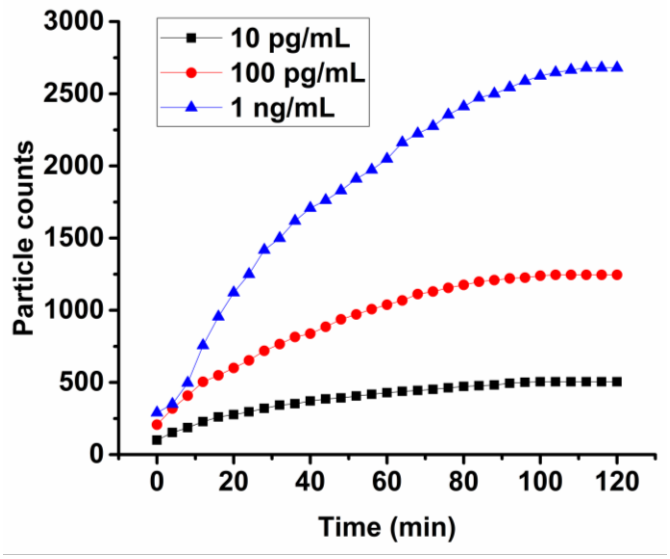

Figure 4.9 Real-time particle counts for 10,100 pg/mL and 1 ng/mL HBsAg samples in stain buffer.

4.6 Conclusions and future directions

SP-IRIS digital microarray can be used to quantify proteins with high sensitivity. We developed a simple microarray and demonstrated the highly sensitive quantification of HBsAg. The assay can be used to detect HBsAg in the range from 0.1 pg/mL to 100 ng/mL. We anticipate that we can develop multiplexed microarrays for simultaneous detection of many proteins and molecules on the same chip, such as detecting mutations in HepB. The wide surface area enables spotting many antibodies in a number of replicates. Therefore, we can still have multiple antibodies for different analytes and many replicates for high sensitivity. As future work, we anticipate validating the microarray performance by correlating with ELISA both in artificial and real patient samples. Also, we can further adopt different antibody immobilization techniques, such as DNA-directed immobilization or oriented immobilization, for better sensitivity in real-time measurements. .

5 CHAPTER FIVE DIGITAL MICROARRAYS FOR NUCLEIC ACID DETECTION

In this chapter, we will focus on single nucleic acid counting using SP-IRIS. This capability allows SP-IRIS to detect nucleic acids at sub-femtomolar concentrations. Single molecule detection offers very high sensitivity and specificity. We demonstrate feasibility of nucleic acid detection with SP-IRIS in microRNA and rare mutation (*KRAS* gene) detection.

5.1 Motivation for single-molecule analysis of nucleic acid biomarkers

Nucleic acids are significant biomarkers for disease detection, monitoring, and treatment. Nucleic acid biomarkers have become widespread and regularly used for detection of from cancer to neurodegenerative diseases thanks to the advances in technologies enabling their discovery and clinical implementations [155,156]. Therefore, sensitive and specific detection of nucleic acid biomarkers in clinical applications is essential.

Figure 5.1 gives a brief overview of types of nucleic acid biomarkers [157]. Commonly, the analysis of DNA biomarkers include detection of single nucleotide polymorphisms (SNPs), variations in genomic sequence or mitochondrial pathogenic DNA [158–160]. DNA biomarkers can be found in cells or in cell-free DNA (cfDNA) form in blood or other biological fluids. Each cell has two copies of DNA. If the affected gene is only on one of the copies, then the target DNA amount is even less. On the other hand, when the cfDNA is released into the blood stream through apoptosis or necrosis of cells, it gets very diluted in this medium and even more dilute when it reaches to other body fluids.

The total amount of cfDNA in plasma was reported as less than 10 ng/mL [161]. Therefore, tools to detect low copy number DNA in biological samples must be very sensitivity. Moreover, the analysis requires high specificity due to the complexity of the human genome, and long and repetitive regions in gene sequences.

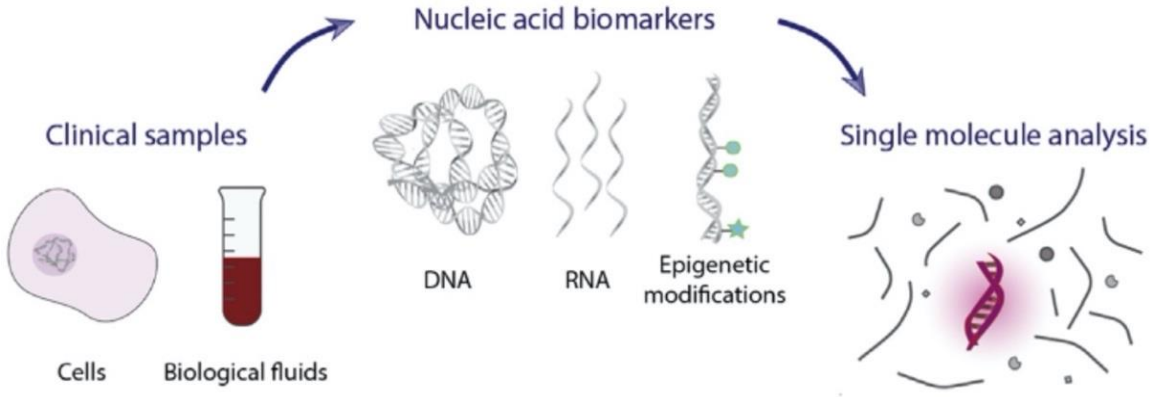

Figure 5.1 An overview of types of nucleic biomarkers. Reprinted from Anal. Chim. Acta., 1115, T. Gilboa, P.M. Garden, L. Cohen, Single-molecule analysis of nucleic acid biomarkers – A review, 61–85, Copyright 2020, with permission from Elsevier [157].

RNAs behave as transmitters for genetic information in cells and regulate transcriptional and post-transcriptional processes [162]. Most common RNA biomarkers are messenger RNAs (mRNAs) and non-coding RNAs such as microRNAs (miRNAs). They are used for disease detection and gene expression profiling. Recently, it has been shown that not only the presence/absence of a gene but also expression level of a particular gene can also be indicative for a disease and its stage [163,164]. Therefore, RNA quantification becomes crucial to track the minute changes. However, since mRNA or miRNA are present in a cell at very low copy numbers form couple copies to only hundreds [165]. For instance, short non-coding miRNAs are usually present in plasma samples in

the femtomolar range [166]. Therefore, it is required to have ultra-sensitive tools for RNA detection and quantification.

Table 5.1. shows the comparison of three types of biomarkers, DNA, RNA and protein, mentioned in Chapters 4 and 5. Their relative amounts in biological samples and conventional detection techniques can be found in the table [167].

	DNA	**RNA**	**Protein**
Biological function	Carrier of genetic information	Transmitter of genetic information	Catalyst, regulatory factor, structural component.
Amount per human cell	~6 pg	10~30 pg	130~150 pg
Amount in 1 mL plasma	1~1000 ng	1~1000 ng	~6 × 104 ng
Features as biomarker	Mutation, epigenetic modification	Expression profile	Abundance; proteomics profile
Accuracy and specificity	Relatively higher	Relatively higher	Relatively lower (mostly rely on good antibody being found)
Detection methods	qPCR, DNA-seq, microarray	RT-qPCR, RNA-seq, microarray	Mass spectrometry, immunoassay, electrophoresis

Note: Reprinted from [167].

Table 5.1 Comparison of macromolecular biomarkers.

5.2 Conventional methods for nucleic acid analysis and their limitations

The most common nucleic acid analysis tools can be classified in two groups: 1. Tools based on sequencing techniques and 2. Tools based on labeling such as fluorescent tags.

The first group of nucleic acid analysis includes next-generation sequencing (NGS), which is most commonly used, Sager sequencing and pyrosequencing [168–170]. The latter two are used for research applications. NGS is generally used to in clinical settings to detect and identify mutations or detect pathogens related with infectious diseases. NGS platforms perform sequencing of millions of small fragments of DNA in parallel. The main drawback of NGS is the requirement of high capacity infrastructure such as computer capacity, data storage, personnel expertise for data collection, analysis and interpretation to obtain clinically relevant information [171].

The second group for nucleic acid analysis consists of dyes or labels that are specific to single-stranded DNA or RNA, or double-stranded DNA. One commonly used tool is gel electrophoresis which requires great amount of sample, gives information about fragment length and does not provide information about sequence. Other most commonly used techniques rely on hybridization of labeling probes to the target sequences. Therefore, they require knowledge of the target sequence beforehand to generate the labels. These detection tools involve Northern and Southern blots and microarrays. Northern and Southern blots are used for RNA and DNA detection, respectively. They have an additional labeling step on top of gel electrophoresis [172,173]. Microarrays are used for both DNA and RNA detection. Microarrays have multiplexing capacity, nevertheless, they suffer from limited

dynamic range, sensitivity and specificity issues [174].

The gold standard for nucleic acid analysis is quantitative PCR (qPCR) or real-time PCR [175,176]. qPCR amplifies several copies of target simultaneously and utilized fluorescent dyes with high affinity towards double stranded DNA to produce a signal by the end of amplification. Due to amplification bias, quantification is limited.

5.3 Objectives and dynamic tracking approach

We propose development of a single-molecule detection technique for DNA and RNA that is label-based rather than amplification-based, and can be used to probe any number of different target nucleotide. The primary outcome of this work is the design and implementation of a new type of molecular assays which are SP-IRIS digital microarrays for nucleic acids. SP-IRIS nucleic acid assays are conceptually very similar to conventional DNA microarrays, whereas they provide digital counting of the number of captured molecules.

In the first section (Section 5.4) we introduce a digital microarray for miRNA detection. In the second section (Section 5.5), we develop a microarray for rare mutation (*KRAS* gene) detection.

Although both miRNAs and DNA with rare mutation present in biological samples with a very low abundancy, they are promising molecular biomarkers for diagnostic information. However, as discussed above, leading technologies are limited by the affinity of low abundant molecular biomarkers. In order to achieve high sensitivity with low abundance biomarkers (high-affinity), and differentiate them from high-abundance, low-affinity (non-specific background), kinetic assay with single-molecule readout is an

excellent solution. This can be accomplished by monitoring and detecting individual binding events while the assay is running. In this technique, individual binding of nanoparticle-labeled target biomarkers to the microarray surface is tracked throughout the assay. Duration of individual binding events are measured. Hence, high-affinity, low-abundance biomarkers can be distinguished from the background non-specific binding. Dynamic tracking of single binding events beats the reaction limits of biosensor sensitivity. In this dissertation, we apply this technique to two assays for better sensitivity and specificity.

5.4 Digital microRNA microarray: Real-time digital detection of individual microRNA with attomolar sensitivity

MicroRNAs are small, non-coding RNA molecules containing ~18–25 nucleotides. MiRNAs are crucial in cellular processes and their potential as diagnostic and prognostic biomarkers is enormous. MiRNAs function mainly by binding specific target mRNAs to alter protein translation [177]. The first miRNA was discovered in *C. elegans* in 1993 by Lee and colleagues [178]. Currently, more than 1900 human miRNAs are reported to be linked to human [179,180]. Increased or decreased levels of specific miRNAs have been shown to link with pathological processes. They have been found to be relevant to viral [181,182] and bacterial [183] infections, as well as non-infectious diseases such as cardiovascular disorder [184] and cancer [185].

Global detection methods used for sensitive detection of mRNA with about 20,000 copy per tissue fail when they are used for miRNA detection due to their low copy number, about 100 in a cell [186]. Ultra-sensitive and selective detection of miRNA biomarkers

present in a complex clinical matrix, such as blood, plasma, or serum is significant for diagnostic applications. However, since absolute miRNA copy number per sample volume is very small (in fM range), the technique used to detect miRNAs must be very sensitive and able to work with small sample volumes to be clinically effective. Moreover, due to their short and similar structures, it is hard to achieve selective and specific detection.

Here, we selected two fairly abundant miRNA, miR-451 and miR-223, for our proof-of-concept assay development applications. MiRNA-451 plays a role in tumorigenesis, tumor suppression, self-renewal and chemoresistance in many types of cancer, such as breast, gastric and colorectal, and has been implicated as a diagnostic and prognostic biomarker [187]. MiR-223 can be upregulated or downregulated in the cells. Its expression is deregulated during influenza or hepatitis B infection and in inflammatory bowel disease, type 2 diabetes, leukemia and lymphoma and upregulated in recurrent ovarian cancer [188]. We evaluated the potential application of SP-IRIS in quantitative detection of miR-451 and miR-223.

5.4.1 Experimental section

5.4.1.1 DNA probe design

Synthetic miRNAs and synthetic, custom-designed ssDNA oligonucleotide surface probes were purchased from Integrated DNA Technologies (IDT) (Coralville, IA). Table 5.2 shows the sequences for miR-451 and miR-223, and their complementary surface probes. The a and 5p sequence types were selected for miR-451 and miR-223, respectively. Surface probes were amine-functionalized and “AmMC6” indicates amine functionalization for covalent binding to the copolymer-coated IRIS chip, while GNR label

sequence was thiol-modified and “ThioMC6” indicates thiol functionalization for nanorod conjugation, as provided by IDT. The surface probes also have a double-stranded ‘stabilized’ region between the surface and the complementary region to accelerate hybridization.

Name	Sequence
miR-451a	**AAACCGUUACCAUUACUGAGUU**
Surface probe (SP) for miR-451	**AACTCAGTAATGGTAACGGTTT**TAGGACTAGGACTTGAAGTTGAAGTTTT /3AmMC6T/
miR-223-3p	**UGUCAGUUUGUCAAAUACCCCA**
Surface probe (SP) for miR-223	**TGGGGTATTTGACAAACTGACA**TAGGACTAGGACTTGAAGTTGAAGTTTT /3AmMC6T/
SP Stabilizer sequence	CTTCAACTTCAAGTCCTAGTCCTA
Non-complementary surface probe (Control)	/5AmMC6/ ATATGTACCCACCGCTATTCCAGTCTGTTCATTCGTAGGC
GNR label sequence	/5ThioMC6-D/ TTTTTTTTTTTTTTTTT

Table 5.2 Sequences for miRNAs and their complementary surface probes.

5.4.1.2 Reagents and apparatus

Dithiothreitol (DTT) was obtained from Sigma-Aldrich (Woodlands, TX, USA). NAP-10 columns for DNA purification were purchased GE Healthcare. Citrate-capped nanorods (OD1) with a longitudinal surface plasmon resonance peak at 650 nm and nominal dimensions 25 nm by 71 nm were used (Nanopartz Inc, Loveland, CO, part number A12- 25-650-CIT). MCP-2 and MCP-2F copolymers were purchased from Lucidant Polymers (Sunnyvale, CA, USA) and used for chip surface functionalization. All

other chemicals were purchased from Sigma-Aldrich.

NanoDrop 2000c Spectrophotometer from Thermo Fisher Scientific (Waltham, MA) was used for characterization of nanoparticles. Scienion S3 SciFlexArrayer (Berlin, Germany) spotter was used to create an array of DNA surface probes. Hamilton PHD 2000 syringe pump was used in liquid experiments.

5.4.1.3 GNR- PolyT conjugation

GNR-polyT conjugates were prepared with slight modifications to previously described methods [189,190]. Prior to conjugation, thiol-modified polyT oligonucleotides were treated with DTT to cleave the disulfide bonds and to activate thiols. 20 µM thiol-polyT was prepared in 170 mM phosphate buffer pH 8.0 and mixed with 100 mM DTT. The solution was kept in dark at room temperature for 3 hours occasionally vortexing. PolyT oligos were then desalted and purified using NAP-5 column according to the manufacturer's directions. Meanwhile, 6 mL of nanorods (OD1, approximately 10 pM) were centrifuged at 1500 rcf for 15 min and resuspended with DI water in a glass container. Immediately after obtaining polyT from the column, the purified oligonucleotides were quantified by measuring their absorbance at 260 nm using a NanoDrop spectrophotometer. GNRs and oligos were mixed in the container and placed on an orbital shaker for 30 min. Then, to bring the pH of the solution to pH 3, concentrated citrate buffer was added up to a final concentration of 10 mM citrate. Same way, tween-20 was added to have a final concentration of 0.1% w/v. After vortexing and sonicating, the solution was rested on the orbital shaker overnight. In the next 24 h, the salt concentration of the solution was brought up to 150 mM by slowly adding citrate buffer with high concentration of NaCl. Salt

addition was followed with another overnight resting. Finally, the nanorods were washed three times with PBS with 0.1% tween-20 to remove the excess, unbound oligos. The conjugation was confirmed by spectrophotometric analysis. The GNR-polyT conjugate was kept in PBST solution in a dark place for up to 2 months at room temperature for further use. Before every use, the conjugate was washed once again to remove the surfactant.

5.4.1.4 Fabrication of SP-IRIS microarrays

IRIS chips were cleaned by sonicating in acetone, rinsed with isopropanol and DI water and dried under nitrogen. They were functionalized with the copolymer 5% MCP-2F containing MCP-2 copolymer from Lucidant Polymers. Complementary and control surface probes were spotted on the IRIS chips in an array format using Scienion sciFLEXARRAYER S3 piezoelectric robotic arrayer. Oligonucleotide ssDNA surface probes were spotted at a concentration of 20 μM in 150 mM phosphate buffer. The periodicity of the spots and the humidity in the spotting chamber (set to 67%) were optimized in order to prevent merging of neighboring spots. A microarray pattern was designed for sixteen replicate spots for each DNA. The space between the spots (pitch) was set as 200 μm. After spotting, the DNA-spotted chips were kept in the spotter chamber at 67% humidity overnight at room temperature to allow time for the amine-modified ssDNA surface probes to immobilize on the surface. Following the immobilization, the chips were incubated in blocking solution of 0.1 M Tris buffer with 50 mM ethanolamine (pH=8.5) for 1 h to quench the excessive NHS groups left after immobilization. NHS groups are active for further possible reactions. Then, the chips were washed with DI water for 2 min.

The spotted chips were kept in a desiccator under vacuum until further use.

5.4.1.5 Assay procedure

miRNA target samples were polyadenylated (approximately 15–20 Adenine residues) by using PolyA polymerase in order to have polyA tails in their 5'-end. Through polyA end, after capturing miRNA targets on the microarray surface with complementary surface probes, polyT-conjugated GNRs were used for labeling.

After blocking, washing and drying, all the chips were preincubated with the stabilizer sequence in order to extend the capture region a bit far from the surface. 1 μM of stabilizer oligo was prepared in 2xSSC buffer, dropped on the chips and the chips were incubated for 20 min with the stabilizer. After incubation, the chips were washed with 2xSSC for 2 min and 0.2xSSC for 2 min, and dried.

miRNA detection was done in either of the assay formats: heterogeneous or homogeneous. In heterogeneous assay format, the microarray chip was first incubated with the miRNA sample for 5h and then placed in the microfluidic chamber and incubated with GNR-polyT conjugate for another 5h at room temperature. After rinsing with the buffer for 10 min, endpoint images were taken. Particle counting was done using SPANDEX custom software. Both heterogeneous and homogeneous assays were done in liquid in microfluidics. In heterogeneous experiments, endpoint measurements were taken at the end of experiments, whereas in homogeneous experiments, real-time video of sample incubation was taken while the chip was incubating with the homogeneous sample. In homogeneous assay, first, miRNA samples and GNR-polyT conjugate were mixed in a vial before incubation. Then, the mixture was injected into the microfluidic chamber and a real-

time video of the surface was captured during 1h incubation at a flow rate of 5 µL/min. The video was used for the analysis of dynamic tracking of labeled-miRNA conjugates' individual binding.

5.4.2 Results and discussion

5.4.2.1 Optimization of assay conditions

First of all, for a proper surface chemistry and efficient ssDNA surface probe immobilization, the polymer used for microarray surface modification was selected. MCP-2, MCP-2F and MCP-2 with 5% MCP-2F were used to immobilize miR-451 surface probe. The DNA surface probes were spotted on the different polymer coated chips at 12.5 µM, 25 µM, 37.5 µM and 50 µM concentrations. Surface morphology and probe densities were compared. All three polymers provided homogeneously spotted DNA spots with good spot morphology. The probe height and density were analyzed using IRIS. Figure 5.2A shows probe densities as a function of the immobilization concentrations of DNA probes on three different polymers. MCP-2F holds the smallest spots with a diameter of 65 µm due to its hydrophobicity while resulting in reduced amount of probe immobilization. On the other hand, MCP-2 polymer provides the largest spots with an average diameter of 130 µm. Since MCP-2 and MCP-2 with 5% mCP-2F polymers have similar immobilization efficiency, and we prefer to fit as many spots as possible in a FOV for multiplexing experiments, we selected MCP-2 with 5% MCP-2F copolymer for the rest of the experiments. It provided around 90 µm spot size.

As discussed in Chapter 3, DNA probe density is also crucial for a proper hybridization. The negative charge from neighboring DNA strands can hinder

hybridization efficiency. Hence, high probe density may not necessarily provide higher binding signal in hybridization assays. To observe the effect of probe density, four arrays were spotted with 20 µM and 40 µM concentrations of the surface probe for miR-451. The arrays were incubated with four concentrations of synthetic miR-451 target and labeled with GNR-PolyTs as described in Section 5.4.1.5. After incubation, the chips were washed and imaged with SP-IRIS. Figure 5.2B depicts that binding of miR target versus probe density. Both 20 and 40 µM surface probes provided almost identical binding results. This result suggests that the surface reaches to a saturation with 20 µM probe density which does not result in higher binding efficiency even if the probe density is increased. Therefore, for the rest of the experiments 20 µM was chosen as the optimum surface probe density in array preparations.

In heterogeneous experiments, it was observed that, the longer the incubation time for miRNA samples was, the more the nanoparticles were captured. Incubation times 2h, 3h, 4h and 5h were tested for both sample and GNR incubation. The best results were obtained with 5h+5h incubation, hence, it was selected as the optimum incubation times.

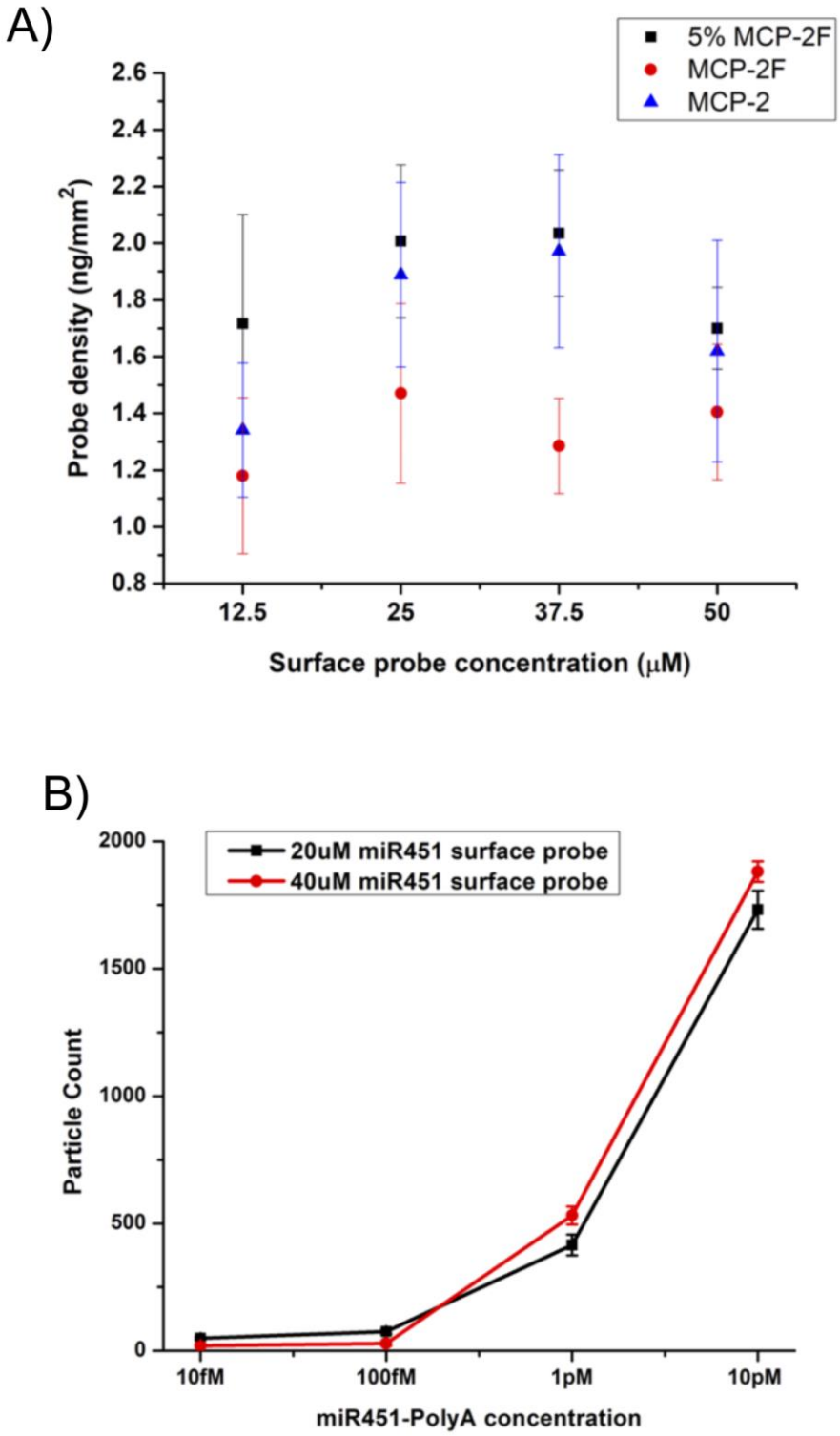

Figure 5.2 A) Probe densities on three different polymers. B) Effect of surface probe density in capture efficiency.

5.4.2.2 Heterogeneous SP-IRIS microRNA assay

Polyadenylated miRNA samples (synthetic RNA mimics of miR-451 and miR-223) were used with a polyA tail. SP-IRIS chips were spotted with ssDNA surface probes which were designed to have a complementary region to the corresponding miRNA. Heterogeneous microRNA assay consists of two steps. In a petri dish, the chips were incubated with miR-451 and miR-223 samples separately. Then, chips were placed the microfluidic cartridge and polyT-conjugated GNRs were injected into the cartridge using a syringe pump to label the captured miRNAs on the chip surface. Endpoint images were taken and analyzed using SPANDEX to obtain total particle counts. Individual particles bound to target miRNAs were identified and digitally counted. Figure 5.3 shows the flow of SP-IRIS miRNA assay schematically and Figure 5.4 shows heterogeneous assay scheme.

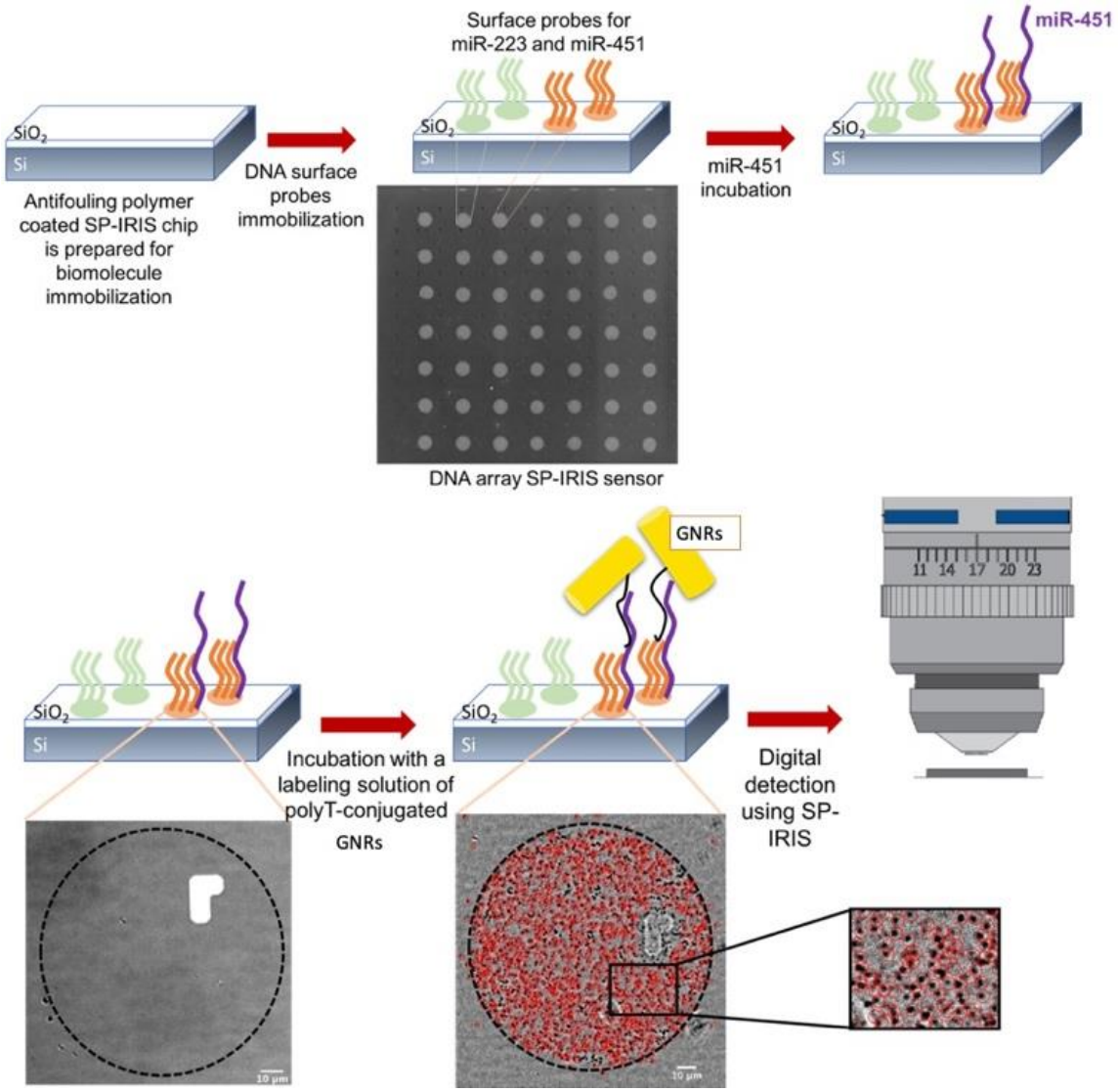

Figure 5.3 A) Schematic representations of assay procedure for miR451-polyA capture and detection using SP-IRIS.

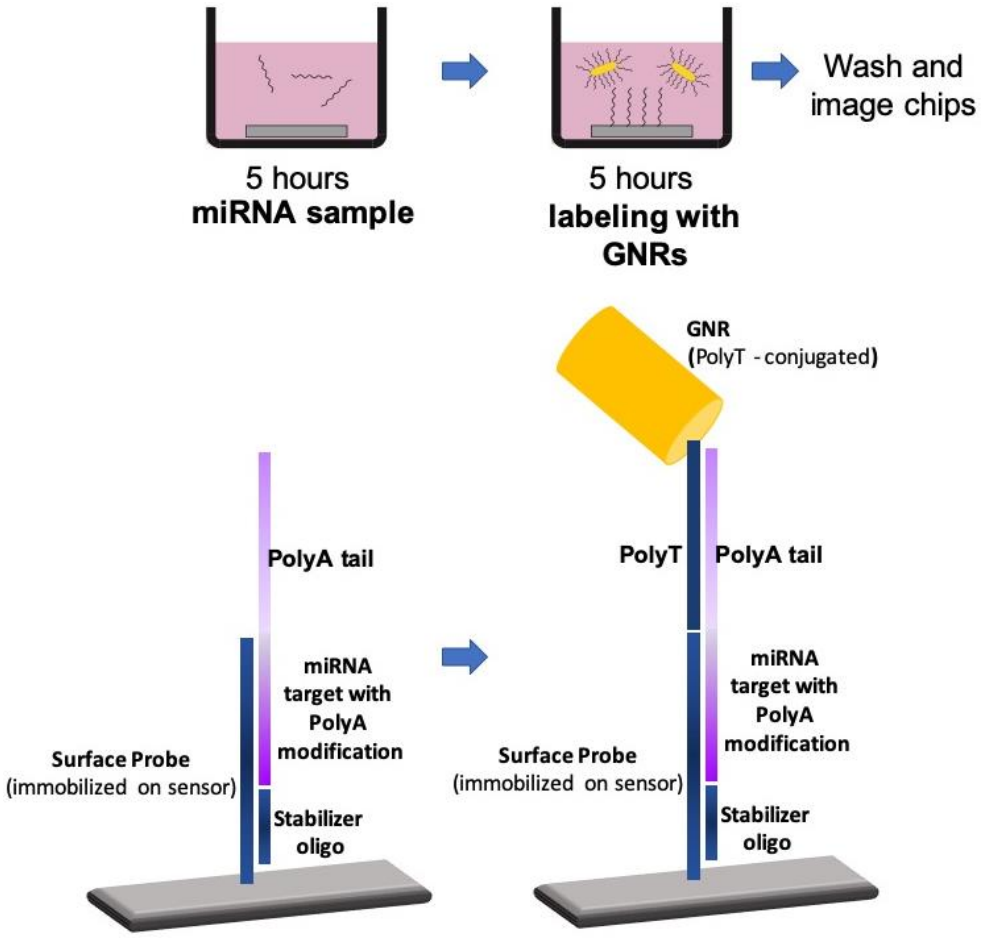

Figure 5.4 Heterogeneous assay scheme. The chip is first incubated with the sample solution, then washed, then incubated with a solution of GNRs.

In Figure 5.5, the average nanoparticle counts (for n=16 replicate spots on one chip) are plotted against miRNA concentration for two miRNAs after incubation with A and C) miR-223 and B and D) miR-451 for 5h following with 5h GNR label incubation in heterogeneous sandwich assay regime. The double logarithmic response plots (Figure 5.5 C and D) show linear correlations with R^2=0.91 and 0.94 (and equations y=0.64865x+1.04008 and y=0.35328x+1.49187) for miR-223 microarray and miR-451 microarray, respectively between the particle counts and target concentration. Linear

ranges were 1fM-1pM and 100 aM-1pM for miR-223 and miR-451, respectively. The limit of detection values were calculated as mentioned in Chapter 4 Section 4.5.4. For miR-223, LOD was 2.22 fM and for miR-451 LOD was 228 aM. LOD values are very promising, however, the results of heterogeneous experiments need to be improved in terms of linearity and specificity. Homogenous assay method was experimented to improve quantification.

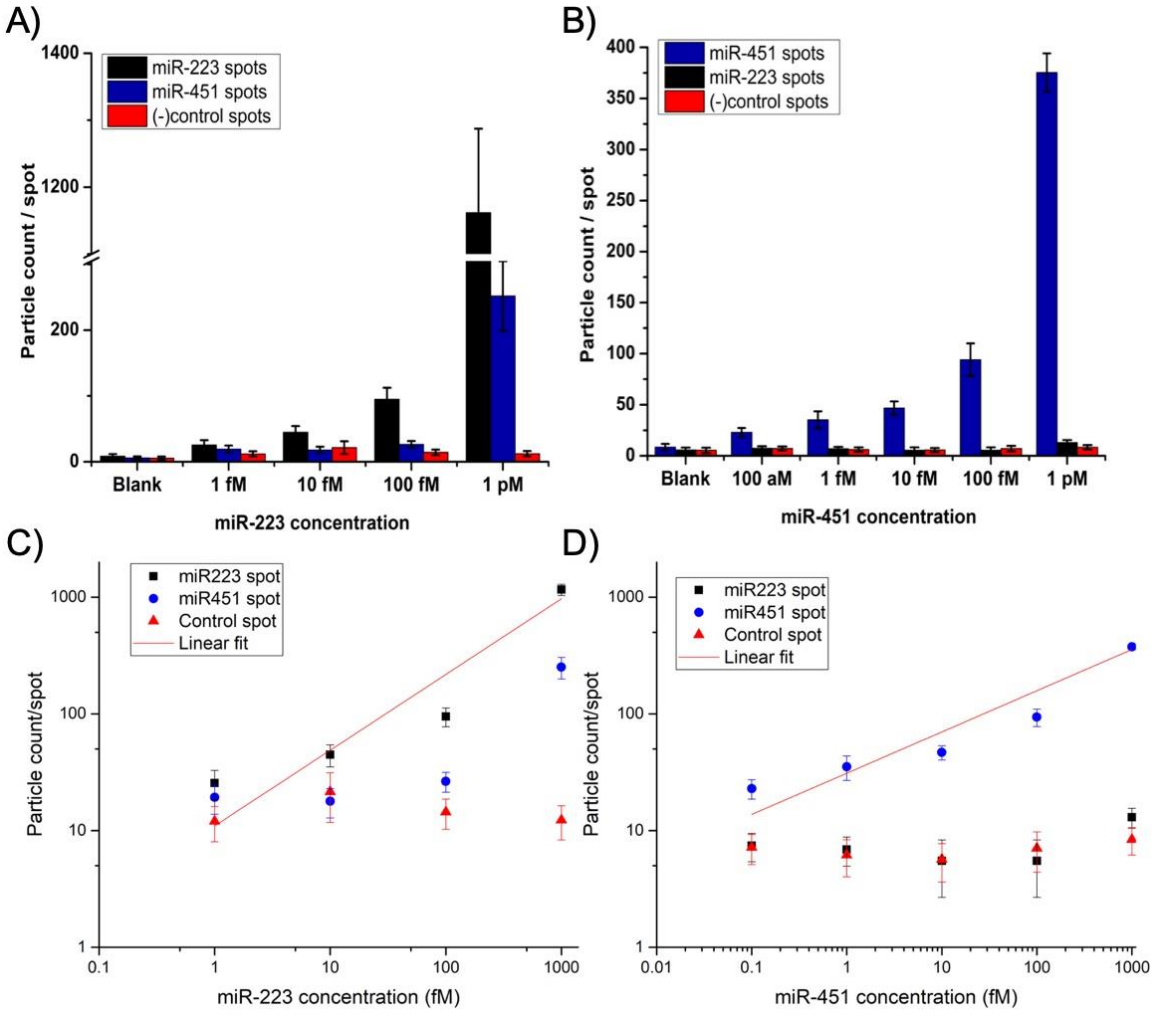

Figure 5.5 Dilution curves for A) miR-223 and B) miR-451 (for n=16 replicate spots on one chip) after incubations in heterogeneous assay scheme. Double logarithmic response plots for C) miR-223 and D) miR-451samples.

5.4.2.1 Homogeneous assay and dynamic tracking

Figure 5.6 shows homogeneous assay configuration on SP-IRIS. Homogeneous assay configuration has a one-step protocol. miRNA sample was pre-mixed with polyT-conjugated GNRs in a vial for 30 min at room temperature. Microarray chip was then incubated with the pre-mixed solution.

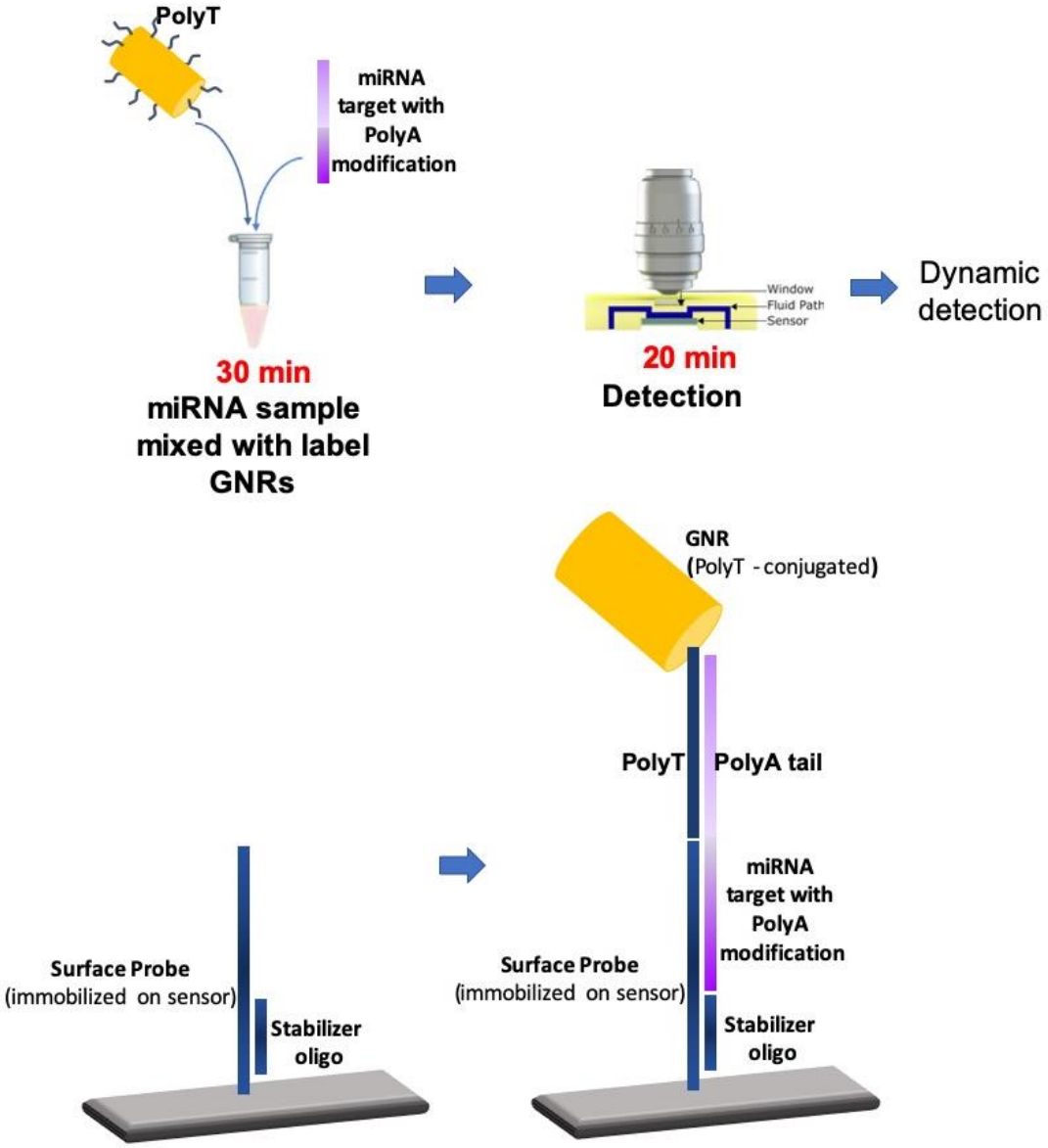

Figure 5.6 Schematic representation of homogeneous assay configuration on SP-IRIS.

It is well known in the literature that in-solution binding (homogeneous assay) is a lot faster than binding on a solid phase support (heterogeneous assay). Our experiments also confirm this and we observed a much rapid response in our real-time homogeneous assays. Incubation time was kept under 60 min. The registered counting results in Figure 5.7 show cumulative (total) binding of the miR-GNR complex onto the different spots in the same field of view versus time. 100 aM-1 pM range miRNA samples were tested in homogeneous assays. Generally, no significant binding on the non-complementary control spots was observed. However, miR-223 has more cross reactivity towards miR-451 spots which was also a specificity issue in heterogeneous assay. Binding rates measured with dynamic tracking are shown for one example spot from each experiment Standard curves were measured with a range of analyte concentrations between 100 aM and 1 pM. Since we are able to detect and count every single binding event on the relevant spot throughout the experiment, we can track binding and debinding of particles. Here we represent total binding which means that even if a miRNA-GNR complex binds to its complementary surface probe and debinds at equilibrium, we can still include this complex for detection and quantification. We simply cannot implement this in endpoint assays. Therefore, we focus on total binding event count rather than particle counts on the surface of the sensor in a time snapshot. Figure 5.8 was produced using binding rates on the relevant microarrays as a function of target concentration in the sample solution. LODs were calculated based on 3.3σ/slope (σ = standard deviation of blank, n = 3). As seen in Figure 5.8B, dilution curves yield better linear fits and much lower LODs as 12.6 aM for miR-451 and 104 aM for miR-223. Hence, we obtained 20-fold improvement in sensitivity of our microarray

with dynamic tracking and assay duration was dropped from 10 h to 1 h.

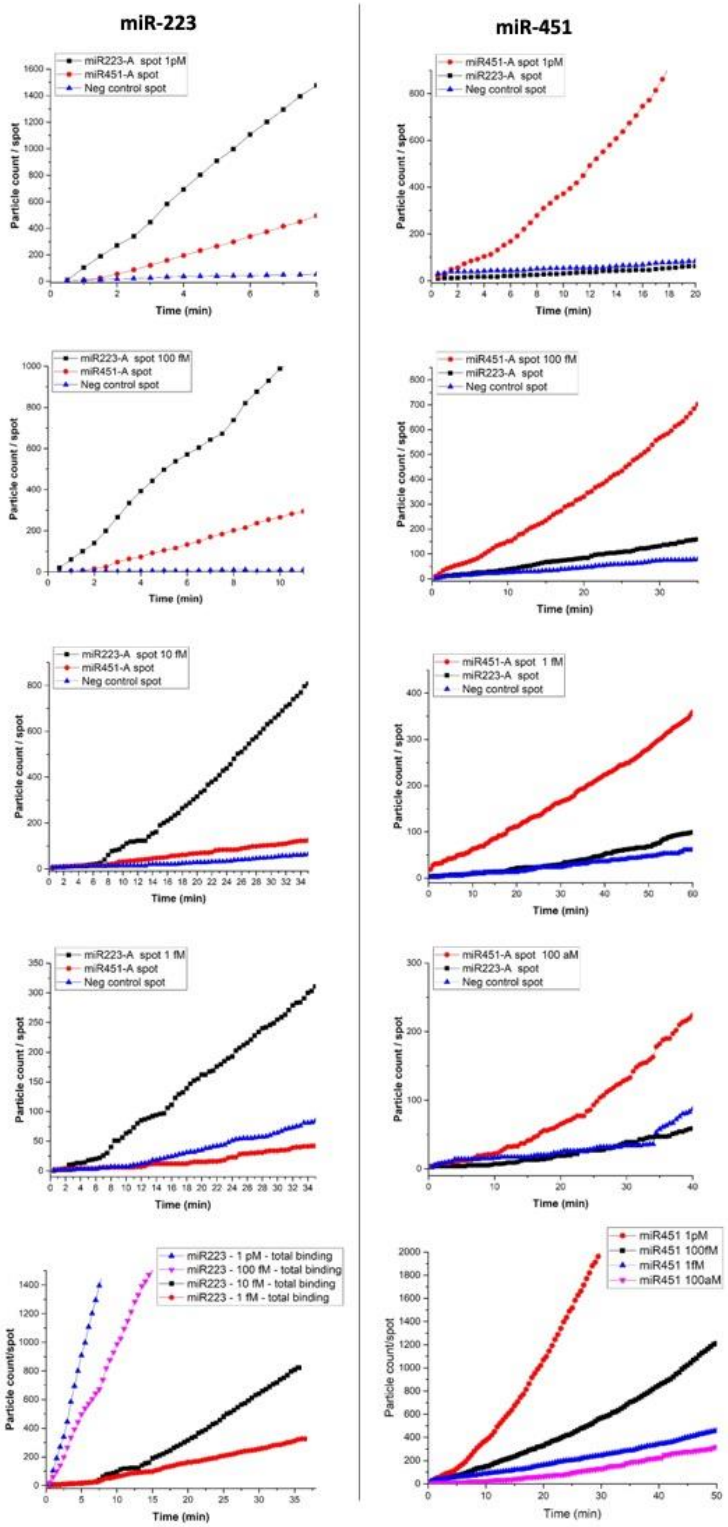

Figure 5.7 Dynamic tracking for real-time homogeneous in-liquid miR-451 and miR-223 experiments. Dynamic tracking measures the cumulative number of binding events. Top to bottom, each figure shows the cumulative binding for miRNA sample mentioned in the legend. Final bottom two figures are the comparison of binding rates for 4 different concentrations of miR-223 (left) and miR-452 (right) in homogeneous assays.

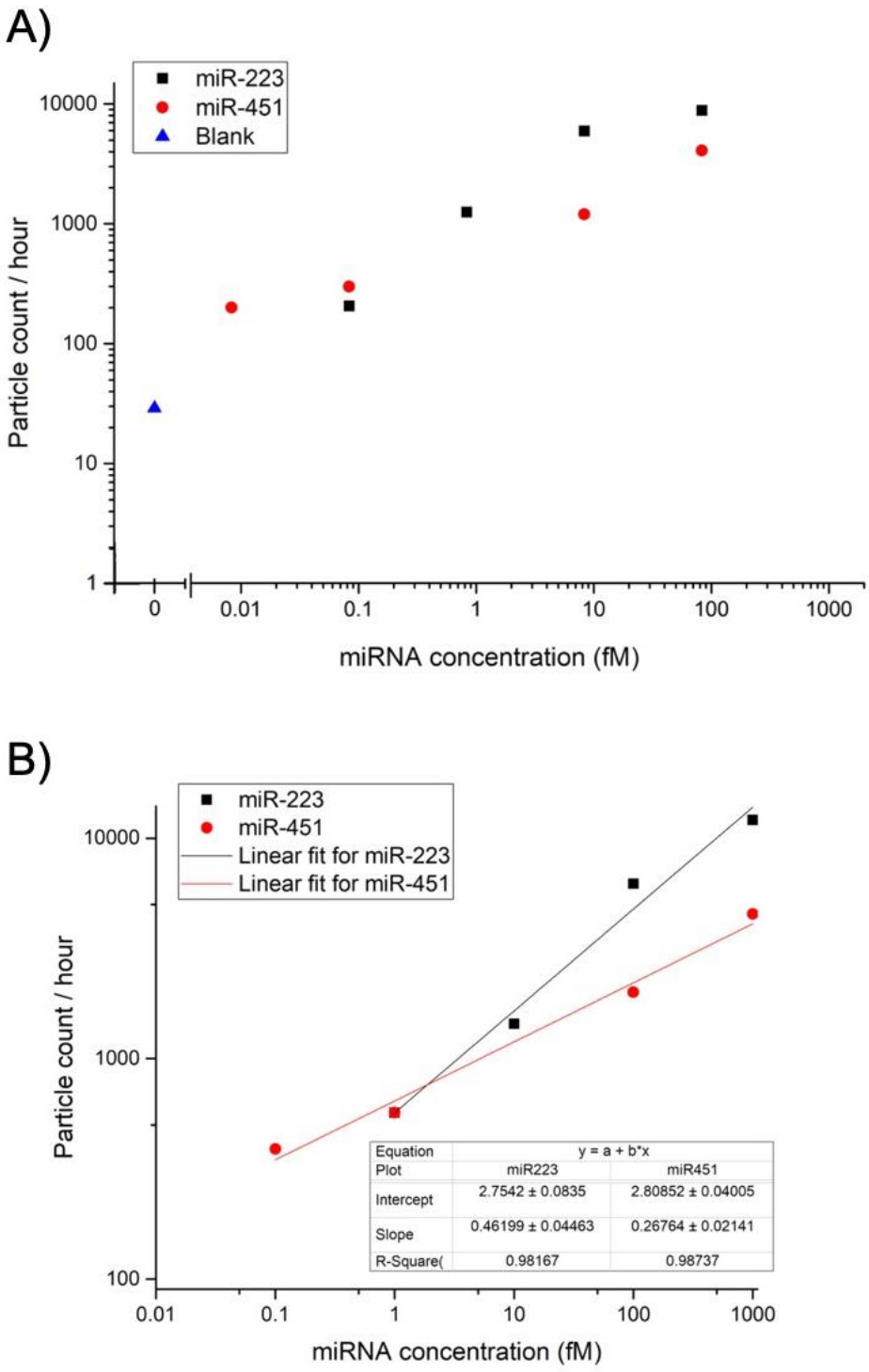

Figure 5.8 A) Binding rates for different concentrations of miR-451 or miR-223. B) Linear fits.

5.4.2.2 Multiplexed detection

In order to test multiplexing capability of SP-IRIS miRNA microarray, two of the miRNAs were mixed together prior to the experiment. 10 fM miR-223 sample and 100 fM miR-451 sample were mixed with GNRs separately and then they were mixed together. The same protocol was followed for the rest of the experiments. The two spots dedicated to miR-451 and miR-223 detection were imaged in the same FOV, just as the previous experiments. we observed excellent binding on the two spots simultaneously. Figure 5.9A shows the tracking results of this experiment. Binding rates of multiplexed and singlexed experiments were compared in Figure 5.9B for the first 30 min. as we can see, miR223 showed almost identical binding rate with 23 min^{-1} compared to the singlexed one which was 24 min^{-1} for 10 fM sample capture. However, we see a decrease in the binding rate and total number of captured target in miR-451 100 fM sample. Its binding rate dropped from 33 min^{-1} to 17 min^{-1}. Since we know from the singlexed experiments that miR-451 has a cross reactivity towards miR-223 surface probes, we may consider specificity issues as the source of this loss.

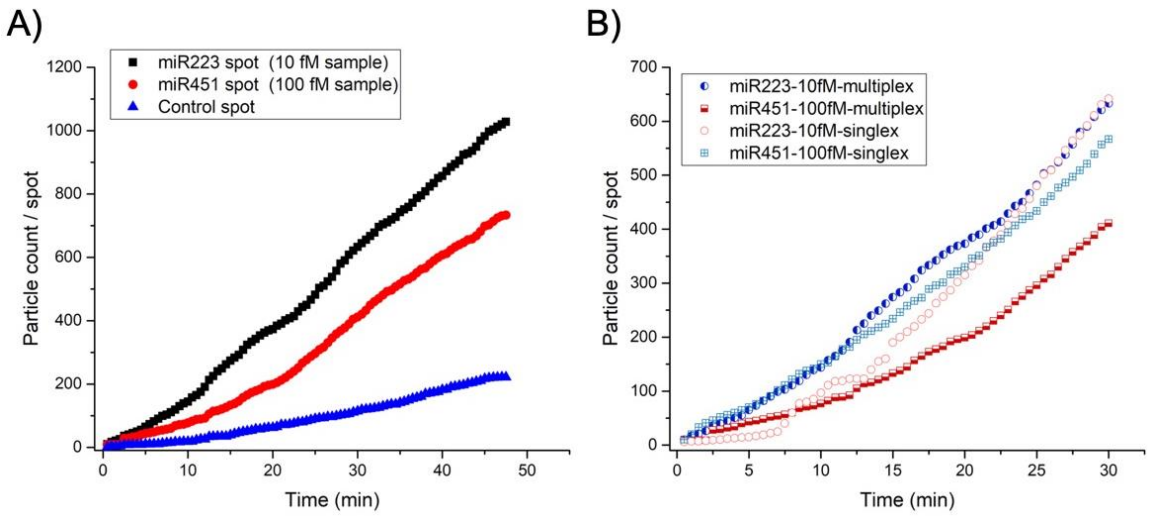

Figure 5.9 Binding curves showing total binding of miRNAs using dynamic tracking for multiplex SP-IRIS for the target mixture of miR-223 (10 fM) and miR-451 (100 fM).

5.4.3 Conclusion and future directions

We developed a miRNA microarray for miR-223 and miR-451 detection and quantification. In this project, we show that the sensitivity has been improved by dynamic tracking, however, it can be further improved by eliminating non-specific binding on control spots and in blank experiments. In order to achieve this, surface probes can be redesigned to minimize cross-reactivity. Such a design of surface probes would contribute to the increased sensitivity. Moreover, the detection and tracking software can be revised to eliminate possible false positives.

In addition to the findings in this project, the next steps to be completed are as follows. First, we aim to complete multiplexing with better surface probes and prepare dilution curves for mixtures. Secondly, we aim to perform experiments in serum or cell media to test the effect of media. Lastly, we will focus on testing real samples like patient samples and then compare the results with gold standard techniques.

5.5 Digital single-molecule counting assay for rare mutation detection

Each human cell possesses *KRAS* gene which has a crucial role in regulating intercellular signaling pathways [191]. These pathways are responsible for major processes in a cell, such as proliferation, differentiation and survival. When *KRAS* gene gets a mutation, it will interfere with all these major pathways, hence, the cell may multiply out of control, which may cause cancer eventually. Figure 5.10 shows the effect of a mutation in *KRAS* gene. Mutant *KRAS* prevents the binding of miRNA-let-7 to the gene, which causes a change in the protein production and abnormal cell growth hereafter.

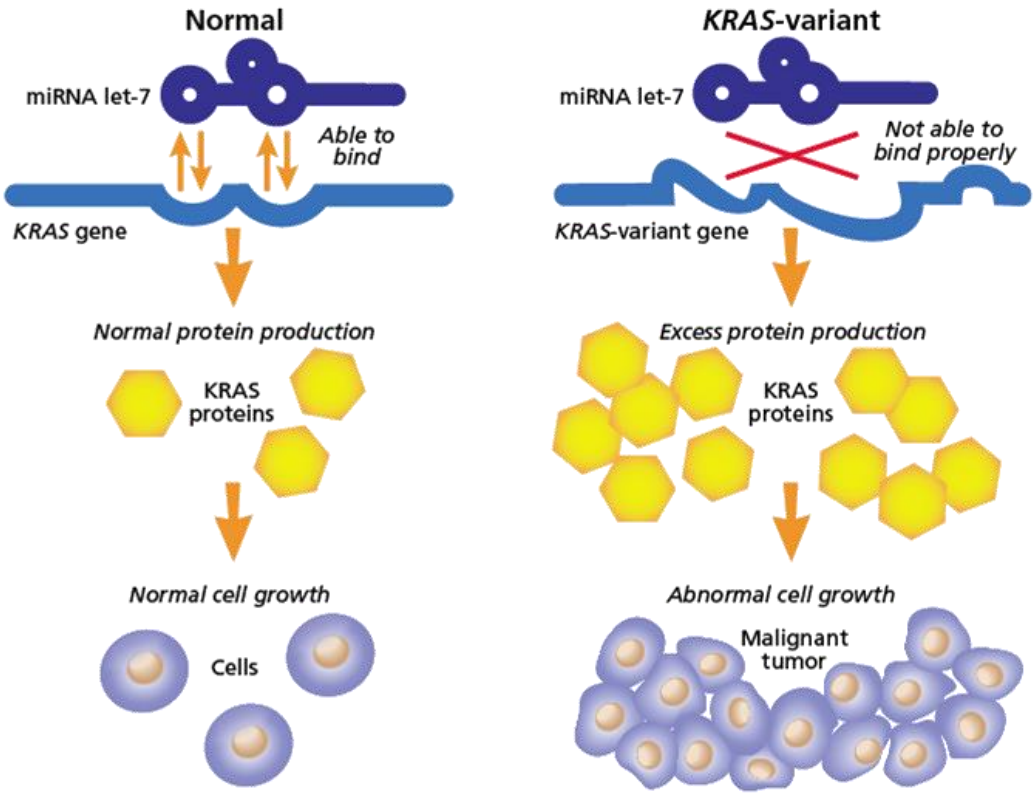

Figure 5.10 Schematic showing how *KRAS* works (left) and how pathways change if a mutation occurs in a *KRAS* gene.

KRAS mutations are one of the most common causes of cancer and *KRAS* is the most frequent mutant oncogene. The ability to identify DNA variants in oncogenes leads to early diagnosis. Additionally, knowing the mutation status before or during the treatment of cancers is essential since not every therapy works in every type of mutations.

Colorectal cancer (CRC) is the third most common cancer among men and the second most common cancer among women [192–194]. More than 1 million patients are diagnosed annually, of which 50% develops metastatic disease [192,195]. CRCs can be classified based on the presence of mutations in oncogenes such as *KRAS*. *KRAS* mutations are present in 35–40% of CRC cases, and the presence of the mutation plays an important role as both a diagnostic and a prognostic biomarker for CRC survival [193,194,196]. Sensitive and specific detection of low-abundant mutant genes is crucial for diagnosis and treatment.

Sequencing, PCR, and high-resolution melting (HRM) are used in *KRAS* mutation detection. The former requires 30% mutant cell presence while the latter requires complex thermo-cycling instrumentation, and the last has a sensitivity only 5–6% of the mutant cells in the clinical samples [197–200]. Thus far, mutation testing, gold standard methods employed in detecting clinical samples leads to complex, expensive and time-consuming analyses. Hence, the methodological aspects and types of assays are important, and a good balance between accuracy and practicality of the testing method is desired.

Currently, tumor tissue is the gold standard for sample collection for sequencing or molecular testing for diagnosis [201,202]. Sample obtained from biopsies may not always contain enough of tumor content available for testing or the tissue may be in insufficient

amount [203]. Also, biopsies are not free of clinical complications.

Cell-free circulating tumor DNAs (ctDNA) are DNA fragments present in blood or other body fluids which are released from the tumor cells [204]. The term liquid biopsy comes into play with ctDNA as blood or plasma samples are used for detection and it is used in diagnosis of cancer, monitoring mutations during treatments, and provides a less invasive technique for the detection of cancer biomarkers [205].

ctDNA is only a very small portion of cell-free circulating DNA. It is very challenging to detect ctDNA derived from the tumors in the pool of cell-free DNA. The low number of mutant copies from the cancer origin are covered with the huge amount of wild-type DNA. Therefore, the detection and analysis of ctDNA with ultra-low copy number require isolation and amplification either on the mutant genes (PCR-based sequencing) [206] or in multiple genes simultaneously (next-generation sequencing (NGS)) [207]. Droplet digital PCR (ddPCR) is one of newly developed methods which can detect mutant alleles with ultra-high sensitivity (0.01–0.001%) [206]. However, these tests are very time consuming and very expensive. Figure 5.11 depicts the fraction of mutant *KRAS* in plasma cell-free DNA in UICC (Union for International Cancer Control)-stages IA to IV in pancreatic cancer patients' plasma samples [201]. The data was obtained using a qPCR-based method and shows that in pancreatic cancer, the patients' plasma samples contains very small amount of mutant DNA fractions until the cancer develops into further stages. However, for early detection, the detection technique should be sensitive enough to detect very low abundant mutant DNA.

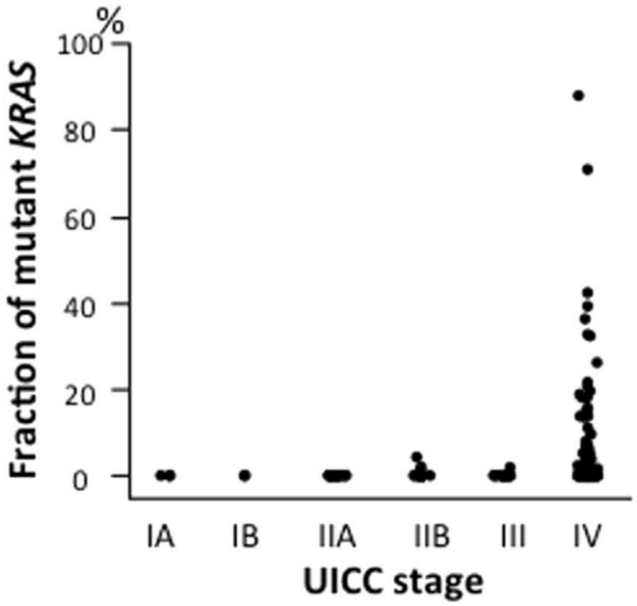

Figure 5.11 The fraction of mutant *KRAS* in plasma cell-free DNA in UICC-stages (Union for International Cancer Control) IA to IV in pancreatic cancer patients' plasma samples. Adapted from [201].

In this study, we introduce our SP-IRIS digital microarray as a promising approach for simultaneous detection of single mutations in different oncogenes in a sensitive and multiplexed assay format. In the market, there are two commercialized array platforms, Affymetrix and Illumina, for SNP genotyping [206] but they are not applied in liquid biopsies. Damin et. al have shown the first microarray for mutation detection in liquid biopsy samples meeting the sensitivity and specificity requirements for the first time [208]. The fluorescence microarray shows LODs ranging 0.03–0.28% for seven most common mutations of *KRAS* gene [208]. Here, we collaborate with Damin and colleagues to develop SP-IRIS microarray for *KRAS* mutation detection in order to overcome the challenges mentioned in the previous sections that fluorescence microarrays face and possible further improve the sensitivity and multiplexing ability of the mutation detection assays.

5.5.1 Experimental section

5.5.1.1 Samples

In this work, we were provided with samples by Dr. Chiari's group at Istituto di Chimica del Riconoscimento Molecolare, CNR, Milano, Italy. The plasma samples containing ctDNA with mutant *KRAS* gene were obtained from CRC patients. The extraction and amplification of ctDNA to make them ready for detection experiments were explained in detail by Damin et al. [202,208]. Simply, ctDNA were extracted from the samples. The DNA sequences containing the mutations were amplified. Calibration experiments were done using standard commercial samples which were known to have 50% mutated alleles in them. Different concentrations of mutant alleles were prepared in the range of 0.01%–1%. The final samples had wild-type allele (WT) in high abundancy whereas the mutant allele was in very low abundancy (MT). ssDNA from PCR products were prepared with streptavidin magnetic beads and liquid allele-specific hybridization was achieved using the complementary reporter sequences. The preparation for hybridization and labeling was explained in detail by Damin et al. [208]. For the detection of wild-type and *KRAS* mutations, the reporters for the wild-type and the mutated sequences were added together in equimolar amounts (final concentration 0.1 μM) to the tube containing the ssPCR product solution (final volume 40 μL). At this stage, the samples were shipped frozen to us for our tests using SP-IRIS digital microarray. Figure 5.12 shows the components of the final product containing ssPCR product (derived from patient sample) which can be WT or MT DNA, reporter oligo including a Barcode region complementary to the surface probe, UTag attachment to the PCR product at the end of the

primer sequence (to be used for labeling). Note that Reporter sequence is product specific.

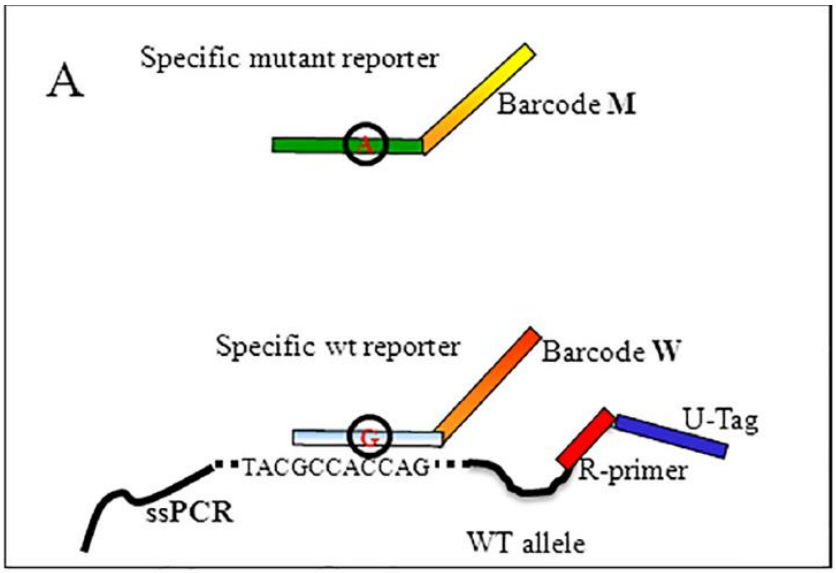

Figure 5.12 Schematic representation of the PCR products prepared from ctDNA of patient samples. Reporter sequence is used for hybridization with the ssPCR product which contains a region complementary (Barcode) to its surface probe for capturing on the microarray surface. In the case of *KRAS* wild-type allele here, the specific wild-type reporter hybridizes in solution with the ssPCR product (ssPCR), whereas the specific mutant reporter (with the variant position circled and in red) does not. Adapted from [208].

5.5.1.2 Reagents and apparatus

Dithiothreitol (DTT) was obtained from Sigma-Aldrich (Woodlands, TX, USA). NAP-10 columns for DNA purification were purchased GE Healthcare. Citrate-capped nanorods (OD1) with a longitudinal surface plasmon resonance peak at 650 nm and nominal dimensions 25 nm by 71 nm were used (Nanopartz Inc, Loveland, CO, part number A12- 25-650-CIT). MCP-4 copolymer was purchased from Lucidant Polymers (Sunnyvale, CA, USA) and used for chip surface functionalization. All other chemicals were purchased from Sigma-Aldrich.

NanoDrop 2000c Spectrophotometer from Thermo Fisher Scientific (Waltham, MA) was used for characterization of nanoparticles. Scienion S3 SciFlexArrayer (Berlin, Germany) spotter was used to create an array of antibody surface probes. Hamilton PHD 2000 syringe pump was used in liquid experiments.

5.5.1.3 GNR- UTag conjugation

GNR-UTag conjugates were prepared as explained in Section 5.4.1.3. Briefly, they were prepared with slight modifications to previously described methods [189,190]. Prior to conjugation, thiol-modified UTag oligonucleotides were treated with DTT to cleave the disulfide bonds and to activate thiols. 20 µM thiol-polyT was prepared in 170 mM phosphate buffer pH 8.0 and mixed with 100 mM DTT. The solution was kept in dark at room temperature for 3 hours occasionally vortexing. PolyT oligos were then desalted and purified using NAP-5 column according to the manufacturer's directions. Meanwhile, 6 mL of nanorods (OD1, approximately 10 pM) were centrifuged at 1500 rcf for 15 min and resuspended with DI water in a glass container. Immediately after obtaining UTag from the column, the purified oligonucleotides were quantified by measuring their absorbance at 260 nm using a NanoDrop spectrophotometer.

GNRs and oligos were mixed in the container and placed on an orbital shaker for 30 min. Then, to bring the pH of the solution to pH 3, concentrated citrate buffer was added up to a final concentration of 10 mM citrate. Same way, tween-20 was added to have a final concentration of 0.1% w/v. After vortexing and sonicating, the solution was rested on the orbital shaker overnight. In the next 24 h, the salt concentration of the solution was brought up to 150 mM by slowly adding citrate buffer with high concentration of NaCl.

Salt addition was followed with another overnight resting. Finally, the nanorods were washed three times with PBS with 0.1% tween-20 to remove the excess, unbound oligos. The conjugation was confirmed by spectrophotometric analysis. The GNR-UTag conjugate was kept in PBST solution in a dark place for up to 2 months at room temperature for further use. Before every use, the conjugate was washed once again to remove the surfactant.

5.5.1.4 DNA probe design

Table 5.3 shows the sequences corresponding to two *KRAS* mutations, custom-designed ssDNA surface capture probes, reporter sequences for labeling. Probes were purchased from Integrated DNA Technologies (IDT) (Coralville, IA). Surface probes were amine-functionalized and "AmMC6" indicates amine functionalization for covalent binding to the polymer-coated IRIS chip, while GNR label sequence was thiol-modified and "ThioMC6" indicates thiol functionalization for nanorod conjugation, as provided by IDT.

Name	Sequence
SP for Wild-type (WT)	5'- /5AmMC6/ actccagtgccaagtacgat-3'
Reporter for WT	5'-*CTGGTGGCGTA-†atcgtacttggcactggagt-3'
SP for G12C	5'- /5AmMC6/ taatcttaattctggtcgcgg-3'
Reporter for G12C	5'-* CT**T**GTGGCGTAG-†ccgcgaccagaattagatta-3'
SP for G12S	5'- /5AmMC6/ attgaccaaactgcggtgcg-3'
Reporter for G12S	/5'-*GCT**A**GTGGCGTA-†cgcaccgcagtttggtcaat-3'
GNR label – UTag	5'-CAGGACCATTCTCTCAATGTTCGGACTCAG /3ThioMC3-D/-3'

Table 5.3 Surface capture probes (SP) for *KRAS* genes with mutations c.34G>T (p.G12C) (abbreviated as G12C) and c.34G>A (p.G12S) (abbreviated as G12S) on Exon 2 Codon12-13, their complementary reporter sequences used in hybridization and labeling. Note that * sequences which hybridize to single strand PCR (the variant base for each mutation is in bold and underlined) and † the tails of the reporter oligonucleotides which hybridize to spotted capture probes [208].

5.5.1.5 Fabrication of SP-IRIS microarrays

IRIS chips were cleaned by sonicating in acetone, rinsed with isopropanol and DI water and dried under nitrogen. They were functionalized with MCP-4 copolymer from Lucidant Polymers. Complementary surface probes for WT and MT sequences, and control surface probe were dissolved in the printing buffer (150 mM sodium phosphate pH 8.5, 0.01% Sucrose monolaurate) at a concentration 10 µM and spotted on coated silicon chips in an array format using Scienion sciFLEXARRAYER S3 piezoelectric robotic arrayer. The periodicity of the spots and the humidity in the spotting chamber (set to 67%) were optimized in order to prevent merging of neighboring spots. A microarray pattern was designed for sixteen replicate spots for each DNA. The space between the spots (pitch) was

set as 200 μm. After spotting, the DNA-spotted chips were kept in the spotter chamber at 67% humidity overnight at room temperature to allow time for the amine-modified ssDNA surface probes to immobilize on the surface. Following the immobilization, the chips were blocked as described in Damin et al. to quench the residual reactive groups left after immobilization [209]. The spotted chips were kept in a desiccator under vacuum until further use.

5.5.2 Preliminary results

5.5.2.1 Development of SP-IRIS rare mutation microarray

Mutation detection was done in homogeneous assay format. In the assay, the allele-specific hybridized samples and GNR-UTag conjugate were mixed in a vial before incubation. Here we do a 100x dilution with the provided sample. Then, the mixture was injected into the microfluidic chamber and a real-time video of the surface was captured during 1h incubation at a flow rate of 5 μL/min. The video was used for the analysis of dynamic tracking of labeled-MT and WT allele conjugates.

Figure 5.13 shows how we hybridize single stranded tagged-PCR products with dual-domain oligonucleotide reporters. The domain sequences complementary to regions encompassing the mutation form hybrids in solution that are direct by the second domain to specific locations on the microarray surface. The tagged-PCRs captured on the microarray are revealed by the GNRs at the end of the universal tag oligonucleotide (UTag).

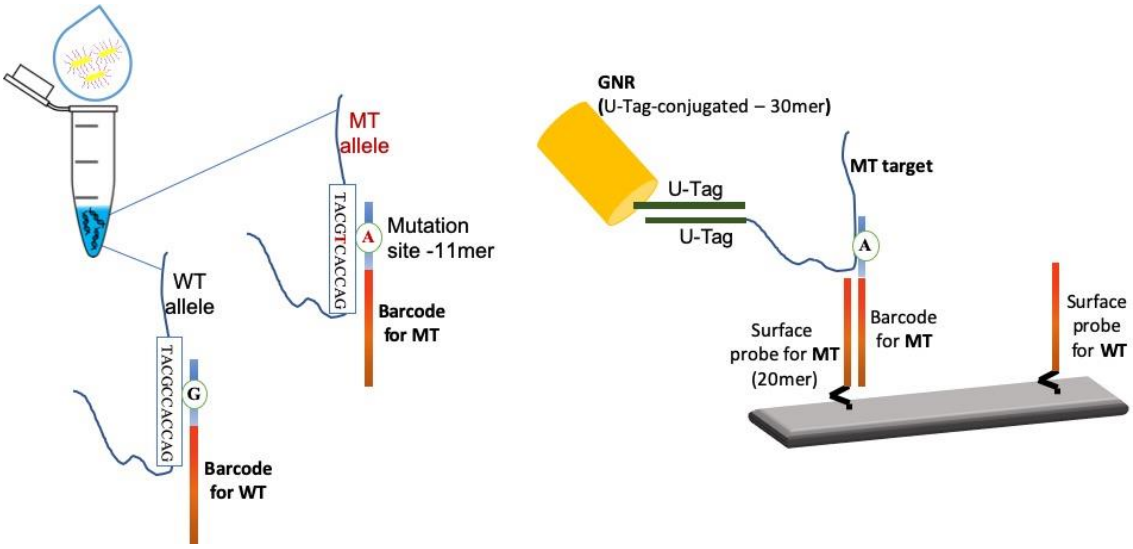

Figure 5.13 Schematic representation of homogeneous assay. WT and MT allele PCR products containing sample was mixed with GNR-UTag conjugates prior to the experiments. microarray surface was decorated with surface probes complementary to WT and MT samples and which have only 1 base pair difference. Alleles were captured on the spots and detected via GNRs using SP-IRIS.

5.5.2.2 Melting experiments

Here, our assay differs what we have done so far in the other digital microarrays in the rest of this dissertation. In this study, we are working with point mutation which means that our sample contains WT sequence in majority while very small amount of MT sequence is present in the sample solution in minority. We want to detect a minority sample with a point mutation. WT and MT sequences possess only one different base. Therefore, cross-reactivity is huge among the samples toward the surface probes. With the help of multiple steps in sample preparation, specific oligonucleotide reporters, and specific surface probes designs, these problems were overcome partially [208]. However, huge amount of WT creates background where WT samples also binds to MT spots on the surface since there is only one different base among them.

An important application of DNA melting — whereby a double helix is destabilized and separates into two single strands above a threshold temperature — is for identifying the presence of a point mutation such as single nucleotide polymorphism (SNP). A SNP is a particular type of DNA mutation in which a single nucleotide is replaced with another. This can occur erroneously during DNA replication and can lead to a variety of diseases including cancer. The 'melting temperature' (T_m) of a solution of double-stranded DNAs is defined as the temperature at which half of the DNA duplexes are double-stranded, and half are single-stranded at equilibrium. Below the melting temperature, the majority of the DNA will form duplexes, and above this temperature most will be single stranded. Mismatched duplexes have a measurably lower melting temperature than perfectly-matched sequences.

The T_m can be manipulated with salt concentration of hybridization solution, which is due to the changes in the screened interactions between the fixed phosphate charges. This technique is highly used in detection of mismatches in DNA sequences. Here, we apply this principle to digital microarrays. Since the sensitivity is very high in SP-IRIS, by changing the salt concentration in flow experiments, we perform a digital melting analysis. To test the efficacy of this system at discriminating DNA mutations in a sample, we spotted two capture probes on the IRIS chip: one that was the reverse complement to the target ('perfect match') for wild-type DNA (WT), and one that had a single base difference ('SNP mismatch') for mutant allele (MT). A 30mer-long oligonucleotide was conjugated to GNRs as a universal tag which is complementary to the UTag used in tagging the target gene as shown in the schematic in Figure 5.13. To test the ability to discriminate mutant and wild-

type allele, a DNA solution containing mutant *KRAS* (1% of total DNA content in the solution) and WT allele was used. UTag-GNRs were used to label both WT and MT alleles in homogeneous assay format. After hybridization of GNRs with the targets at room temperature for 15 min, we introduced this mixture to the chip in flow cell. 1M NaCl and 0.1 % tween-20 containing 5mM Tris buffer was used as the assay buffer. The salt concentration was gradually decreased until the nanoparticles debound. During data acquisition, spots for both MT and WT DNAs were imaged in one filed-of-view. Even though the mutation domain with 11-mer consists of 1-mer mutation point, due to the similarity in remaining 10mer in MT and WT targets, both targets bind to both spots. However, because of the mutation, the mismatched sequences are not strong enough to resist ionic strength changes in the medium. U-Tag and surface probes are long enough to resist these changes. Theoretical Tm in solution are shown in Table 5.3. the only melting site can be mutation site. Theoretical calculations duplexes in solution show that when the salt concentration decreases from 50 mM to 20 mM, Tm for WT allele on WT spot decreases from 40ºC to 34ºC, whereas Tm for MT on the same WT spot (hybridized with 1-mer mismatch) drops from 28ºC to 21ºC. Therefore, in equilibrium at room temperature at this salt concentration, the probability of dehybridization of MT allele from WT spot probes becomes very high, which is shown in Figure 5.14B. Moreover, due to higher number of WT DNA in the sample (99%) and mismatch on MT spot, we observe a drastic debind on MT spot with the salt concentration drop in assay buffer. Using particle tracking, the disassociation kinetics of GNRs were measured. We can fit dehybridization curve to standard exponential decay model to quantitatively measure the off rate; hence, we can

evaluate the amount of perfect match and mismatch ratio in the samples. Tables in Figure 5.15 show the theoretical Tm values for each hybrid on the microarray surface. these values are for free duplex separation in solution. Tm values changes when one of the components is covalently bound to the surface. however, these give us a rough idea that given all the conditions, when we change the salt concentration of the assay buffer, it is very likely that it will separate from only the mutation site.

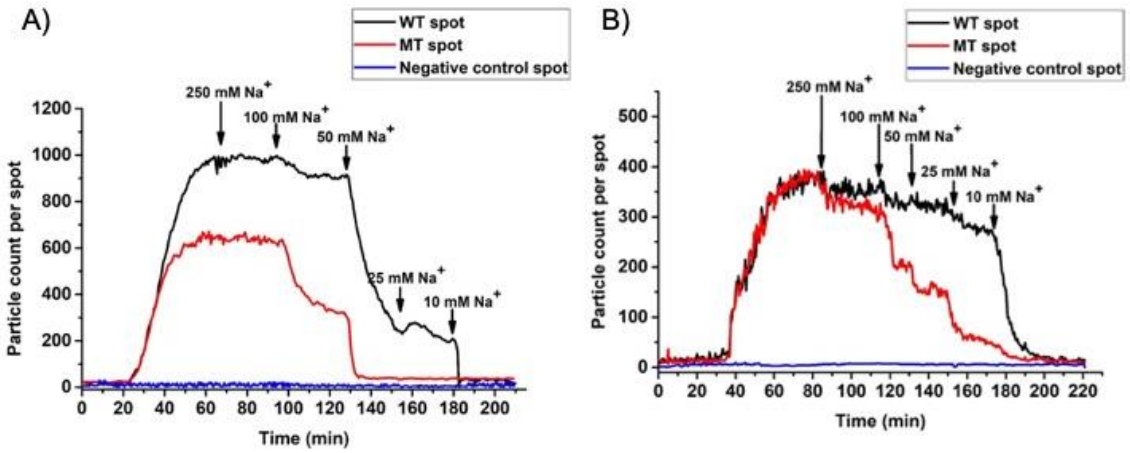

Figure 5.14 A) WT sample and B) 1% MT G12S allele containing standard solutions. Samples were mixed with GNR-UTag and run in the microfluidic chamber. Dynamic tracking is used to track particle-sample binding. After binding reaches to almost a saturation on the surface salt concentration in the buffer was changed and debinding tracked.

Mutation domain - 11mer

WT spot	Tm in 50 mM Na+	20 mM Na+
Perfect match WT	40 C	34 C
Mismatch MT	28 C	21 C

MT spot	Tm in 50 mM Na+	20 mM Na+
Perfect match MT	40 C	29 C
Mismatch WT	22.5 C	16 C

Surface probe domain - 20mer

	Tm in 50 mM Na+	20 mM Na+	10 mM Na+
WT spot	56 C	47.9 C	41.1 C

	Tm in 50 mM Na+	20 mM Na+	10 mM Na+
MT spot	59.1 C	51 C	44.1 C

Figure 5.15 Theoretical Tm values for given sequences at given salt concentrations for free DNA duplexes. Data is provided from IDT webpage via OligoAnalyzer tool.

1% MT (G12C or G12S) and WT containing samples in 250 mM NaCl were tested and endpoint measurements were done in 60 min incubation. Figure 5.16 shows the results of particle counting. After obtaining results for a range of MT content, a dilution curve can be prepared for each type of mutation.

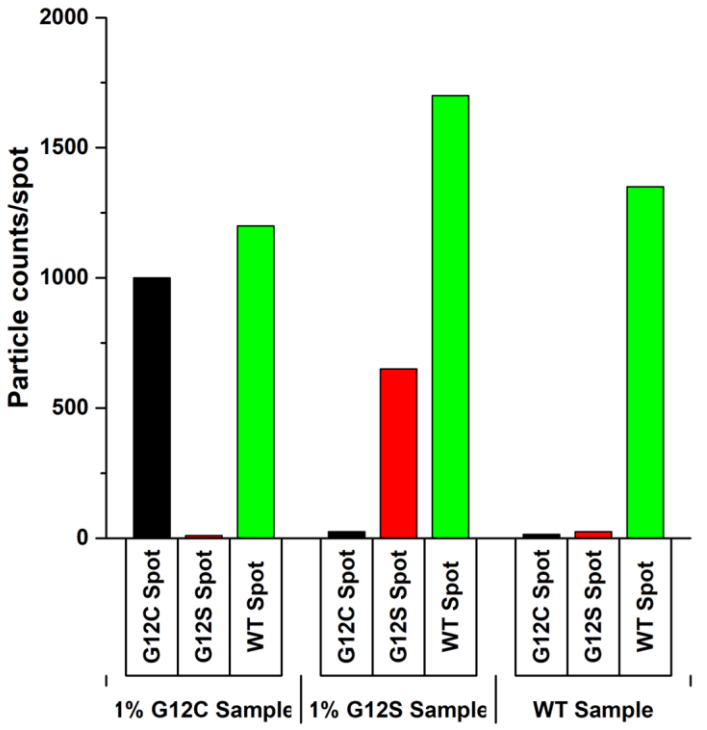

Figure 5.16 Particle counts for samples with 1% G12C MT, 1% G12S MT and WT only, in 60 min incubation.

5.5.3 Conclusion and future directions

We aim to continue studying on the binding kinetics and thermodynamics of DNA-conjugated nanoparticles in *KRAS* mutation detection. Using the system developed here, a thorough investigation of the dilution curve for two types of mutations will be conducted. Melting curves for perfect-matched and mismatched duplexes will be measured while

varying salt concentration with the objective of maximizing the difference in the melting temperature between the two. Off-rates during debinding assays will be determined and evaluated to obtain the appropriate salt concentration of discrimination between WT and MT. Finally, we will investigate the prospect of using this platform to identify rare mutations in clinical samples, using the optimal conditions identified during testing. Our aim is to detect mutant DNA with 1:1000 ratio in wild-type sample to obtain a clinically effective diagnostic assay.

6 CHAPTER SIX SURFACE CHEMISTRY AND MORPHOLOGY IN BIO-NANOPARTICLE OPTICAL IMAGING AND SINGLE BIO-NANOPARTICLE SENSING USING SP-IRIS

In Chapters 4 and 5, we showed how SP-IRIS can count single protein and nucleic acid molecules via nanoparticle-labeling with ultra-high sensitivity. In this chapter, we demonstrate how we can expand nanoparticle-based detection for individual biological nanoparticle like viruses.

6.1 Motivation for biological nanoparticle sensing

Synthetic and natural nanoparticles — generally defined as having a size of 10–100 nm — have enormous utility as well as potential adverse impact in biotechnology, human health, medicine, and food safety [210–213]. Detection and characterization of biological nanoparticles represent unique challenges and opportunities. Viruses are the most abundant species on earth, with an estimated ~10^{32} phages in the biosphere [214] and ~10^{7} viruses on average in a milliliter of seawater [215]. The detection and identification of individual virions are of significant interest due to their potential relation with many infectious diseases and human cancers [13]. Early and sensitive detection of infections is important especially for high impact diseases leading to epidemics. Consequently, many detection systems for viral diagnostics have been developed during the outbreaks [216]. Thus, there is always a need for single-particle detection systems that are robust, affordable, high-throughput, sensitive in heterogeneous media, and less technically difficult.

Due to the growing need in rapid detection and quantification, there has been a significant interest in the development of sensors for biological nanoparticles. For reliable

results, it is crucial to detect them with high sensitivity. Fluorescence-based microscopy techniques have been developed extensively for detection of biological nanoparticles and molecules [217,218]. They require fluorescence labeling of the single natural nanoparticles, which makes them less applicable for a variety of samples. Moreover, nonspecific binding of the fluorescent labels to the other components in the heterogeneous media or formation of aggregates remains as a challenge in fluorescence detection systems along with the inconstancy of the fluorescence signal independent of the size of the biological nanoparticles [46]. Also, irreversible photobleaching of the fluorescent label limits observation time. Electrical sensors also provide single virus or biological particle detection. However, as they are very dependent to the environmental conditions and the properties and content of the sample media such as pH, heterogeneity, and changes in ionic strength, they suffer from specificity and selectivity issues [219,220].

Optical biosensors are highlighted with their distinct properties and advantages such as high sensitivity, easy adaptation to multiplexed systems, and portable operation capability [221,222]. They are also attractive due to their non-invasive nature. Elastic light scattering-based direct detection methods that require no molecular labels are more advantageous than fluorescence methods that may suffer from variability and temporal decay of the signal due to photobleaching. However, as the elastically scattered light intensity induced by the illumination of the nanoparticle's scales with the sixth power of the particle size, it is very difficult to detect small biological nanoparticles over the background scattering. Thus, eliminating the background noise for small particle detection is of vital importance.

In this chapter, we review several optical technologies for label-free BNP detectors with a focus on imaging systems. We compare the surface-imaging methods including dark-field, surface plasmon resonance imaging and interference reflectance imaging. We discuss the importance of ensuring consistently uniform and smooth surface coatings of capture molecules for these types of biosensors, and summarize several methods that have been developed towards addressing this challenge. Finally, we show real-time detection of viral particles without any labels using SP-IRIS technology.

6.2 Label-free optical imaging detectors of single biological nanoparticles

Conventional light scattering microscopy cannot resolve features much smaller than the illumination wavelength due to the diffraction limit. When we consider imaging a sensor surface with a sparse distribution of nanoparticles, classical understanding of optical resolution may no longer be the primary concern. In this case, objects of interest, i.e., nanoparticles may not be visible above the background, since they scatter light very weakly. Radioisotope and fluorescence staining, therefore, have historically been used to ‘decorate’ or ‘label’ biological nanoparticles (BNPs) and increase their visibility. These labels can add molecular specificity (for example, by using a fluorescently labeled antibody or complementary oligonucleotide), but they may hinder characterization of physical properties and also increase assay complexity and cost. To address applications where these are major concerns, a variety of label free assays for BNPs have been developed. Many of these techniques utilize light, and either directly or indirectly detect light scattered by the BNP. Label-free optical imaging biosensors are those which use imaging optics to rapidly measure a large sensor surface area. In this section, we describe three members of the

family of label-free optical imaging biosensors, which are dark-field microscopy (DF/TIRM), surface plasmon resonance imaging (SPRi), and interference reflectance imaging (IRIS, iSCAT) [37,108,223,224]. We also introduce the notion that for label-free imaging approaches, even more than for other types of label-free sensors, the surface morphology of the sensor's functionalization is extremely important. Table 6.1 shows a comparison of label-free optical imaging biosensors utilized in detection of BNP. The implementation and availability of these technologies at diagnosis near-patient is also shown. Point-of-care (POC) testing requires miniaturized, portable platforms and avoidance of time-consuming steps of analysis. Among these technologies, dark-field microscopy and iSCAT are not deployable to majority of clinical locations at POC. While SPRi is very sensitive and highly employed, the use of SPRi has not yet been demonstrated at POC. On the other hand, SP-IRIS has POC capability for virus detection. It allows virus detection in complex media via the use of disposable cartridges and a benchtop-size microscope with minimal sample and reduced exposure risk.

Technology	Optical system	Analyte	Matrix	Detection limit	Availability at POC	Advantages	Ref.
Dark-field microscopy	Total Internal Reflection Dark-Field Microscopy	Influenza virus	Buffer	$1.26x10^4$ pfu/mL	Not applicable	Simple optical system and no elaborated sample preparation	[225]
Surface plasmon resonance	Surface plasmon resonance imaging	HIV-based virus-like particles	Buffer	-	Applicable but not shown yet	Efficient for quantification and characterization	[224]
	Surface plasmon resonance imaging	Influenza A virus	Buffer	0.2 fg/mm^2	Applicable but not shown yet	Mass/size measurement of single viral particles	[226]
Interference reflectance imaging	iSCAT	Lipid nanodomains responsible in cell signaling	Lipid-oil solution	Tracking individual domains in lifetime of 0.22 ± 0.06 s	Not applicable	Time-lapse imaging of dynamic creation and destruction of lipid nanodomains	[227]
	SP-IRIS	Exosomes from a HEK 293 cells	Buffer	$3.94 x10^9$ particles/mL	Not applicable	Phenotyping and characterization of exosomes directly from human cerebrospinal fluid	[228]
	SP-IRIS	Recombinant vesicular stomatitis virus Ebola model	100% fetal bovine serum	100 pfu/mL	Applicable	Real-time imaging of individual viruses, highly sensitive rapid detection platform of pathogens with minimal sample preparation	[229]

	SP-IRIS	Ebola virus, Zaire Strain-variant Mayinga	100% fetal bovine serum	$1x10^5$ pfu/mL	Very applicable	Disposable polymer-paperfluidic cartridge, detection limit 10–100 times more sensitive than commercial rapid tests	[37]

Table 6.1 A comparison of label-free optical imaging biosensors in detection of biological nanoparticles (BNP).

6.3 Importance of surface morphology in single particle optical imaging

Biofunctionalization of the sensor surface should be measured systematically. Procedures for biomolecule immobilization are employed in similar ways with the same principles; however, surfaces are usually poorly characterized. Any modification on the sensor may change the ability of the device to detect biomolecules. For instance, in optical resonators, the lowest possibly detectable concentration of the target in sample is usually proportional with the resonance linewidth (also called quality factor) [230]. Poor surface chemistry may cause an increase in linewidth, however, which increases the detection limit [231]. Since surface biofunctionalization may occur in multiple steps, it is important to track these changes on the surface in each step and optimize accordingly [35].

In surface plasmon resonance biosensors, microorganisms and viruses can be detected via local changes in the refractive index. Due to the confinement of surface plasmon polaritons (SPPs) to within 100–200 nm of the gold-liquid interface however, only a portion of the entire bacteria is detectable. For the same reason, the sensitivity of these type of biosensors also depends on the separation distance between the target BNP and the gold film. Furthermore, BNPs with a diameter larger than about the evanescent field decay constant are measured with decreasing sensitivity [232]. Hence, surface morphology must be designed accordingly. Despite being one of the most applied optical imaging techniques for BNPs, some limitations constrain SPR based imaging systems. Having a few hundred-nm penetration depths of the evanescent field into the dielectric medium limits the detection of smaller sized particles [233].

SPR imaging (SPRi) enables multiplexed and real-time measurements [234,235].

However, sensitivity is a limiting issue in SPRi compared to the conventional SPR due to the difficulties in sample delivery in real time over the multiplexed spotted sensor surface. The use of microfluidic flow cells and amplifying the signal with various techniques improve signal-to-noise ratio in many applications [73,235–238]. The effective thickness of the captured target layer is the layer of analyte on top of the surface probes on the SPR sensor, which has the major effect on the magnitude of SPR response. The measurements are based on the uniformity and consistency of these two layers on the sensor. However, the refractive index change within the layers also affects the SPR shift in the system. In conventional SPR imaging system designs, it is hard to keep the immobilized probe layer fixed and free of variations, due to the possible non-specific bindings and changes in the surface chemistry of the layer in real-time measurements.

Although the noise is an issue and relatively greater than in SPR, SPRi is utilized in many applications for detection of cells and bacteria [239]. In one approach, the SPRi sensor surface was modified with a hydrogel-based interaction layer. When red blood cell-surface antibody interaction is investigated real time, it was found that the noise level was very high due to the non-specific binding and remaining total mass of cell debris on the surface [239]. As a result, only limited number of cell binding was detected.

Until recently, SPRi were not in use for detection of nanoscale BNPs due to certain limitations. Mainly, restrictions stemming from lateral resolution, SPR-based sensors remained useless for detection of viruses and virus-like particles [240]. However, in 2010, Wang et al. showed that with the right surface chemistry and functionalization, imaging and detection of virus particles on SPRi surface is achievable [226]. The diffraction

patterns created by surface plasmon waves of the individual viral particle scattering were used to identify the particles and distinguish them from the background noise and interference patterns. Since the intensity of diffraction pattern increases with the size of the BNP, they were also able to measure the size of the BNP. They have compared the Influenza A Virus (IAV) particles versus artificial silica nanoparticles. Even though the synthetic nanoparticles do not adhere to the surface and disappear in the real-time imaging measurements, when they functionalized the sensor surface properly, they can capture, image and count the viral particles on the surface. They obtained a non-specific and irreversible adsorption of the viral particles on the bare gold sensor surface. On the other hand, when they compared different surface modification such as PEGylation and antibody coating, they obtained lower intensity profiles. Even though PEG-coating is usually used to prevent non-specific binding and increase the sensitivity by lowering the background, in this particular case, on PEGylated surface, viral particles were observed as transient events, which shows the effect and diversity of surface morphology for each technique and target. Also, anti-influenza A antibody-coated surfaces provided reversible binding in real time measurements. As seen in Figure 6.1A, different surface modifications created different signal intensities. Even though bare gold sensor had more capture, it cannot differentiate between the virus types, whereas anti-influenza A antibody modified surface was applied successfully for Influenza A virus capture and remained fairly inert to the other type of virus, HCMV, yielding specific binding and significantly higher signal than the nonspecific bindings. By improving surface properties and system stability, the noise was reduced and they obtained a noise level of 0.3 mDeg which can detect 13 nm-sized nanoparticles. The

imaging intensities of the viral particles were used to determine their size, which was found as 109±13 nm.

In another study, viral particles were counted using SPRi [224]. When the viral particles were captured on the sensor surface, they appeared as bright dots on the background and counted in a very small field of view to improve the detection limit and block the signals coming from the other regions. The authors have showed that they can detect various concentrations of human immunodeficiency-virus-like-particles (HIV-VLP- spherical, 100–140nm in diameter), Influenza A virus (IAV- spherical, 80–120 nm in diameter), tobacco-mosaic virus (TMV- elongated cylinder, 15–18 nm in diameter and around 300 nm in length) in complex buffers. They prepared the sensor surface in multiple steps. They first coated the surface with streptavidin, and then, with biotinylated antibody layer. While they checked surface roughness, a uniform and temporal constant background was observed. If a smooth and low-rough surface was not obtained at first, they kept saturating the surface with antibodies to obtain a low-roughness in order to lower the background and to be able to distinguish the VLPs from the background roughness. As seen in Figure 6.1B, after subtraction of the background, spherical IAV particles (a) and HIV-VLP (b) were characterized. The binding event is also confirmed with the intensity increase and stabilization in the SPR signal in Figure 6.1B (c) and (d), which is correlated with the size of the particle. However, binding of TMV could not be visualized due to its smaller size in diameter and vanishing on the surface roughness. Even though the surface modification with antibodies was successful and enough for the visualization of ~100 nm-sized viral particles, it was limited for imaging of smaller particles due to the crudity of the

sensor surface.

Moreover, in a study where the optimal conditions for SPR-imaging of nano-objects are discussed, it has been explained that the layer on the sensor surface and its roughness have great importance in local reflectivity resonance and in signal-to-background ratio [241]. In order to have this ratio high, the reflectivity should be minimum; however, due to the roughness and inhomogeneity of the substrate and the layer on the surface, the achievable minimum reflectivity is limited which can be obtained as minimum as 1%. The authors were able to lower this by using different techniques to prepare the substrate surface such as magnetron sputtering of gold on glass yielding a proper thickness and 0.1% reflectivity.

Limitations emanating from illumination profile necessitate a higher surface sensitivity compared to other types of microscopy such as confocal-based microscopy. Although the use of dark-field microscopy has been moderately explored in detection of BNPs, dielectric nanoparticles and virus particles have been successfully detected using TIR-based dark-field microscopy with a sensitivity down to ~100 nm for virus particles [225,242]. Moreover, in order to improve sensitivity and obtain a more uniform illumination profile, in addition to TIR-illumination via a prism or an objective, planar waveguides can be used in the evanescent-field microcopy. The sample can be placed in the core layer of the waveguide which is then exposed to the evanescent part of the guided light in a similar way to TIR illumination [243,244]. As a result of this configuration, even though the penetration depth of and evanescent field is around 100–200 nm, the depth of evanescent field can be regulated from 100 nm to a micron via tuning the thickness and

refractive indices of the core and cladding layers of the waveguide [245]. With an evanescent light-scattering microscopy technique, a simultaneous fluorescent and high sensitivity scattering imaging has been done for efficient detection surface binding of BNPs in a label-free way [246]. As well as all the other techniques, in this technique, in order to obtain highest sensitivity based on evanescent illumination, background scattering must be suppressed. Therefore, a three-layer waveguide design was utilized. For refractive index matching and repressing the roughness of the core layer (root-mean-square surface roughness <1 nm), a silica core layer in between organic fluorinated polymer (CYTOP) cladding layers was used. By this way, the stray lights were reduced while the signal-to-background ratio was improved by enhancing the scattered light coming from the BNPs in aqueous environment. Single lipid vesicles were visualized with scattered and fluorescent light for demonstration as seen in Figure 6.1C. Individual lipid vesicles (~150 nm diameter) were capture on the sensor surface via specific protein receptor binding and size of them was determined. Moreover, after confirmation with a fluorescent dye, the same labeling was also achieved with 18nm-gold nanoparticles in order to prove the applicability of the technique with very small gold nanoparticle for studying single molecule interaction with surface-immobilized vesicles. In addition to labeling, molecular interaction on the surface bound vesicles was also determined with the same technique with high sensitivity. To do so, the surface of the silica region of the waveguide was modified with a layer of polymer called PLL-g-PEG/PLL-g-PEG-biotin for immobilization of lipid vesicles. It is known that this modification provides a low-rough surface and mediates strong binding, while it protects the nature of the molecular interaction and prevents unspecific binding of other

biological molecules in the solution [247]. IgG binding to immobilized-lipid vesicles was monitored in scattering mode with a scattering intensity change.

Nearly all of the considerations mentioned earlier, regarding the impact of surface functionalization on the performance on SPR/SPRi biosensors, are applicable to interference reflectance BNP detectors as well. There are however a few salient differences. First, while SPR/SPRi biosensors utilize SPP waves that are confined to a narrow region above the gold film interface, interference reflectance sensors detect only far-field scattering. Second, since SPP waves are highly directional, SPP diffraction from a BNP creates a relatively large (with respect to the far-field diffraction limit) and asymmetric feature in the SPRi reflectance image. By comparison, interference reflectance sensors are nearly always diffraction-limited imaging systems that register the presence of a BNP as a symmetric point spread function. Together, these differences may provide reason enough to believe that interference reflectance imaging is more suitable for the detection and characterization of BNPs. Consider that interference reflectance is much less sensitive to variations in the optical thickness of the surface coating, which can be different for two different protein spots, even on the same chip. Additionally, the extended and asymmetric effect of a BNP on the propagating SPPs may reduce the maximum number or density of BNPs that can be captured onto the sensor before they can no longer be enumerated, lowering the dynamic range — although, dynamic measurement may be able to ameliorate this problem.

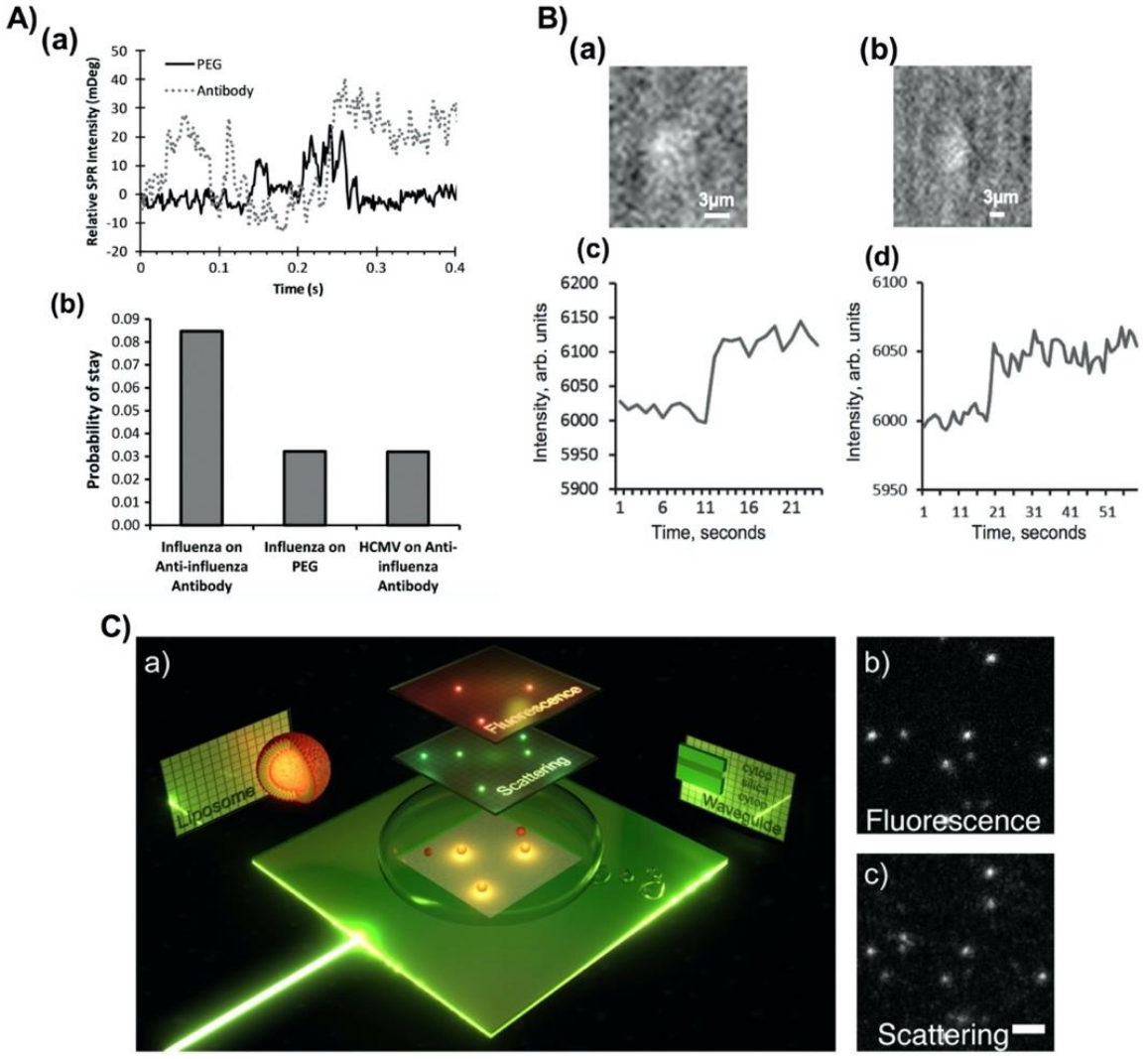

Figure 6.1 A) (a) SPR intensity profiles for influenza A viral particles captured on PEG and anti-influenza A antibody-functionalized sensor surfaces. (b) Relative binding probabilities of influenza A on PEG and anti-influenza A antibody-functionalized surfaces, and binding of a different virus HCMV on anti-influenza antibody spots as a control. Adapted from [226] Copyright 2010 National Academy of Sciences. B) A SPRi micrograph of (a) IAV or (b) HIV-VLP captured functionalized surfaces. Viruses appear as bright spots on grey background. Intensity change with the binding event of IAV and HIV-VLPs is seen in (c) and (d) as signal increase, respectively. Reprinted from Anal. Biochem., 486, V. Shpacovitch, V. Temchura, M. Matrosovich, J. Hamacher, J. Skolnik, P. Libuschewski, D. Siedhoff, F. Weichert, P. Marwedel, H. Müller, K. Überla, R. Hergenröder, A. Zybin, Application of surface plasmon resonance imaging technique for the detection of single spherical biological submicrometer particles, 62–69, Copyright 2015, with permission from Elsevier [224]. C) (a) Schematic representation of the planar waveguide chip and detection of fluorescently labeled vesicles in (b) fluorescence and (c) scattering modes. Reprinted with permission from ACS Nano 2015, 9, 12, 11849–11862. Copyright 2015 American Chemical Society [246].

As mentioned earlier chapters, IRIS can be used for virus detection via surface-immobilized antibody probes. In a study, the binding of viral particles to specific antibody spots was compared with non-specific antibody spots, with a limit of detection of $3x10^5$ PFU/mL. Very few bindings of virions above the background was observed (Figure 6.2A (a)) [111]. Note that in this study, captured BNPs were not detected individually – instead, an ensemble measurement was made by monitoring the reflectivity spectrum of the surface. In later studies, a high numerical aperture objective was used to detect the faint interference signal from individual virions. Calculating the size of a particle from the bright-ness of the resulting spot was nontrivial, because increasing the particle size increases the position of its centroid above the reflecting surface, thereby slightly increasing the optical path length difference between forward- and back-scattered light [46]. Once the substrate film thickness and surface morphology were optimized, individual BNPs ranging from 50 nm to 200 nm were detected by affinity-based capture in various complex media with SP-IRIS [248]. Specifically, *vesicular stomatitis virus* (VSV) BNPs with an ellipsoidal shape of around 70x180 nm were captured on antibody-immobilized sensor surfaces and individually counted as seen in Figure 6.2B. Even though various complex media such as serum or whole blood were used, background noise was reduced by eliminating nonspecific binding of particles with different sizes. In this study, as well as others, proper surface morphology and functionalization were achieved via coating the sensor surface with a non-fouling copoly-(DMA-NAS-MAPS) polymer [115,249]. The ssDNA and antibody capture probes were immobilized on the polymer under certain conditions to obtain the perfect spot morphology. The layered surface was checked with IRIS, and the thickness of ssDNA and

antibody spots were determined after each modification. Thus, the smooth, uniform, and low-rough surface morphology was confirmed before further steps. In order to have a better spot morphology and target capture efficiency, the authors immobilized antibody probes via DNA-directed immobilization (DDI). For this, antibodies were conjugated with 40-mer-long oligonucleotides. The complementary sequences of these ssDNAs were selected as the surface probes. ssDNA surface probes were immobilized on the sensor surface. The chips were then incubated with the antibody-DNA conjugates; therefore, anti-VSV antibodies were immobilized on the sensor surface with DNA bridges. This hybridization was also confirmed with IRIS measurements and surface roughness is validated. Although many layers of modification have been done on the sensor, since the roughness was appropriate and confirmed with low-magnification measurements, captured VSVs were easily distinguished from the background yielding a high signal-to-noise ratio. Moreover, same experiments also were repeated with direct antibody immobilization. When the VSV-capture results were compared, it was shown that DDI improved surface morphology and probe density on the surface; hence, a much higher dynamic range was obtained with DDI-antibody spots. Furthermore, since the recognition sites of the capture antibodies were more available and the antibodies more flexibly tethered, much fewer total antibodies were needed to achieve the same binding affinity of the spot. Specifically, equivalent virus capture was observed even when the average surface density of antibodies was 6x lower. Finally, since the spot printing was performed with only DNA oligonucleotides, the spot uniformity & smoothness as well as process repeatability was greatly improved.

In another study, real-time rapid counting of virus was performed in serum samples using SP-IRIS [229]. The surface of the SP-IRIS chip and setup were modified with antibodies as a highly sensitive rapid detection platform for pathogen detection with minimal sample preparation. Captured VSV particles on the sensor represented higher signals and with the optimal surface chemistry described earlier, no non-specific binding coming from the complex media was observed. As a result, VSV-Ebola model was detected at a concentration of as low as 100 PFU/mL in less than 30 min.

Moreover, digital exosome detection was also demonstrated using SP-IRIS (Figure 6.2C) [228]. In this study, the size and multi-phenotype information from the same exosome were obtained. The size distribution for the exosomes from HEK 293 cell line was determined as 50–200 nm. Despite being very low refractive index and at very low concentrations in the real samples, with properly immobilized antibodies and smooth background, exosomes were captured and digitally counted with a detection limit of $3.94x10^9$ particles/mL, which is very sensitive compared to conventional characterization techniques. Detection and characterization are two different problems for BNPs. Even though the detection is possible with these techniques, characterization needs to be done with the proper instrumentation and surface chemistry. Here, it is important to determine the size of the exosome particles. In order to determine the size, the surface roughness must be small enough to be able to differentiate between the BNPs since specific elevation of NPs due to surface morphology affects the perceived size as seen in Figure 6.2D [38].

Interferometric scattering microscopy (iSCAT) also depends on the background during the measurements. Although the polarizability of the nano-object is large enough

and there is no theoretical limit for detection, the limit stems from the nature of the background where the nano-object of interest presents. iSCAT can reach high signal-to-noise ratio in real-time measurements of localized nanoparticles. In a study, detection and tracking of single, unlabeled 45 nm *Simian virus 40* (SV40) virions were shown [250]. The authors obtained an average contrast of 3.00±0.87% for the scattering signal relative to the background on a glass substrate. Moreover, the binding of virions to receptor proteins in supported membrane bilayers on the sensor surface was tracked with iSCAT. However, as the authors stated, since all the measurements were performed on plasma cleaned-glass substrates, this technique is yet suitable for imaging or tracking nanoobjects in strongly scattering media such as serum or intact cell.

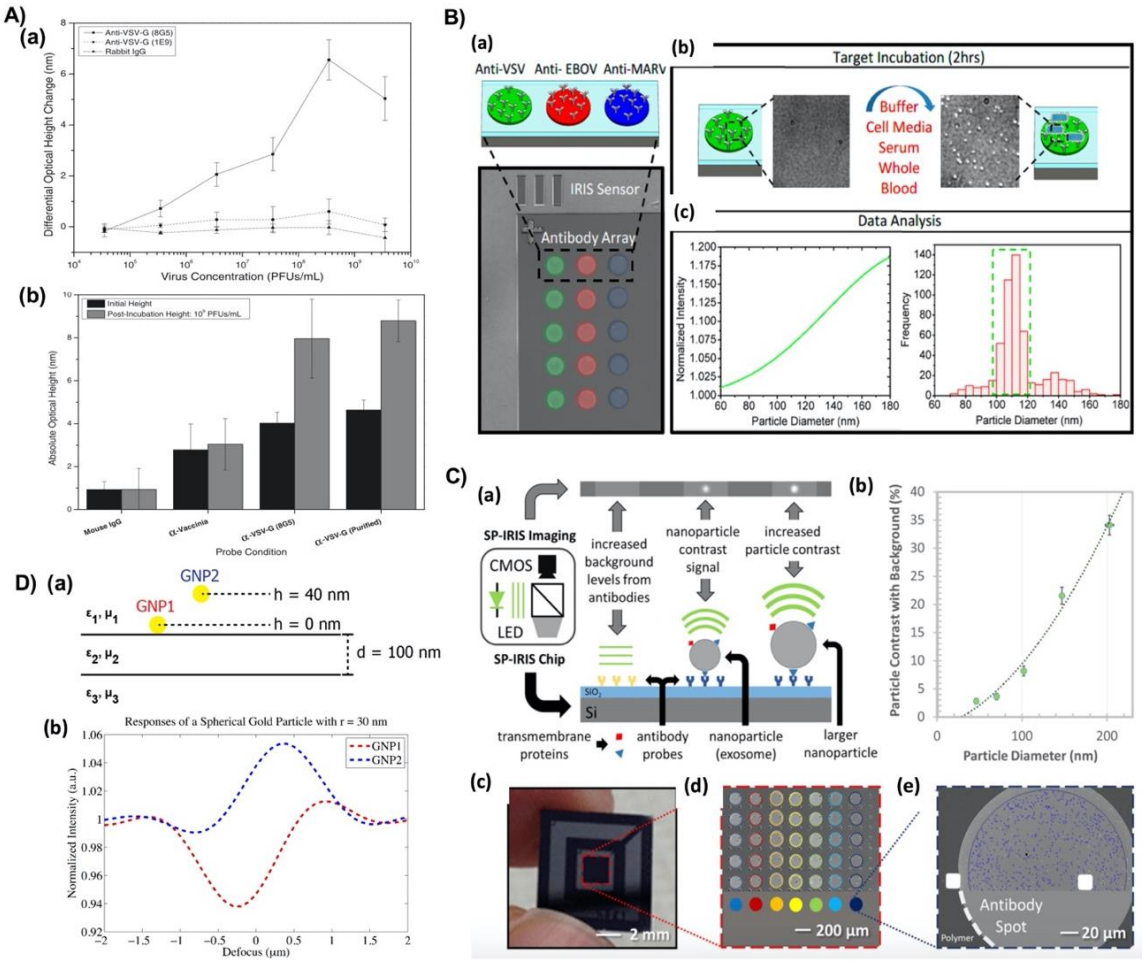

Figure 6.2 A) (a) A calibration curve for wild-type VSV (8G5) sample tested with IRIS platform. Corresponding height changes upon specific virion particle binding is shown. Greater binding indicates the greater affinity to immobilized antibody on the sensor. (b) Specific binding and low-non-specific binding are shown in the results of pre- and post-incubations with the virions. Reprinted from Biosens. Bioelectron., 26, C.A. Lopez, G.G. Daaboul, R.S. Vedula, E. Özkumur, D.A. Bergstein, T.W. Geisbert, H.E. Fawcett, B.B. Goldberg, J.H. Connor, M.S. Ünlü, Label-free multiplexed virus detection using spectral reflectance imaging, 3432–3437, Copyright 2011, with permission from Elsevier [111]. B) (a) A SP-IRIS microarray configuration with immobilized antibody spots in green, red, and blue for anti-VSV, anti-EBOV, and anti-MARV probes, respectively. (b) Data acquisition and analysis for virus identification using SP-IRIS. Captured VSV particles can be seen on anti-VSV antibody spotted sensor surface (right) when compared to pre-incubation image (left). (c) The model used for determining the size of each particle within the spot (left) and a size distribution of particles identified on the spot of the image (right). The selected region on the plot represents expected sizes of VSV. Reprinted with permission from ACS Nano 2014, 8, 6, 6047–6055. Copyright 2014 American Chemical Society [248]. C) (a) Schematic representation of the SP-IRIS detection principle (b) SP-IRIS signal for polystyrene nanoparticles with a diameter from 50–200 nm used to be reference for exosomes. (c) An

image of the SP-IRIS chip. (d) IRIS image of immobilized antibody surface probes. (e) SP-IRIS image of a captured particles on the spot which are detected via NVDX analysis. Reprinted from [228]. D) SP-IRIS measurement of spherical gold nanoparticles (r = 30 nm) at (a) h = 0 nm (GNP1) and h = 40 nm (GNP2), and (b) their interferometric responses (GNP1 shown in red, and GNP2 shown in blue). Adapted from [38] Copyright 2016 Optical Society of America.

6.4 Interferometric kinetic detection and enumeration of viral particles

Viruses are by far the most abundant species on earth. The total number of viruses/phages in the biosphere (estimated at $\sim 10^{32}$ [214]) are much larger than the number of stars in the known universe. The detection, visualization and characterization of individual viruses are of significant interest due to their relevance to many infectious diseases and human cancers [13]. Electron microscopy has been the most commonly used method for visualization and characterization of such nanoparticles, however, besides its complexity and low throughput, it does not allow for real-time detection in liquid. High-Q resonator based approaches have been shown to successfully detect individual nanoparticles given that the nanoparticle interacts with the active sensor area [251–255]. For applications that require specificity and sensitivity for samples with limited number of viruses, however, wide-field imaging of individual particles immobilized on sensor surface through interaction of their surface antigens with capture antibodies would be ideal. For imaging technologies that can visualize nanoparticles directly without any labeling, the size and the refractive index of the nanoparticles determine the strength of the signal: changes in resonant wavelength, scattered spectrum, or scattered/absorbed intensity. Therefore, visualization of viral particles remains a challenge due to their small size and low refractive index.

In end-point assays, interferometric imaging yields sufficient visibility of viral particles due to relatively high refractive index contrast between the particle (n = 1.5) and the medium (n_{air} = 1). The significant drawback of changing the medium from air to water (n_{water} = 1.33) is that it results in a three-fold reduction in signal, and thus, discriminating the particles from the local background becomes a challenging task (Figure 6.3). Nevertheless, the ability to observe particles in real-time as they bind/debind enables monitoring of individual events, which reduces the ambiguity in particle enumeration and increases the sensitivity for weak particle/probe interactions.

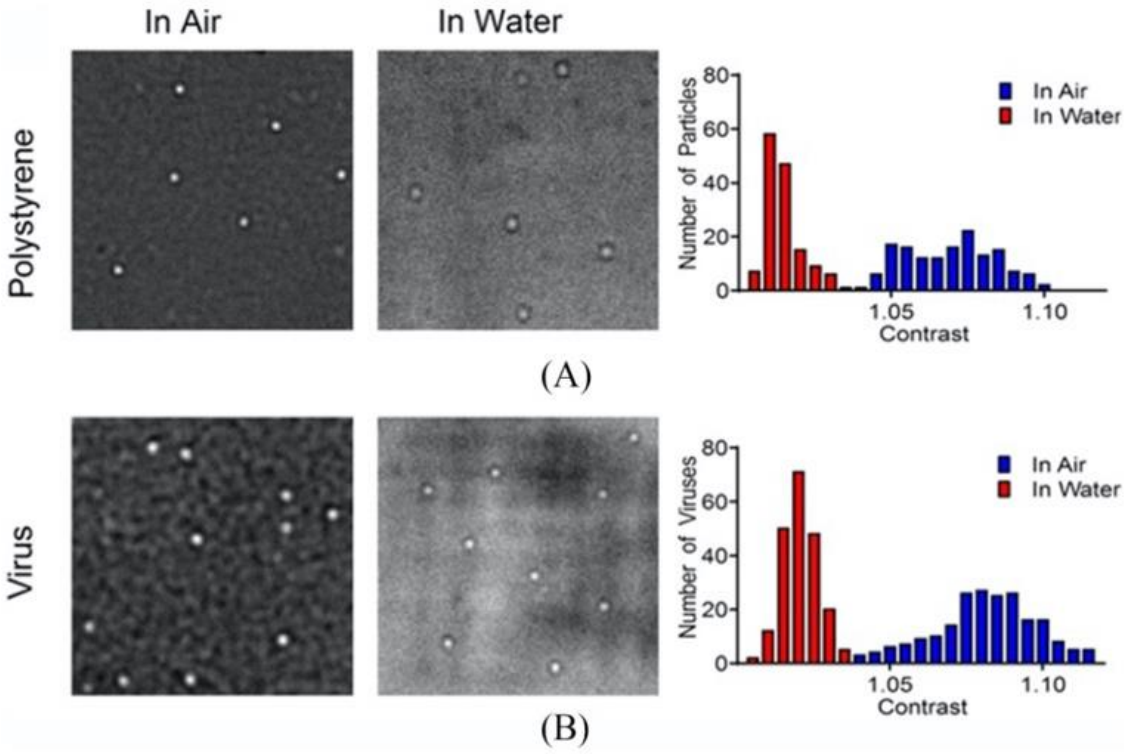

Figure 6.3 SP-IRIS images of A) 104 nm polystyrene beads and B) virus particles imaged in air and water. The visibility of single nanoparticles reduces in water by three-fold. Reprinted with permission from ACS Nano 2016, 10, 2, 2827–2833, Copyright 2016 American Chemical Society [229].

6.4.1 Real-time detection of viral particle using SP-IRIS

In order to demonstrate the capability of the wide-field viral nanoparticle detection of SP-IRIS and the Si-based cartridge, we utilized detection of 100 nm polystyrene nanospheres and virus-like particles (VLPs) as model systems for validation. These nanoparticles closely represent the size and refractive index of common viruses of interest [113].

6.4.1.1 Surface preparation

Clean silicon chips were treated with a polymeric coating as described before [117]. Briefly, the chips were immersed in MCP-4 polymer in Coat-on solution (Lucidant Polymers) for 30 min, rinsed with deionized water, dried under nitrogen and cured for 15 min under vacuum at 80°C. Streptavidin (Sigma Aldrich) and rabbit anti-EBOV VLP polyclonal antibodies (IBT Bioservices) were arrayed on the polymer coated chips at 3 mg/mL concentration in PBS using a SciFlexArrayer S3 non-contact spotter (Scienion) at 20 °C, and 57% humidity. Following overnight incubation in humid chamber, the surfaces were blocked with 1xTBST with 0.05% Tween-20 for 30 min, washed with deionized water and dried under nitrogen. The printed arrays had 155 μm diameter spots at 245 μm spot-to-spot distance.

6.4.1.2 Instrument design

SP-IRIS instrument employs a low-magnification objective (20X/0.45 NA). This configuration provides sufficient visibility for viral pathogens larger that 100 nm in size. For detecting smaller viruses, a higher magnification objective (for example 40X) can be substituted. With the higher magnification objectives, the technique has the demonstrated

ability to detect viruses down to 50 nm in size. The instrument (Figure 6.4) is compact (12 in wide x 18 in deep x 12 in tall), and supported by custom manufactured stainless-steel plates and brackets for added stability and alignment precision.

As a common-path interferometry imaging technique, SP-IRIS employs Köhler illumination where the back focal plane of the objective and the light source are in conjugate planes. This configuration allows adjustment of the illumination geometry, improving the visibility of scattering particles by ~3 fold as demonstrated in earlier work [256]. The Köhler illumination arm consists of a ring-actuated diaphragm followed by a 1:1 4-f system with 60 mm achromatic lens doublets (Thorlabs), and the illumination NA is reduced to 0.3 using the diaphragm. The LED (525 nm central wavelength, 40 nm FWHM, LedEngin) is mounted on an integrating sphere (Thorlabs) for a uniform output beam. The light scattered from particles and reflected off the surface are collected with an extra-long working distance, 20X/0.45 NA objective with correction ring (CFI S Plan Fluor ELWD 20X, Nikon), and detected at the 12.3 MP monocolor CMOS camera (FLIR) with global shutter. Sample displacement along the XYZ directions is implemented using motorized stages (Thorlabs, MTS25-Z8 (X and Z), MTS50-Z8 (Y)). For data acquisition, Micromanager is utilized.

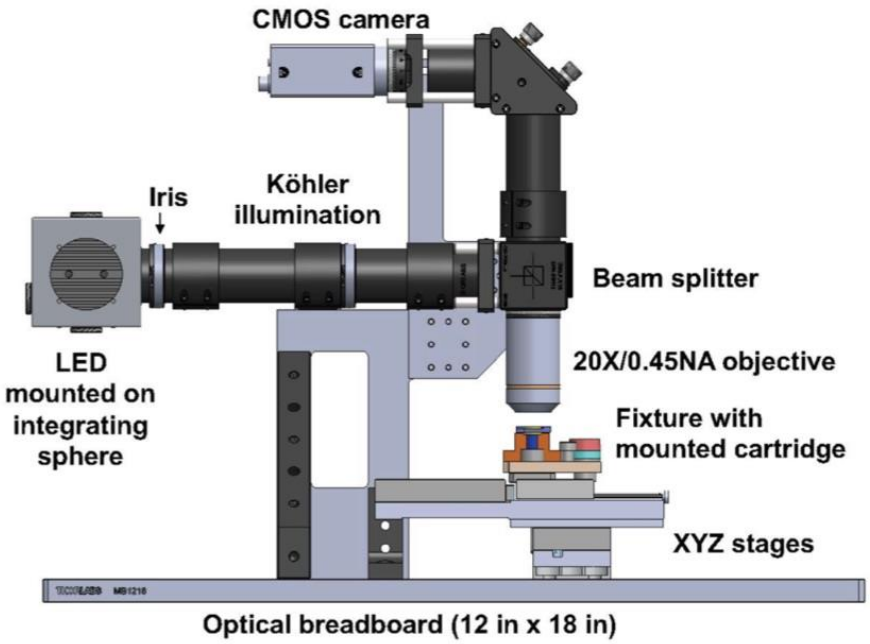

Figure 6.4 Schematic representation of the SP-IRIS detection instrument.

6.4.1.3 Real-time capture and visualization of polystyrene nanoparticles and VLPs

100 nm biotinylated polystyrene spheres (Nanocs, 1% solid) and Ebola virus-like particles (IBT Bioservices) were diluted in PBS at 250X and 50X from stock, respectively, and introduced to the cartridges that include the corresponding chips at 5–8 μL/min flow rate using a syringe pump. For both chips, 1X PBS was flown initially through the system to fill the chamber, and baseline measurements were taken to check the cleanliness of the sensor surface. Then, nanoparticles were introduced into the flow chamber by switching solutions using a 4-way valve. Once the sample reached the chamber, data acquisition is initiated. Z-stack images were taken (at 60 ms exposure time) over a 10 μm range of z-positions in 200 nm increments at every time point, with a temporal resolution of 1 min. The recorded data that has the time dependency and defocus profile information is then analyzed with a custom MATLAB code, which uses template matching for particle

detection from differential intensity images [46]. The results are presented in Figure 6.6, where the movie strips display cropped images from representative regions of spots corresponding to different time points along the curves shown below. In Figure 6.5A, detection of biotinylated polystyrene nanoparticles on a chip with streptavidin spots is demonstrated, whereas in Figure 6.5B, detection of VLPs on a chip with VLP antibody spots are shown. In each case, the reported particle density (counts/spot) corresponds to the number of particles counted within a 100 μm × 100 μm square area inside the spot. For these experiments, the particle concentrations were low, and did not lead to a saturation signal as evident from the presented data in Figure 6.5. The background noise in these images can be further reduced by averaging multiple frames at each z-position. Even without any averaging, we were able to demonstrate dynamic detection of individual particles bound on the surface in a wide-field configuration.

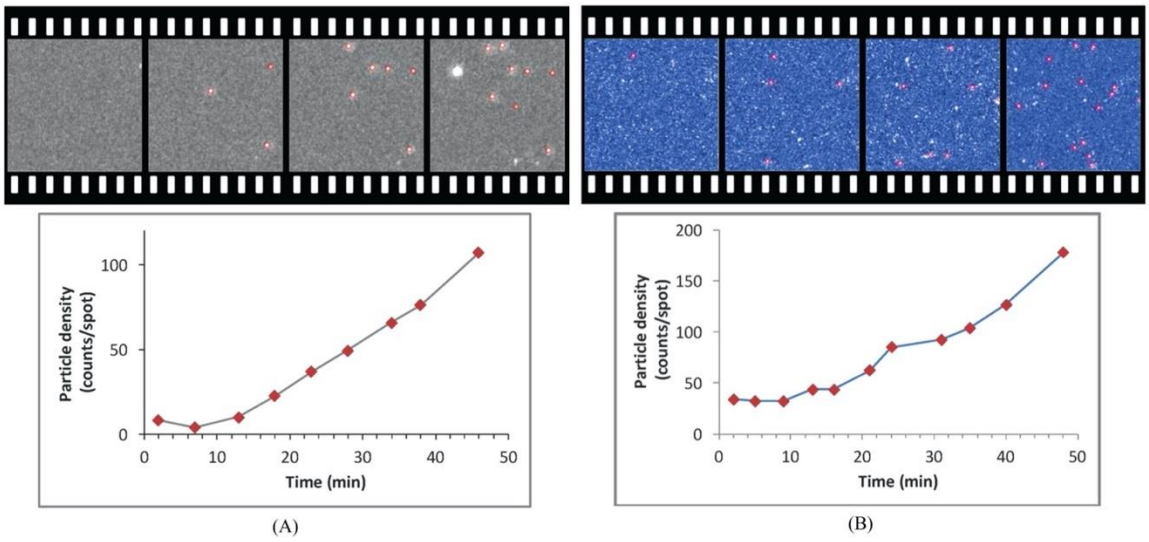

Figure 6.5 **Real-time detection and enumeration of binding of A) 100 nm polystyrene particles and B) VLPs on sensor surface. Movie strips show representative cropped images (at time points: 5, 20, 30, and 50 min. The lines are provided as guides for the eye. Reprinted from [113] Copyright 2018 IEEE.**

7 CHAPTER SEVEN CONCLUSIONS AND FUTURE DIRECTIONS

7.1 Conclusion

In this dissertation, we describe the design and implementation of four digital assays, which perform rapid protein, nucleic acid and biological nanoparticle detection in microarray format with great sensitivity.

The emergence of need for reliable and rapid biomarker detection led the field to develop simple and accurate systems for biomarker detection. SP-IRIS is a promising tool for sensitive and reliable biomarker detection. It can be used in detection of various types of biomarkers. Here, we applied this technology particularly in three group of biomarkers. In Chapter 2, we described how different modalities of IRIS is utilized for different purposes. While low-mag modality is ideal for surface profiling, morphology characterization, biomass accumulation quantification, high-mag modality, SP-IRIS, is excellent for nanoparticle detection. Here, we described a quantitative approach to performing SP-IRIS imaging. This work also laid the groundwork for the development of a high throughput, polarization-enhanced version of SP-IRIS. Moreover, we discussed about the strategy SP-IRIS advanced to perform kinetic measurements of nanoparticle binding.

In Chapter 3, we discussed how an ideal microarray surface can be and how we can achieve this with proper design. Also, we have demonstrated that low-cost disposable sensor chips and microfluidic cartridges can be manufactured using standard Si processing techniques. We showed the improvements to the instrumentation of SP-IRIS intended to enable real-time in-liquid imaging of nanoparticles as they bind to the sensor surface. We

presented the simplified microfluidic flow cell concept. Then, we presented the microarray design, surface preparation for biomarker detection assays.

In Chapters 4, 5 and 6, the development of four digital microarray assays for protein, nucleic acids and biological nanoparticles, specifically, hepatitis B viral surface antigen, microRNAs and rare mutation in an oncogene, and virus-like particles. In Chapters 4 and 5, we presented our system for imaging gold nanorod labels for the detection of molecular analytes, proteins and nucleic acids via heterogeneous or homogeneous assays. Consequently, sophisticated kinetic measurements and particle tracking enabled by SP-IRIS have the potential for broad impact in the development of new biomarkers and molecular tests. We showed how the advancements drastically improved the sensitivity in real-time assays, especially when the target molecule is in low abundancy.

As Dr. Walt mentioned the future of biological detection will be single molecule counting. As the technology advances, many tests and liquid biopsies enabled by single particle detection will replace time-consuming, troublesome and labor-intensive surgical biopsies and today's detection methods. We strongly believe that our technology will have a great impact with its capability and applicability in biomedical practices.

7.2 Future directions

In this dissertation, we demonstrated the applicability and success of polarization-enhanced SP-IRIS integrated with a disposable flow cell. It is very promising that this system can be further used to meet the needs in healthcare field.

Rapid and accurate quantification of multiple analytes is needed in the current settings of fast and furious world. We need systems that diagnose diseases with single-

molecule sensitivity in shortest time. In Chapter 5, we showed proof of principle experiments of multiplexed detection on one chip. A further step to improve detection time and multiplexing will be having multiple channels on a single IRIS chip for simultaneous detection of multiple analytes in parallel. Figure 7.1 shows SolidWorks images of a possible design for a multichannel SP-IRIS application with modified spacer and fixture for multichannel liquid handling.

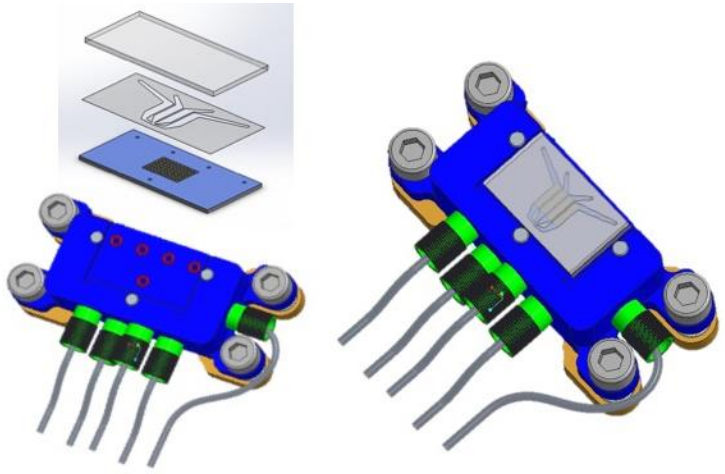

Figure 7.1 A possible design for multichannel IRIS microfluidic flow cell for future in liquid detection applications.

As seen in Figure 7.1, four channels can fit in parallel, and multiple analytes can be introduced to different section of the same chip simultaneously. This will have many advantages. First of all, it will reduce the experimental time drastically, as we would do four experiments in parallel. For instance, in microRNA detection assays, with real-time detection and homogeneous assay format, we already improved assay time from 10 h to 1 h and for four experiments, this makes from 40 h to 4 h. With multichannel design, we can further go down to 1 h for four analytes. This makes a reduction in total assay time from

40 h to 1 h which makes our technology excellent as a diagnostic tool. This design is great for especially dilution experiments. Second, since we would be using the different regions of same spotted chip for all four conditions, it will improve inter-assay coefficient of variation (CV) as well as intra-assay CV. Moreover, we can adjust the channel sizes and gaps and also integrate a lower magnification, e.g. 10x, objective with high NA. As a result, we can image multiple channel in one FOV for even higher throughput. Last, an eventual result will be the cost of our assays. It will be reduced drastically with the less need for multiple chips, sample and consumables.

Based on our preliminary results, we believe that there are many approaches that can be explored to improve SP-IRIS digital microarray technology which has a great potential to become a diagnostic tool that could be deployed in rapid diagnostics and a POC setting.

8 BIBLIOGRAPHY

[1] WHO Director-General's opening remarks at the media briefing on COVID-19 - 11 March 2020, (n.d.). https://www.who.int/dg/speeches/detail/who-director-general-s-opening-remarks-at-the-media-briefing-on-covid-19---11-march-2020 (accessed May 10, 2020).

[2] WHO Coronavirus Disease (COVID-19) Dashboard, (2020). https://covid19.who.int/ (accessed July 25, 2020).

[3] R. Lu, X. Zhao, J. Li, P. Niu, B. Yang, H. Wu, W. Wang, H. Song, B. Huang, N. Zhu, Y. Bi, X. Ma, F. Zhan, L. Wang, T. Hu, H. Zhou, Z. Hu, W. Zhou, L. Zhao, J. Chen, Y. Meng, J. Wang, Y. Lin, J. Yuan, Z. Xie, J. Ma, W.J. Liu, D. Wang, W. Xu, E.C. Holmes, G.F. Gao, G. Wu, W. Chen, W. Shi, W. Tan, Genomic characterisation and epidemiology of 2019 novel coronavirus: implications for virus origins and receptor binding, Lancet. 395 (2020) 565–574. doi:10.1016/S0140-6736(20)30251-8.

[4] N. Zhu, D. Zhang, W. Wang, X. Li, B. Yang, J. Song, X. Zhao, B. Huang, W. Shi, R. Lu, P. Niu, F. Zhan, X. Ma, D. Wang, W. Xu, G. Wu, G.F. Gao, W. Tan, A novel coronavirus from patients with pneumonia in China, 2019, New England Journal of Medicine. 382 (2020) 727–733. doi:10.1056/NEJMoa2001017.

[5] Coronavirus Disease 2019 (COVID-19) | FDA, (n.d.). https://www.fda.gov/emergency-preparedness-and-response/counterterrorism-and-emerging-threats/coronavirus-disease-2019-covid-19 (accessed May 16, 2020).

[6] S.H. Kim, J. Lee, B.H. Lee, C.S. Song, M.B. Gu, Specific detection of avian influenza H5N2 whole virus particles on lateral flow strips using a pair of sandwich-type aptamers, Biosensors & Bioelectronics 134 (2019) 123–129. doi:10.1016/j.bios.2019.03.061.

[7] L.J. Carter, L. V Garner, J.W. Smoot, Y. Li, Q. Zhou, C.J. Saveson, J.M. Sasso, A.C. Gregg, D.J. Soares, T.R. Beskid, S.R. Jervey, C. Liu, Assay Techniques and Test Development for COVID-19 Diagnosis., ACS Central Science. 6 (2020) 591–605. doi:10.1021/acscentsci.0c00501.

[8] B. Udugama, P. Kadhiresan, H.N. Kozlowski, A. Malekjahani, M. Osborne, V.Y.C. Li, H. Chen, S. Mubareka, J. Gubbay, W.C.W. Chan, Diagnosing COVID-19: The Disease and Tools for Detection, ACS Nano. 14 (2020) 3822–3835. doi:10.1021/acsnano.0c02624.

[9] K. Strimbu, J.A. Tavel, What are biomarkers?, Current Opinion in HIV and AIDS. 5 (2010) 463–466. doi:10.1097/COH.0b013e32833ed177.

[10] FDA-NIH Biomarker Working Group, BEST (Biomarkers, Endpoints, and other Tools), Updat. Sept. 25. (2017) 55. doi:10.1164/rccm.201301-0153OC.

[11] R. Aebersold, L. Anderson, R. Caprioli, B. Druker, L. Hartwell, R. Smith, Perspective: A program to improve protein biomarker discovery for cancer, Journal of Proteome Research. 4 (2005) 1104–1109. doi:10.1021/pr050027n.

[12] T.H. Tsai, E. Song, R. Zhu, C. Di Poto, M. Wang, Y. Luo, R.S. Varghese, M.G. Tadesse, D.H. Ziada, C.S. Desai, K. Shetty, Y. Mechref, H.W. Ressom, LC-MS/MS-based serum proteomics for identification of candidate biomarkers for hepatocellular carcinoma, Proteomics. 15 (2015) 2369–2381. doi:10.1002/pmic.201400364.

[13] M.C. DeSantis, W. Cheng, Label-free detection and manipulation of single biological nanoparticles, Wiley Interdisciplinary Reviews. Nanomedicine and Nanobiotechnology. 8 (2016) 717–729. doi:10.1002/wnan.1392.

[14] File:Biological and technological scales compared-en.svg - Wikimedia Commons, (n.d.). https://commons.wikimedia.org/wiki/File:Biological_and_technological_scales_compared-en.svg (accessed May 10, 2020).

[15] K. Hao, Y. He, H. Lu, S. Pu, Y. Zhang, H. Dong, X. Zhang, High-sensitive surface plasmon resonance microRNA biosensor based on streptavidin functionalized gold nanorods-assisted signal amplification, Analytica Chimica Acta. 954 (2017) 114–120. doi:10.1016/j.aca.2016.12.006.

[16] A. Tereshchenko, V. Fedorenko, V. Smyntyna, I. Konup, A. Konup, M. Eriksson, R. Yakimova, A. Ramanavicius, S. Balme, M. Bechelany, ZnO films formed by atomic layer deposition as an optical biosensor platform for the detection of Grapevine virus A-type proteins, Biosensors & Bioelectronics. 92 (2017) 763–769. doi:10.1016/j.bios.2016.09.071.

[17] H.L. Shuai, K.J. Huang, W.J. Zhang, X. Cao, M.P. Jia, Sandwich-type microRNA biosensor based on magnesium oxide nanoflower and graphene oxide–gold nanoparticles hybrids coupling with enzyme signal amplification, Sensors and Actuators. B, Chemical. 243 (2017) 403–411. doi:10.1016/j.snb.2016.12.001.

[18] L. Lan, Y. Yao, J. Ping, Y. Ying, Recent advances in nanomaterial-based biosensors for antibiotics detection, Biosensors & Bioelectronics. 91 (2017) 504–514. doi:10.1016/j.bios.2017.01.007.

[19] S. Mackay, J. Chen, Biosensor systems and applications in genomics, proteomics and metabolomics: A review, Proceedings – IEEE International Symposium on Circuits and Systems (ISCAS). (2014) 217–220.

doi:10.1109/ISCAS.2014.6865104.

[20] Y. Lee, E.K. Lee, Y.W. Cho, T. Matsui, I.C. Kang, T.S. Kim, M.H. Han, ProteoChip: A highly sensitive protein microarray prepared by a novel method of protein immobilization for application of protein-protein interaction studies, Proteomics. 3 (2003) 2289–2304. doi:10.1002/pmic.200300541.

[21] G.G. Daaboul, R.S. Vedula, S. Ahn, C.A. Lopez, A. Reddington, E. Ozkumur, M.S. Ünlü, LED-based Interferometric Reflectance Imaging Sensor for quantitative dynamic monitoring of biomolecular interactions, Biosensors & Bioelectronics. 26 (2011) 2221–2227. doi:10.1016/j.bios.2010.09.038.

[22] E. Özkumur, S. Ahn, A. Yaçin, C.A. Lopez, E. Çevik, R.J. Irani, C. DeLisi, M. Chiari, M.S. Ünlü, Label-free microarray imaging for direct detection of DNA hybridization and single-nucleotide mismatches, Biosensors & Bioelectronics. 25 (2010) 1789–1795. doi:10.1016/j.bios.2009.12.032.

[23] M.R. Monroe, G.G. Daaboul, A. Tuysuzoglu, C.A. Lopez, F.F. Little, M.S. Ünlü, Single Nanoparticle Detection for Multiplexed Protein Diagnostics with Attomolar Sensitivity in Serum and Unprocessed Whole Blood, Analytical Chemistry. 85 (2013) 3698–3706. doi:10.1021/ac4000514.

[24] O. Avci, N.L. Ünlü, A.Y. Özkumur, M.S. Ünlü, Interferometric reflectance imaging sensor (IRIS)—a platform technology for multiplexed diagnostics and digital detection, Sensors. 15 (2015) 17649–17665. doi:10.3390/s150717649.

[25] G.G. Daaboul, A. Yurt, X. Zhang, G.M. Hwang, B.B. Goldberg, M.S. Ünlü, High-throughput detection and sizing of individual low-index nanoparticles and viruses for pathogen identification, Nano Letters. 10 (2010) 4727–4731. doi:10.1021/nl103210p.

[26] A. Yurt, G.G. Daaboul, J.H. Connor, B.B. Goldberg, M. Selim Ünlü, Single nanoparticle detectors for biological applications, Nanoscale. 4 (2012) 715–726. doi:10.1039/c2nr11562j.

[27] E. Özkumur, J.W. Needham, D.A. Bergstein, R. Gonzalez, M. Cabodi, J.M. Gershoni, B.B. Goldberg, M.S. Ünlü, Label-free and dynamic detection of biomolecular interactions for high-throughput microarray applications, Proceedings of the National Academy of Sciences of the United States of America. 105 (2008) 7988–7992. doi:10.1073/pnas.0711421105.

[28] E. Özkumur, C.A. Lopez, A. Yalçin, J.H. Connor, M. Chiari, M.S. Ünlü, Spectral reflectance imaging for a multiplexed, high-throughput, label-free, and dynamic biosensing platform, IEEE Journal of Selected Topics in Quantum Electronics. 16 (2010) 635–646. doi:10.1109/JSTQE.2009.2037438.

[29] D. Sevenler, G. Daaboul, F. Ekiz Kanik, N.L. Ünlü, M.S. Ünlü, Digital Microarrays: Single-Molecule Readout with Interferometric Detection of Plasmonic Nanorod Labels, ACS Nano. 12 (2018) 5880–5887. doi:10.1021/acsnano.8b02036.

[30] J. Vörös, The density and refractive index of adsorbing protein layers, Biophysical Journal. 87 (2004) 553–561. doi:10.1529/biophysj.103.030072.

[31] E. Ozkumur, A. Yalçin, M. Cretich, C.A. Lopez, D.A. Bergstein, B.B. Goldberg, M. Chiari, M.S. Unlü, E. Özkumur, A. Yalçin, M. Cretich, C.A. Lopez, D.A. Bergstein, B.B. Goldberg, M. Chiari, M.S. Ünlü, Quantification of DNA and protein adsorption by optical phase shift., Biosensors & Bioelectronics. 25 (2009) 167–172. doi:10.1016/j.bios.2009.06.033.

[32] M. Cretich, M.R. Monroe, A. Reddington, X. Zhang, G.G. Daaboul, F. Damin, L. Sola, M.S. Unlu, M. Chiari, Interferometric silicon biochips for label and label-free DNA and protein microarrays, Proteomics. 12 (2012) 2963–2977. doi:10.1002/pmic.201200202.

[33] A. Yalçın, F. Damin, E. Özkumur, G. di Carlo, B.B. Goldberg, M. Chiari, M.S. Ünlü, A. Yalçin, F. Damin, E. Özkumur, G. di Carlo, B.B. Goldberg, M. Chiari, M.S. Unlü, Direct Observation of Conformation of a Polymeric Coating with Implications in Microarray Applications, Analytical Chemistry. 81 (2009) 625–630. doi:10.1021/ac801954x.

[34] J.W. Needham, N.L. Ünlü, C. Yurdakul, M.S. Ünlü, Interferometric Reflectance Imaging Sensor (IRIS) for Molecular Kinetics with a Low-Cost, Disposable Fluidic Cartridge, in: Methods in Molecular Biology, Humana Press Inc., 2019: pp. 15–28. doi:10.1007/978-1-4939-9616-2_2.

[35] G.G. Daaboul, C.A. Lopez, A. Yurt, B.B. Goldberg, J.H. Connor, M.S. Ünlü, Label-free optical biosensors for virus detection and characterization, IEEE Journal of Selected Topics in Quantum Electronics. 18 (2012) 1422–1433. doi:10.1109/JSTQE.2011.2180516.

[36] E. Seymour, G.G. Daaboul, X. Zhang, S.M. Scherr, N.L. Ünlü, J.H. Connor, M.S. Ünlü, DNA-Directed Antibody Immobilization for Enhanced Detection of Single Viral Pathogens, Analytical Chemistry 87 (2015) 10505–10512. doi:10.1021/acs.analchem.5b02702.

[37] S.M. Scherr, D.S. Freedman, K.N. Agans, A. Rosca, E. Carter, M. Kuroda, H.E. Fawcett, C.E. Mire, T.W. Geisbert, M.S. Ünlü, J.H. Connor, Disposable cartridge platform for rapid detection of viral hemorrhagic fever viruses, Lab Chip. 17 (2017) 917–925. doi:10.1039/C6LC01528J.

[38] O. Avci, R. Adato, A.Y. Ozkumur, M.S. Ünlü, Physical modeling of interference enhanced imaging and characterization of single nanoparticles, Optics Express. 24 (2016) 6094. doi:10.1364/oe.24.006094.

[39] J. Hesse, J. Jacak, M. Kasper, G. Regl, T. Eichberger, M. Winklmayr, F. Aberger, M. Sonnleitner, R. Schlapak, S. Howorka, L. Muresan, A.M. Frischauf, G.J. Schütz, RNA expression profiling at the single molecule level, Genome Research 16 (2006) 1–5. doi:10.1101/gr.4999906.

[40] A.H. Alhasan, D.Y. Kim, W.L. Daniel, E. Watson, J.J. Meeks, C.S. Thaxton, C.A. Mirkin, Scanometric MicroRNA array profiling of prostate cancer markers using spherical nucleic acid-gold nanoparticle conjugates, Analytical Chemistry. 84 (2012) 4153–4160. doi:10.1021/ac3004055.

[41] S. Patskovsky, M. Meunier, Reflected light microspectroscopy for single-nanoparticle biosensing, Journal of Biomedical Optics. 20 (2015) 097001. doi:10.1117/1.jbo.20.9.097001.

[42] C.F. Bohren, D.R. Huffman, Absorption and Scattering of Light by Small Particles, Wiley, 1998. doi:10.1002/9783527618156.

[43] S. Link, M.A. El-Sayed, Spectral Properties and Relaxation Dynamics of Surface Plasmon Electronic Oscillations in Gold and Silver Nanodots and Nanorods, Journal of Physical Chemistry. B. 103 (1999) 8410–8426. doi:10.1021/jp9917648.

[44] M.A. El-Sayed, Some interesting properties of metals confined in time and nanometer space of different shapes, Accouts of Chemical Research. 34 (2001) 257–264. doi:10.1021/ar960016n.

[45] P.K. Jain, K.S. Lee, I.H. El-Sayed, M.A. El-Sayed, Calculated absorption and scattering properties of gold nanoparticles of different size, shape, and composition: Applications in biological imaging and biomedicine, Journal of Physical Chemistry. B. 110 (2006) 7238–7248. doi:10.1021/jp057170o.

[46] J.T. Trueb, O. Avci, D. Sevenler, J.H. Connor, M.S. Ünlü, Robust Visualization and Discrimination of Nanoparticles by Interferometric Imaging, IEEE Journal of Selected Topics in Quantum Electronics. 23 (2017). doi:10.1109/JSTQE.2016.2639824.

[47] L. Diéauez, N. Darwish, M. Mir, E. Martínez, M. Moreno, J. Samitier, Effect of the refractive index of buffer solutions in evanescent optical biosensors, Sensor Letters. 7 (2009) 851–855. doi:10.1166/sl.2009.1161.

[48] A.D. Edelstein, M.A. Tsuchida, N. Amodaj, H. Pinkard, R.D. Vale, N. Stuurman, Advanced methods of microscope control using μManager software, Journal of

Biological Methods. 1 (2014) 10. doi:10.14440/jbm.2014.36.

[49] T.M. Squires, R.J. Messinger, S.R. Manalis, Making it stick: Convection, reaction and diffusion in surface-based biosensors, Nature Biotechnology. 26 (2008) 417–426. doi:10.1038/nbt1388.

[50] D. Sevenler, J. Trueb, M. Selim Ünlü, Beating the reaction limits of biosensor sensitivity with dynamic tracking of single binding events, Proceedings of the National Academy of Sciences of the United States of America. 116 (2019) 4129–4134. doi:10.1073/pnas.1815329116.

[51] J.O. Arroyo, P. Kukura, Non-fluorescent schemes for single-molecule detection, imaging and spectroscopy, Nature Photonics. 10 (2016) 11–17. http://dx.doi.org/10.1038/nphoton.2015.251.

[52] P. Zijlstra, P.M.R. Paulo, M. Orrit, Optical detection of single non-absorbing molecules using the surface plasmon resonance of a gold nanorod, Nature Nano. 7 (2012) 379–382. http://dx.doi.org/10.1038/nnano.2012.51.

[53] M.R. Lee, P.M. Fauchet, Nanoscale microcavity sensor for single particle detection, Optics Letters. 32 (2007) 3284–3286. doi:10.1364/OL.32.003284.

[54] X. Fan, I.M. White, S.I. Shopova, H. Zhu, J.D. Suter, Y. Sun, Sensitive optical biosensors for unlabeled targets: A review, Analytica Chimica Acta. 620 (2008) 8–26. doi:10.1016/j.aca.2008.05.022.

[55] J. Beuthan, O. Minet, J. Helfmann, M. Herrig, G. Müller, The spatial variation of the refractive index in biological cells, Physics in Medicine and Biology. 41 (1996) 369–382. doi:10.1088/0031-9155/41/3/002.

[56] V.D. Svet, About Holographic (Interferometric) Approach to the Primary Visual Perception, Open Journal of Biophysics. 03 (2013) 165–177. doi:10.4236/ojbiphy.2013.33020.

[57] E. Melnik, R. Bruck, R. Hainberger, M. Lämmerhofer, Multi-step surface functionalization of polyimide based evanescent wave photonic biosensors and application for DNA hybridization by Mach-Zehnder interferometer, Analytica Chimica Acta. 699 (2011) 206–215. doi:10.1016/j.aca.2011.05.017.

[58] R.P. Ekins, Ligand assays: From electrophoresis to miniaturized microarrays, Clinical Chemistry. 44 (1998) 2015–2030.

[59] D.S. Dandy, P. Wu, D.W. Grainger, Array feature size influences nucleic acid surface capture in DNA microarrays, Proceedings of the National Academy of Sciences of the United States of America. 104 (2007) 8223–8228.

doi:10.1073/pnas.0606054104.

[60] M.J. Bañuls, R. Puchades, Á. Maquieira, Chemical surface modifications for the development of silicon-based label-free integrated optical (IO) biosensors: A review, Analytica Chimica Acta. 777 (2013) 1–16. doi:10.1016/j.aca.2013.01.025.

[61] S.K. Njoroge, H.-W. Chen, M.A. Witek, S.A. Soper, Integrated Microfluidic Systems for DNA Analysis, in: B. Lin (Ed.), Microfluid. Technol. Appl., Springer Berlin Heidelberg, Berlin, Heidelberg, 2011: pp. 203–260. doi:10.1007/128_2011_153.

[62] F.S. Ligler, M. Breimer, J.P. Golden, D.A. Nivens, J.P. Dodson, T.M. Green, D.P. Haders, O.A. Sadik, Integrating Waveguide Biosensor, Analytical Chemistry. 74 (2002) 713–719. doi:10.1021/ac015607s.

[63] H.S. Dhadwal, P. Kemp, J. Aller, M.M. Dantzler, Capillary waveguide nucleic acid based biosensor, Analytica Chimica Acta. 501 (2004) 205–217. doi:10.1016/j.aca.2003.09.035.

[64] L. Liu, X. Zhou, J.S. Wilkinson, P. Hua, B. Song, H. Shi, Integrated optical waveguide-based fluorescent immunosensor for fast and sensitive detection of microcystin-LR in lakes: Optimization and Analysis, Scientific Reports. 7 (2017) 3655. doi:10.1038/s41598-017-03939-8.

[65] Y. Liu, S. Chen, Q. Liu, W. Peng, Micro-capillary-based evanescent field biosensor for sensitive, label-free DNA detection, Optics Express. 23 (2015) 20686. doi:10.1364/OE.23.020686.

[66] C. a Rowe-Taitt, J.W. Hazzard, K.E. Hoffman, J.J. Cras, J.P. Golden, F.S. Ligler, Simultaneous detection of six biohazardous agents using a planar waveguide array biosensor., Biosensors & Bioelectronics. 15 (2000) 579–589. doi:10.1016/S0956-5663(00)00122-6.

[67] G. a. Rodriguez, S. Hu, S.M. Weiss, Porous silicon ring resonator for compact, high sensitivity biosensing applications, Optics Express. 23 (2015) 7111. doi:10.1364/OE.23.007111.

[68] C.F. Carlborg, K.B. Gylfason, a Kaźmierczak, F. Dortu, M.J. Bañuls Polo, a Maquieira Catala, G.M. Kresbach, H. Sohlström, T. Moh, L. Vivien, J. Popplewell, G. Ronan, C. a Barrios, G. Stemme, W. van der Wijngaart, A packaged optical slot-waveguide ring resonator sensor array for multiplex label-free assays in labs-on-chips., Lab on a Chip. 10 (2010) 281–290. doi:10.1039/b914183a.

[69] M. Iqbal, M.A. Gleeson, B. Spaugh, F. Tybor, W.G. Gunn, M. Hochberg, T. Baehr-Jones, R.C. Bailey, L.C. Gunn, Label-free biosensor arrays based on silicon ring

resonators and high-speed optical scanning instrumentation, IEEE Journal of Selected Topics in Quantum Electronics. 16 (2010) 654–661. doi:10.1109/JSTQE.2009.2032510.

[70] F. Dell'Olio, V.M. Passaro, Optical sensing by optimized silicon slot waveguides, Optics Express. 15 (2007) 4977. doi:10.1364/OE.15.004977.

[71] W. Bogaerts, P. de Heyn, T. van Vaerenbergh, K. de Vos, S. Kumar Selvaraja, T. Claes, P. Dumon, P. Bienstman, D. van Thourhout, R. Baets, Silicon microring resonators, Lasers & Photonics Reviews. 6 (2012) 47–73. doi:10.1002/lpor.201100017.

[72] C. Wongmanerod, S. Zangooie, H. Arwin, Determination of pore size distribution and surface area of thin porous silicon layers by spectroscopic ellipsometry, Applied Surface Science. 172(1–2) (2001) 117–125. https://doi.org/10.1016/S0169-4332(00)00847-3

[73] L. Malic, B. Cui, T. Veres, M. Tabrizian, Enhanced surface plasmon resonance imaging detection of DNA hybridization on periodic gold nanoposts., Optics Letters. 32 (2007) 3092–4. doi:10.1364/OL.32.003092.

[74] L. He, Q. Pagneux, I. Larroulet, A.Y. Serrano, A. Pesquera, A. Zurutuza, D. Mandler, R. Boukherroub, S. Szunerits, Label-free femtomolar cancer biomarker detection in human serum using graphene-coated surface plasmon resonance chips, Biosensors & Bioelectronics. 89 (2017) 606–611. doi:10.1016/j.bios.2016.01.076.

[75] A. Kussrow, C.S. Enders, D.J. Bornhop, Interferometric methods for label-free molecular interaction studies, Analytical Chemistry. 84 (2012) 779–792. doi:10.1021/ac202812h.

[76] S. Pan, L.J. Rothberg, Interferometric sensing of biomolecular binding using nanoporous aluminum oxide templates, Nano Letters. 3 (2003) 811–814. doi:10.1021/nl034055l.

[77] T. Zhang, Z. Gong, R. Giorno, L. Que, A nanostructured Fabry-Perot interferometer, Optics Express. 18 (2010) 20282–20288. https://doi.org/10.1364/OE.18.020282

[78] A.W. Peterson, R.J. Heaton, R.M. Georgiadis, The effect of surface probe density on DNA hybridization., Nucleic Acids Research. 29 (2001) 5163–5168. doi:10.1093/nar/29.24.5163.

[79] M. Zhao, X. Wang, D. Nolte, Mass-transport limitations in spot-based microarrays, Biomedical Optics Express. 1 (2010) 983. doi:10.1364/BOE.1.000983.

[80] W. Kusnezow, Y. V Syagailo, S. Rüffer, N. Baudenstiel, C. Gauer, J.D. Hoheisel, D. Wild, I. Goychuk, Optimal design of microarray immunoassays to compensate for kinetic limitations: theory and experiment., Molecular & Cellular Proteomics. 5 (2006) 1681–1696. doi:10.1074/mcp.T500035-MCP200.

[81] M. Moschallski, J. Baader, O. Prucker, J. Rühe, Printed protein microarrays on unmodified plastic substrates, Analytica Chimica Acta. 671 (2010) 92–98. doi:10.1016/j.aca.2010.05.008.

[82] S.S. Mahshid, A. Vallée-Bélisle, S.O. Kelley, Biomolecular Steric Hindrance Effects Are Enhanced on Nanostructured Microelectrodes, Analytical Chemistry. (2017) acs.analchem.7b01595. doi:10.1021/acs.analchem.7b01595.

[83] G. Shemer, Y. Atsmon, E. Karzbrun, R.H. Bar-Ziv, Collective Conformations of DNA Polymers Assembled on Surface Density Gradients, Journal of the American Chemical Society. 134 (2012) 3954–3956. doi:10.1021/ja2106543.

[84] L. Ramdas, D.E. Cogdell, J.Y. Jia, E.E. Taylor, V.R. Dunmire, L. Hu, S.R. Hamilton, W. Zhang, Improving signal intensities for genes with low-expression on oligonucleotide microarrays, BMC Genomics. 5 (2004) 35. doi:10.1186/1471-2164-5-35.

[85] B. Esteban Fernández De Ávila, H.M. Watkins, J.M. Pingarrón, K.W. Plaxco, G. Palleschi, F. Ricci, Determinants of the detection limit and specificity of surface-based biosensors, Analytical Chemistry. 85 (2013) 6593–6597. doi:10.1021/ac4012123.

[86] H. Xu, J.R. Lu, D.E. Williams, Effect of surface packing density of interfacially adsorbed monoclonal antibody on the binding of hormonal antigen human chorionic gonadotrophin, Journal of Physical Chemistry. B. 110 (2006) 1907–1914. doi:10.1021/jp0538161.

[87] Z.A. Parpia, D.M. Kelso, Empirically optimized flow cytometric immunoassay validates ambient analyte theory, Analytical Biochemistry. 401 (2010) 1–6. doi:https://doi.org/10.1016/j.ab.2009.03.050.

[88] M. Cretich, F. Damin, M. Chiari, Protein microarray technology: how far off is routine diagnostics? Analyst. 139 (2014) 528–42. doi:10.1039/c3an01619f.

[89] E. Reimhult, F. Höök, Design of Surface Modifications for Nanoscale Sensor Applications, Sensors. 15 (2015) 1635–1675. doi:10.3390/s150101635.

[90] J.M. Goddard, J.H. Hotchkiss, Polymer surface modification for the attachment of bioactive compounds, Progress in Polymer Science. 32 (2007) 698–725. doi:10.1016/j.progpolymsci.2007.04.002.

[91] A. Gori, R. Longhi, Chemoselective Strategies to Peptide and Protein Bioprobes Immobilization on Microarray Surfaces, In: M. Cretich, M. Chiari (Eds.), Peptide Microarrays. Methods in Molecular Biology, vol. 1352, Springer New York, NY, 2016: pp. 145–156. doi:10.1007/978-1-4939-3037-1_11.

[92] N.G. Welch, J.A. Scoble, B.W. Muir, P.J. Pigram, Orientation and characterization of immobilized antibodies for improved immunoassays (Review), Biointerphases. 12 (2017) 02D301. doi:10.1116/1.4978435.

[93] S. Hosseini, F. Ibrahim, I. Djordjevic, L.H. Koole, Recent advances in surface functionalization techniques on polymethacrylate materials for optical biosensor applications, Analyst. 139 (2014) 2933. doi:10.1039/c3an01789c.

[94] A. V Orlov, V.A. Bragina, M.P. Nikitin, P.I. Nikitin, Rapid dry-reagent immunomagnetic biosensing platform based on volumetric detection of nanoparticles on 3D structures, Biosensors & Bioelectronics. 79 (2016) 423–429. doi:https://doi.org/10.1016/j.bios.2015.12.049.

[95] E.A. Josephs, T. Ye, Nanoscale spatial distribution of thiolated DNA on model nucleic acid sensor surfaces, ACS Nano. 7 (2013) 3653–3660. doi:10.1021/nn400659m.

[96] E.A. Josephs, T. Ye, A single-molecule view of conformational switching of DNA tethered to a gold electrode, Journal of the American Chemical Society. 134 (2012) 10021–10030. doi:10.1021/ja3010946.

[97] R.M. Dirks, M. Lin, E. Winfree, N.A. Pierce, Paradigms for computational nucleic acid design, Nucleic Acids Research. 32 (2004) 1392–1403. doi:10.1093/nar/gkh291.

[98] A. Jayaraman, C.K. Hall, J. Genzer, Computer Simulation Study of Molecular Recognition in Model DNA Microarrays, Biophysical Journal. 91 (2006) 2227–2236. doi:10.1529/biophysj.106.086173.

[99] A. Jayaraman, C.K. Hall, J. Genzer, Computer simulation study of probe-target hybridization in model DNA microarrays: Effect of probe surface density and target concentration, Journal of Chemical Physics. 127 (2007). doi:10.1063/1.2787618.

[100] W. J.G., Excluded Volume Effects on the Rate of Renaturatiori of DNA, Biopolymers. 10 (1971) 601–613.

[101] M.F. Hagan, A.K. Chakraborty, Hybridization dynamics of surface immobilized DNA, Journal of Chemical Physics. 120 (2004) 4958–4968. doi:10.1063/1.1645786.

[102] A.W. Peterson, R.J. Heaton, R. Georgiadis, Kinetic control of hybridization in surface immobilized DNA monolayer films [14], Journal of the American Chemical Society. 122 (2000) 7837–7838. doi:10.1021/ja0015489.

[103] A.W. Peterson, L.K. Wolf, R.M. Georgiadis, Hybridization of mismatched or partially matched DNA at surfaces, Journal of the American Chemical Society. 124 (2002) 14601–14607. doi:10.1021/ja0279996.

[104] E. Southern, K. Mir, M. Shchepinov, Molecular interactions on microarrays, Nature Genetics. 21 (1999) 5–9. doi:10.1038/4429.

[105] D.J. Duggan, M. Bittner, Y. Chen, P. Meltzer, J.M. Trent, Expression profiling using cDNA microarrays, Nature Genetics. 21 (1999) 10–14. doi:10.1038/4434.

[106] M.S. Shchepinov, S.C. Case-Green, E.M. Southern, Steric factors influencing hybridisation of nucleic acids to oligonucleotide arrays, Nucleic Acids Research. 25 (1997) 1155–1161. doi:10.1093/nar/25.6.1155.

[107] F. Ekiz-Kanik, D.D. Sevenler, N.L. Ünlü, M. Chiari, M.S. Ünlü, Surface chemistry and morphology in single particle optical imaging, Nanophotonics. 6 (2017) 713–730. doi:10.1515/nanoph-2016-0184.

[108] H. Verschueren, Interference Reflection Microscopy in Cell Biology: Methodology and Applications, Journal of Cell Science. 75 (1985) 279–301.

[109] P.C. Montgomery, A. Benatmane, E. Fogarassy, J.P. Ponpon, Large area, high resolution analysis of surface roughness of semiconductors using interference microscopy, Materials Science & Engineering. B. 91–92 (2002) 79–82. doi:http://dx.doi.org/10.1016/S0921-5107(01)00977-1.

[110] D. Sevenler, N. Lortlar Ünlü, M.S. Ünlü, N.L. Ünlü, M.S. Ünlü, Nanoparticle Biosensing with Interferometric Reflectance Imaging, in: M.C. Vestergaard, K. Kerman, I.-M. Hsing, E. Tamiya (Eds.), Nanobiosensors and Nanobioanalyses, Springer Japan, Tokyo, 2015: pp. 81–95. doi:10.1007/978-4-431-55190-4_5.

[111] C.A. Lopez, G.G. Daaboul, R.S. Vedula, E. Özkumur, D.A. Bergstein, T.W. Geisbert, H.E. Fawcett, B.B. Goldberg, J.H. Connor, M.S. Ünlü, Label-free multiplexed virus detection using spectral reflectance imaging, Biosensors & Bioelectronics. 26 (2011) 3432–3437. doi:10.1016/j.bios.2011.01.019.

[112] L.J. Kricka, S.R. Master, Quality control and protein microarrays, Clinical Chemistry. 55 (2009) 1053–1055. doi:10.1373/clinchem.2009.126557.

[113] A.Y. Ozkumur, F.E. Kanik, J.T. Trueb, C. Yurdakul, M.S. Unlu, Interferometric detection and enumeration of viral particles using Si-based microfluidics, IEEE

Journal of Selected Topics in Quantum Electronics. 25 (2018). doi:10.1109/JSTQE.2018.2854548.

[114] M. Cretich, F. Damin, G. Pirri, M. Chiari, Protein and peptide arrays: Recent trends and new directions, Biomolecular Engineering. 23 (2006) 77–88. doi:10.1016/j.bioeng.2006.02.001.

[115] M. Cretich, G. Pirri, F. Damin, I. Solinas, M. Chiari, A new polymeric coating for protein microarrays, Analytical Biochemistry. 332 (2004) 67–74. doi:10.1016/j.ab.2004.05.041.

[116] L. Vanjur, T. Carzaniga, L. Casiraghi, M. Chiari, G. Zanchetta, M. Buscaglia, Non-Langmuir kinetics of DNA surface hybridization, (n.d.). doi:10.1101/2020.02.27.968081.

[117] G. Pirri, F. Damin, M. Chiari, E. Bontempi, L.E. Depero, Characterization of A Polymeric Adsorbed Coating for DNA Microarray Glass Slides, Analytical Chemistry. 76 (2004) 1352–1358. doi:10.1021/ac0352629.

[118] Lucidant Polymers - Technologies, (n.d.). https://lucidant.com/Technologies (accessed May 13, 2020).

[119] D. Ganem, A.M. Prince, Hepatitis B Virus Infection - Natural History and Clinical Consequences, New England Journal of Medicine. 350 (2004) 1118–1129. doi:10.1056/NEJMra031087.

[120] A.S.F. Lok, B.J. McMahon, Chronic hepatitis B, Hepatology. 34 (2001) 1225–1241. doi:10.1053/jhep.2001.29401.

[121] Global Hepatitis Report 2017. Geneva:, World Health Organization; 2017. Licence: CC BY-NC-SA 3.0 IGO., n.d. http://apps.who.int/iris/bitstream/10665/255016/1/9789241565455-eng.pdf?ua=1 (accessed May 3, 2020).

[122] C. Velati, L. Fomiatti, L. Baruffi, V. Piccinini, D. Prati, A. Reina, A. Lobbiani, A. Zanetti, L. Romanò, Criteria for hepatitis B virus screening and validation of blood components in Italy: The position of the SIMTI HBV working group, Blood Transfusion. 9 (2011) 455–461. doi:10.2450/2011.0014-11.

[123] World Health Organization. Global Hepatitis Programme, Guidelines for the prevention, care, and treatment of persons with chronic hepatitis B infection, 2015.

[124] World Health Organization, Screening Donated Blood for Transfussion-Transmissible Infections: Recomendation, WHO Library Cataloguing-in Publication Data, 2009. doi:10.1017/CBO9781107415324.004.

[125] A. Amini, O. Varsaneux, H. Kelly, W. Tang, W. Chen, D.I. Boeras, J. Falconer, J.D. Tucker, R. Chou, A. Ishizaki, P. Easterbrook, R.W. Peeling, Diagnostic accuracy of tests to detect hepatitis B surface antigen: A systematic review of the literature and meta-analysis, BMC Infectious Diseases. 17 (2017). doi:10.1186/s12879-017-2772-3.

[126] WHO | Urgently needed: rapid, sensitive, safe and simple Ebola diagnostic tests, (n.d.). https://www.who.int/mediacentre/news/ebola/18-november-2014-diagnostics/en/ (accessed May 3, 2020).

[127] S.H. Kim, ELISA for quantitative determination of hepatitis b virus surface antigen, Immune Network. 17 (2017) 451–459. doi:10.4110/in.2017.17.6.451.

[128] F. Yucel, E. Akcael, Development of sandwich ELISA systems for the diagnosis of hepatitis B virus surface antigen and its antibody in human sera, Journal of Microbiology and Experimentation. 6 (2018) 77–82. doi:10.15406/jmen.2018.06.00191.

[129] C. Liu, L. Chang, T. Jia, et al., Real-time PCR assays for hepatitis B virus DNA quantification may require two different targets, Virology Journal. 14 (2017) 94. http://www.embase.com/search/results?subaction=viewrecord&from=export&id=L616069822 (accessed May 3, 2020).

[130] H.H. Kessler, S. Preininger, E. Stelzl, E. Daghofer, B.I. Santner, E. Marth, H. Lackner, R.E. Stauber, Identification of Different States of Hepatitis B Virus Infection with a Quantitative PCR Assay, 2000. http://cvi.asm.org/ (accessed May 3, 2020).

[131] J.M. Echevarría, A. Avellón, Hepatitis B virus genetic diversity, Journal of Medical Virology. 78 (2006). doi:10.1002/jmv.20605.

[132] S. Ghosh, P. Banerjee, P. Deny, R.K. Mondal, M. Nandi, A. Roychoudhury, K. Das, S. Banerjee, A. Santra, F. Zoulim, A. Chowdhury, S. Datta, New HBV subgenotype D9, a novel D/C recombinant, identified in patients with chronic HBeAg-negative infection in Eastern India, Journal of Viral Hepatitis. 20 (2013) 209–218. doi:10.1111/j.1365-2893.2012.01655.x.

[133] I.M. Mackay, K.E. Arden, A. Nitsche, Real-time PCR in virology, Nucleic Acids Research. 30(6)(2002) 1292–1305.

[134] S. Choi, Powering point-of-care diagnostic devices, Biotechnology Advances. 34 (2016) 321–330. doi:10.1016/j.biotechadv.2015.11.004.

[135] J. Song, M.G. Mauk, B.A. Hackett, S. Cherry, H.H. Bau, C. Liu, Instrument-Free Point-of-Care Molecular Detection of Zika Virus, Analytical Chemistry. 88 (2016)

7289–7294. doi:10.1021/acs.analchem.6b01632.

[136] D. Kim, Y. Kim, S. Hong, J. Kim, N. Heo, M.-K. Lee, S. Lee, B. Kim, I. Kim, Y. Huh, B. Choi, Development of Lateral Flow Assay Based on Size-Controlled Gold Nanoparticles for Detection of Hepatitis B Surface Antigen, Sensors. 16 (2016) 2154. doi:10.3390/s16122154.

[137] F.Y. Wu, Y.W. Liao, J.F. Wu, H.L. Chen, H.Y. Hsu, M.H. Chang, Y.H. Ni, A Simple and Rapid Test-card Method to Detect Hepatitis B Surface Antigen and Antibody: Potential Application in Young Children and Infants, Pediatrics and Neonatology. 57 (2016) 219–224. doi:10.1016/j.pedneo.2015.07.003.

[138] E. Seremba, P. Ocama, C.K. Opio, M. Kagimu, H.J. Yuan, N. Attar, D.L. Thomas, W.M. Lee, Validity of the rapid strip assay test for detecting HBsAg in patients admitted to hospital in Uganda, Journal of Medical Virology. 82 (2010) 1334–1340. doi:10.1002/jmv.21813.

[139] J.H. Ryu, M. Kwon, J.D. Moon, M.W. Hwang, J.M. Lee, K.H. Park, S.J. Yun, H.J. Bae, A. Choi, H. Lee, B. Jung, J. Jeong, K. Han, Y. Kim, E.J. Oh, Development of a rapid automated fluorescent lateral flow immunoassay to detect Hepatitis B surface antigen (HBsAg), antibody to HBsAg, and antibody to Hepatitis C, Annals of Laboratory Medicine. 38 (2018) 578–584. doi:10.3343/alm.2018.38.6.578.

[140] A.W. Gani, W. Wei, R.-Z. Shi, E. Ng, M. Nguyen, M.-S. Chua, S. So, S.X. Wang, An Automated, Quantitative, and Multiplexed Assay Suitable for point-of-care Hepatitis B Virus Diagnostics. Scientific Reports. 9 (2019) 15615. doi:10.1038/s41598-019-52147-z.

[141] L.W. Song, Y. Bin Wang, L.L. Fang, Y. Wu, L. Yang, J.Y. Chen, S.X. Ge, J. Zhang, Y.Z. Xiong, X.M. Deng, X.P. Min, J. Zhang, P.J. Chen, Q. Yuan, N.S. Xia, Rapid fluorescent lateral-flow immunoassay for hepatitis B virus genotyping, Analytical Chemistry. 87 (2015) 5173–5180. doi:10.1021/ac504832c.

[142] C. Fda, Guidance for Industry: Adequate and Appropriate Donor Screening Tests for Hepatitis B; Hepatitis B Surface Antigen (HBsAg) Assays Used to Test Donors of Whole Blood and Blood Components, Including Source Plasma and Source Leukocytes, 2007. http:www.fda.gov/cber/guidelines.htm. (accessed May 5, 2020).

[143] Y. Yazdani, A. Roohi, J. Khoshnoodi, F. Shokri, Development of a sensitive enzyme-linked immunosorbent assay for detection of hepatitis B surface antigen using novel monoclonal antibodies, Avicenna Journal of Medical Biotechnology. 2 (2010) 207–214.

[144] S. Lou, R. Taylor, S. Pearce, M. Kuhns, T. Leary, An ultra-sensitive Abbott ARCHITECT ® assay for the detection of hepatitis B virus surface antigen (HBsAg),

Journal of Clinical Virology. 105 (2018) 18–25. doi:10.1016/j.jcv.2018.05.009.

[145] E Hadziyannis, Quantification of HBsAg in serum: characteristics of the assays. OA Hepatology, 1 (2013) 1. http://www.oapublishinglondon.com/article/395#.

[146] K.H. Shin, H.J. Lee, C.L. Chang, H.H. Kim, Performance of the cobas Hepatitis B virus (HBV) test using the cobas 4800 system and comparison of HBV DNA quantification ability between the COBAS AmpliPrep/COBAS TaqMan HBV test version 2.0 and cobas HBV test, Journal of Clinical Virology. 101 (2018) 47–51. doi:10.1016/j.jcv.2018.01.012.

[147] RealTime HBV Viral Load Assay | Abbott Molecular, (n.d.). https://www.molecular.abbott/us/en/products/infectious-disease/realtime-hbv-viral-load (accessed May 4, 2020).

[148] Y. Shen, G. Shen, Signal-Enhanced Lateral Flow Immunoassay with Dual Gold Nanoparticle Conjugates for the Detection of Hepatitis B Surface Antigen, ACS Omega 4 (3) (2019) 5083–5087. doi:10.1021/acsomega.8b03593.

[149] C. Yu, J. Irudayaraj, Multiplex biosensor using gold nanorods, Analytical Chemistry. 79 (2007) 572–579. doi:10.1021/ac061730d.

[150] P.P. Joshi, S.J. Yoon, W.G. Hardin, S. Emelianov, K. V. Sokolov, Conjugation of antibodies to gold nanorods through fc portion: Synthesis and molecular specific imaging, Bioconjugate Chemistry. 24 (2013) 878–888. doi:10.1021/bc3004815.

[151] Z. Grabarek, J. Gergely, Zero-length crosslinking procedure with the use of active esters, Analytical Biochemistry. 185 (1990) 131–135. doi:10.1016/0003-2697(90)90267-D.

[152] K.M. Slagle, S.J. Ghosn, Immunoassays: Tools for Sensitive, Specific, and Accurate Test Results, Laboratory Medicine. 27 (1996) 177–183. doi:10.1093/labmed/27.3.177.

[153] T.A. Little, Method validation essentials, limit of blank, limit of detection, and limit of quantitation: Care needs to be made to match the method of limit determination to the analytical method, BioPharm International. 28 (2015) 48–51.

[154] A. Shrivastava, V. Gupta, Methods for the determination of limit of detection and limit of quantitation of the analytical methods, Chronicles og Young Scientists. 2 (2011) 21–25. doi:10.4103/2229-5186.79345.

[155] A. Niemz, T.M. Ferguson, D.S. Boyle, Point-of-care nucleic acid testing for infectious diseases, Trends in Biotechnology. 29 (2011) 240–250. doi:10.1016/j.tibtech.2011.01.007.

[156] M. Grasso, P. Piscopo, A. Confaloni, M. Denti, Circulating miRNAs as Biomarkers for Neurodegenerative Disorders, Molecules. 19 (2014) 6891–6910. doi:10.3390/molecules19056891.

[157] T. Gilboa, P.M. Garden, L. Cohen, Single-molecule analysis of nucleic acid biomarkers – A review, Analytica Chimica Acta. 1115 (2020) 61–85. doi:10.1016/j.aca.2020.03.001.

[158] N. Akkilic, S. Geschwindner, F. Höök, Single-molecule biosensors: Recent advances and applications, Biosensors & Bioelectronics. 151 (2020) 111944. doi:10.1016/j.bios.2019.111944.

[159] J.P. Jakupciak, W. Wang, M.E. Markowitz, D. Ally, M. Coble, S. Srivastava, A. Maitra, P.E. Barker, D. Sidransky, C.D. O'Connell, Mitochondrial DNA as a cancer biomarker, Journal of Molecular Diagnostics. 7 (2005) 258–267. doi:10.1016/S1525-1578(10)60553-3.

[160] A. Ziegler, A. Koch, K. Krockenberger, A. Großhennig, Personalized medicine using DNA biomarkers: A review, Human Genetics. 131 (2012) 1627–1638. doi:10.1007/s00439-012-1188-9.

[161] G. Johansson, D. Andersson, S. Filges, J. Li, A. Muth, T.E. Godfrey, A. Ståhlberg, Considerations and quality controls when analyzing cell-free tumor DNA, Biomolecular Detection and Quantification. 17 (2019) 100078. doi:10.1016/j.bdq.2018.12.003.

[162] Y.C.T. Yang, C. Di, B. Hu, M. Zhou, Y. Liu, N. Song, Y. Li, J. Umetsu, J.J. Lu, CLIPdb: A CLIP-seq database for protein-RNA interactions, BMC Genomics. 16 (2015) 51. doi:10.1186/s12864-015-1273-2.

[163] A.A. Alshatwi, G. Shafi, T.N. Hasan, N.A. Syed, A.A. Al-Hazzani, M.A. Alsaif, A.A. Alsaif, Differential Expression Profile and Genetic Variants of MicroRNAs Sequences in Breast Cancer Patients, PLoS One. 7 (2012) e30049. doi:10.1371/journal.pone.0030049.

[164] K. Munkholm, M. Vinberg, M. Berk, L.V. Kessing, State-related alterations of gene expression in bipolar disorder: A systematic review, Bipolar Disorders. 14 (2012) 684–696. doi:10.1111/bdi.12005.

[165] A. Schmid, H. Kortmann, P.S. Dittrich, L.M. Blank, Chemical and biological single cell analysis, Current Opinion in Biotechnology. 21 (2010) 12–20. doi:10.1016/j.copbio.2010.01.007.

[166] Z. Williams, I.Z. Ben-Dov, R. Elias, A. Mihailovic, M. Brown, Z. Rosenwaks, T. Tuschl, Comprehensive profiling of circulating microRNA via small RNA

sequencing of cDNA libraries reveals biomarker potential and limitations, Proceedings of the National Academy of Sciences of the United States of America. 110 (2013) 4255–4260. doi:10.1073/pnas.1214046110.

[167] X. Xi, T. Li, Y. Huang, J. Sun, Y. Zhu, Y. Yang, Z.J. Lu, RNA biomarkers: Frontier of precision medicine for cancer, Non-Coding RNA. 3 (2017). doi:10.3390/ncrna3010009.

[168] M.L. Metzker, Sequencing technologies the next generation, Nature Reviews. Genetics. 11 (2010) 31–46. doi:10.1038/nrg2626.

[169] J. Shendure, H. Ji, Next-generation DNA sequencing, Nature Biotechnology. 26 (2008) 1135–1145. doi:10.1038/nbt1486.

[170] E.R. Mardis, R.K. Wilson, Cancer genome sequencing: a review, Human Molecular Genetics. 18 (2009) R163--R168. doi:10.1093/hmg/ddp396.

[171] S. Behjati, P.S. Tarpey, What is next generation sequencing? Archives of Disease in Childhood. Education and Practice Edition. 98 (2013) 236–238. doi:10.1136/archdischild-2013-304340.

[172] L. Dubeau, L.A. Chandler, J.R. Gralow, P.W. Nichols, P.A. Jones, Southern Blot Analysis of DNA Extracted from Formalin-Fixed Pathology Specimens, Cancer Research 46 (1986) 2964–2969.

[173] G.S. Pall, A.J. Hamilton, Improved northern blot method for enhanced detection of small RNA, Nature Protocols. 3 (2008) 1077–1084. doi:10.1038/nprot.2008.67.

[174] O. Sheils, S. Finn, J. O'Leary, Nucleic acid microarrays: An overview. Diagnostic Histopathology. 9 (2003), 155–158. doi:10.1016/S0968-6053(02)00095-9.

[175] A.S. Devonshire, R. Sanders, T.M. Wilkes, M.S. Taylor, C.A. Foy, J.F. Huggett, Application of next generation qPCR and sequencing platforms to mRNA biomarker analysis, Methods. 59 (2013) 89–100. doi:10.1016/j.ymeth.2012.07.021.

[176] M.W. Pfaffl, Quantification strategies in real-time PCR, In: S.A. Bustin (Ed.), A-Z of Quantitative PCR, International University Line (IUL), La Jolla, CA USA, 2004: pp. 87–112.

[177] M.A. Cortez, G.A. Calin, MicroRNA identification in plasma and serum: A new tool to diagnose and monitor diseases, Expert Opinion on Biological Therapy. 9 (2009) 703–711. doi:10.1517/14712590902932889.

[178] R.C. Lee, R.L. Feinbaum, V. Ambros, The C. elegans heterochronic gene lin-4 encodes small RNAs with antisense complementarity to lin-14, Cell. 75 (1993) 843–

854. doi:10.1016/0092-8674(93)90529-Y.

[179] miRBase, (n.d.). http://www.mirbase.org/summary.shtml?org=hsa (accessed May 13, 2020).

[180] A. Kozomara, M. Birgaoanu, S. Griffiths-Jones, miRBase: from microRNA sequences to function, Nucleic Acids Research. 47 (2018) 155–162. doi:10.1093/nar/gky1141.

[181] G. Swaminathan, J. Martin-Garcia, S. Navas-Martin, RNA viruses and microRNAs: Challenging discoveries for the 21st century, Physiological Genomics. 45 (2013) 1035–1048. doi:10.1152/physiolgenomics.00112.2013.

[182] J. Lim, J. Byun, K. Guk, S. Gee Hwang, P. Kee Bae, J. Jung, T. Kang, E.-K. Lim, Highly Sensitive in Vitro Diagnostic System of Pandemic Influenza A (H1N1) Virus Infection with Specific MicroRNA as a Biomarker, ACS Omega 4 (11) (2019) 14560–14568. doi:10.1021/acsomega.9b01790.

[183] P.T. Liu, M. Wheelwright, R. Teles, E. Komisopoulou, K. Edfeldt, B. Ferguson, M.D. Mehta, A. Vazirnia, T.H. Rea, E.N. Sarno, T.G. Graeber, R.L. Modlin, MicroRNA-21 targets the vitamin D-dependent antimicrobial pathway in leprosy, Nature Medicine. 18 (2012) 267–273. doi:10.1038/nm.2584.

[184] Y. Cheng, C. Zhang, MicroRNA-21 in cardiovascular disease, Journal of Cardiovascular Translational Research. 3 (2010) 251–255. doi:10.1007/s12265-010-9169-7.

[185] N. Yanaihara, N. Caplen, E. Bowman, M. Seike, K. Kumamoto, M. Yi, R.M. Stephens, A. Okamoto, J. Yokota, T. Tanaka, G.A. Calin, C.G. Liu, C.M. Croce, C.C. Harris, Unique microRNA molecular profiles in lung cancer diagnosis and prognosis, Cancer Cell. 9 (2006) 189–198. doi:10.1016/j.ccr.2006.01.025.

[186] U. Bissels, S. Wild, S. Tomiuk, A. Holste, M. Hafner, T. Tuschl, A. Bosio, Absolute quantification of microRNAs by using a universal reference, RNA. 15 (2009) 2375–2384. doi:10.1261/rna.1754109.

[187] X. Pan, R. Wang, Z.X. Wang, The potential role of miR-451 in cancer diagnosis, prognosis, and therapy, Molecular Cancer Therapeutics. 12 (2013) 1153–1162. doi:10.1158/1535-7163.MCT-12-0802.

[188] M. Haneklaus, M. Gerlic, L.A.J. O'Neill, S.L. Masters, MiR-223: Infection, inflammation and cancer, Journal of Internal Medicine. 274 (2013) 215–226. doi:10.1111/joim.12099.

[189] X. Zhang, M.R. Servos, J. Liu, Instantaneous and quantitative functionalization of

gold nanoparticles with thiolated DNA using a pH-assisted and surfactant-free route, Journal of the American Chemical Society. 134 (2012) 7266–7269. doi:10.1021/ja3014055.

[190] H.D. Hill, C.A. Mirkin, The bio-barcode assay for the detection of protein and nucleic acid targets using DTT-induced ligand exchange, Nature Protocols. 1 (2006) 324–336. doi:10.1038/nprot.2006.51.

[191] X.-B. Wan, A.-Q. Wang, J. Cao, Z.-C. Dong, N. Li, S. Yang, M.-M. Sun, Z. Li, S.-X. Luo, Relationships among KRAS mutation status, expression of RAS pathway signaling molecules, and clinicopathological features and prognosis of patients with colorectal cancer. World Journal of Gastroenterology. 25 (7) (2010 808–823. doi:10.3748/wjg.v25.i7.808.

[192] A. Walther, E. Johnstone, C. Swanton, R. Midgley, I. Tomlinson, D. Kerr, Genetic prognostic and predictive markers in colorectal cancer, Nature Reviews. Cancer. 9 (2009) 489–499. doi:10.1038/nrc2645.

[193] H.H. Yoon, D. Tougeron, Q. Shi, S.R. Alberts, M.R. Mahoney, G.D. Nelson, S.G. Nair, S.N. Thibodeau, R.M. Goldberg, D.J. Sargent, F.A. Sinicrope, KRAS codon 12 and 13 mutations in relation to disease-free survival in BRAF-wild-type stage III colon cancers from an adjuvant chemotherapy trial (N0147 alliance), Clinical Cancer Research. 20 (2014) 3033–3043. doi:10.1158/1078-0432.CCR-13-3140.

[194] F. Molinari, L. Felicioni, M. Buscarino, S. De Dosso, F. Buttitta, S. Malatesta, A. Movilia, M. Luoni, R. Boldorini, O. Alabiso, S. Girlando, B. Soini, A. Spitale, F. Di Nicolantonio, P. Saletti, S. Crippa, L. Mazzucchelli, A. Marchetti, A. Bardelli, M. Frattini, Increased detection sensitivity for KRAS mutations enhances the prediction of anti-EGFR monoclonal antibody resistance in metastatic colorectal cancer, Clinical Cancer Research. 17 (2011) 4901–4914. doi:10.1158/1078-0432.CCR-10-3137.

[195] H.M. Chiu, L.C. Chang, W.F. Hsu, C.K. Chou, M.S. Wu, Non-invasive screening for colorectal cancer in Asia, Best Practice & Research. Clinical Gastroenterology. 29 (2015) 953–965. doi:10.1016/j.bpg.2015.09.015.

[196] Y. Imamura, T. Morikawa, X. Liao, P. Lochhead, A. Kuchiba, M. Yamauchi, Z.R. Qian, R. Nishihara, J.A. Meyerhardt, K.M. Haigis, C.S. Fuchs, S. Ogino, Specific mutations in KRAS codons 12 and 13, and patient prognosis in 1075 BRAF wild-type colorectal cancers, Clinical Cancer Research. 18 (2012) 4753–4763. doi:10.1158/1078-0432.CCR-11-3210.

[197] L. Simi, N. Pratesi, M. Vignoli, R. Sestini, F. Cianchi, R. Valanzano, S. Nobili, E. Mini, M. Pazzagli, C. Orlando, High-resolution melting analysis for rapid detection of KRAS, BRAF, and PIK3CA gene mutations in colorectal cancer, American

Journal of Clinical Pathology. 130 (2008) 247–253. doi:10.1309/LWDY1AXHXUULNVHQ.

[198] S. Lee, V.H. Brophy, J. Cao, M. Velez, C. Hoeppner, S. Soviero, H.J. Lawrence, Analytical performance of a PCR assay for the detection of KRAS mutations (codons 12/13 and 61) in formalin-fixed paraffin-embedded tissue samples of colorectal carcinoma, Virchows Archiv. 460 (2012) 141–149. doi:10.1007/s00428-011-1180-0.

[199] C. Sun, S. Hobor, A. Bertotti, D. Zecchin, S. Huang, F. Galimi, F. Cottino, A. Prahallad, W. Grernrum, A. Tzani, A. Schlicker, L.F.A. Wessels, E.F. Smit, E. Thunnissen, P. Halonen, C. Lieftink, R.L. Beijersbergen, F. DiNicolantonio, A. Bardelli, L. Trusolino, R. Bernards, Intrinsic resistance to MEK inhibition in kras mutant lung and colon cancer through transcriptional induction of ERBB3, Cell Reports. 7 (2014) 86–93. doi:10.1016/j.celrep.2014.02.045.

[200] J.F. Huggett, S. Cowen, C.A. Foy, Considerations for digital PCR as an accurate molecular diagnostic tool, Clinical Chemistry. 61 (2015) 79–88. doi:10.1373/clinchem.2014.221366.

[201] E. Takai, Y. Totoki, H. Nakamura, C. Morizane, S. Nara, N. Hama, M. Suzuki, E. Furukawa, M. Kato, H. Hayashi, T. Kohno, H. Ueno, K. Shimada, T. Okusaka, H. Nakagama, T. Shibata, S. Yachida, Clinical utility of circulating tumor DNA for molecular assessment in pancreatic cancer, Scientific Reports. 5 (2015) 18425. doi:10.1038/srep18425.

[202] Galbiati, Damin, Ferraro, Soriani, Burgio, Ronzoni, Gianni, Ferrari, Chiari, Microarray Approach Combined with ddPCR: An Useful Pipeline for the Detection and Quantification of Circulating Tumour dna Mutations, Cells. 8 (2019) 769. doi:10.3390/cells8080769.

[203] D.D. Von Hoff, J.J. Stephenson, P. Rosen, D.M. Loesch, M.J. Borad, S. Anthony, G. Jameson, S. Brown, N. Cantafio, D.A. Richards, T.R. Fitch, E. Wasserman, C. Fernandez, S. Green, W. Sutherland, M. Bittner, A. Alarcon, D. Mallery, R. Penny, Pilot study using molecular profiling of patients' tumors to find potential targets and select treatments for their refractory cancers, Journal of Clinical Oncology. 28 (2010) 4877–4883. doi:10.1200/JCO.2009.26.5983.

[204] G.D. Sorenson, D.M. Pribish, F.H. Valone, V.A. Memoli, D.J. Bzik, S.L. Yao, Soluble normal and mutated DNA sequences from single-copy genes in human blood., Cancer Epidemiology, Biomarkers & Prevention. 3 (1994) 67–71.

[205] P.B. Gahan, R. Swaminathan, Circulating nucleic acids in plasma and serum: Recent developments, Annals of the New York Academy of Sciences, 1137 (2008) 1–6. doi:10.1196/annals.1448.050.

[206] J.-D. Luo, E.-C. Chan, C.-L. Shih, T.-L. Chen, Y. Liang, T.-L. Hwang, C.-C. Chiou, Detection of rare mutant K-ras DNA in a single-tube reaction using peptide nucleic acid as both PCR clamp and sensor probe, Nucleic Acids Research. 34 (2) (2006) e12. doi:10.1093/nar/gnj008.

[207] M.T. Lin, S.L. Mosier, M. Thiess, K.F. Beierl, M. Debeljak, L.H. Tseng, G. Chen, S. Yegnasubramanian, H. Ho, L. Cope, S.J. Wheelan, C.D. Gocke, J.R. Eshleman, Clinical validation of KRAS, BRAF, and EGFR mutation detection using next-generation sequencing, American Journal of Clinical Pathology. 141 (2014) 856–866. doi:10.1309/AJCPMWGWGO34EGOD.

[208] F. Damin, S. Galbiati, N. Soriani, V. Burgio, M. Ronzoni, M. Ferrari, M. Chiari, Analysis of KRAS, NRAS and BRAF mutational profile by combination of in-tube hybridization and universal tag-microarray in tumor tissue and plasma of colorectal cancer patients, PLoS One. 13 (2018) 1–15. doi:10.1371/journal.pone.0207876.

[209] F. Damin, S. Galbiati, M. Ferrari, M. Chiari, DNA microarray-based solid-phase PCR on copoly (DMA-NAS-MAPS) silicon coated slides: An example of relevant clinical application, Biosensors & Bioelectronics. 78 (2016) 367–373. doi:10.1016/j.bios.2015.11.091.

[210] M. V. Yezhelyev, X. Gao, Y. Xing, A. Al-Hajj, S. Nie, R.M. O'Regan, Emerging use of nanoparticles in diagnosis and treatment of breast cancer, The Lancet. Oncology. 7 (2006) 657–667. doi:10.1016/S1470-2045(06)70793-8.

[211] C.M. Somers, B.E. McCarry, F. Malek, J.S. Quinn, Reduction of Particulate Air Pollution Lowers the Risk of Heritable Mutations in Mice, Science. 304 (2004) 1008–1010. doi:10.1126/science.1095815.

[212] Y. Cao, J. Li, F. Liu, X. Li, Q. Jiang, S. Cheng, Y. Gu, Consideration of interaction between nanoparticles and food components for the safety assessment of nanoparticles following oral exposure: A review, Environmental Toxicology and Pharmacology. 46 (2016) 206–210. doi:10.1016/j.etap.2016.07.023.

[213] L. Luo, Z. Zhang, L. Hou, Development of a gold nanoparticles based chemiluminescence imaging assay and its application, Analytica Chimica Acta. 584 (2007) 106–111. doi:10.1016/j.aca.2006.10.047.

[214] R.W. Hendrix, M.C.M. Smith, R.N. Burns, M.E. Ford, G.F. Hatfull, Evolutionary relationships among diverse bacteriophages and prophages: All the world's a phage, Proceedings of the National Academy of Sciences of the United States of America. 96 (1999) 2192–2197. doi:10.1073/pnas.96.5.2192.

[215] C.A. Suttle, Viruses in the sea, Nature. 437 (2005) 356–361. doi:10.1038/nature04160.

[216] J.M. Mansuy, Mobile laboratories for Ebola and other pathogens, The Lancet. Infectious Diseases. 15 (2015) 1135. doi:10.1016/S1473-3099(15)00309-6.

[217] F. Kulzer, M. Orrit, Single-Molecule Optics, Annual Review of Physical Chemistry. 55 (2004) 585–611. doi:10.1146/annurev.physchem.54.011002.103816.

[218] W.E. Moerner, D.P. Fromm, Methods of single-molecule fluorescence spectroscopy and microscopy, Review of Scientific Instruments. 74 (2003) 3597–3619. doi:10.1063/1.1589587.

[219] E. Stern, R. Wagner, F.J. Sigworth, R. Breaker, T.M. Fahmy, M.A. Reed, Importance of the debye screening length on nanowire field effect transistor sensors, Nano Letters. 7 (2007) 3405–3409. doi:10.1021/nl071792z.

[220] F. Patolsky, G. Zheng, O. Hayden, M. Lakadamyali, X. Zhuang, C.M. Lieber, Electrical detection of single viruses, Proceedings of the National Academy of Sciences of the United States of America. 101 (2004) 14017–14022. doi:10.1073/pnas.0406159101.

[221] X.L. Luo, J.J. Xu, W. Zhao, H.Y. Chen, Glucose biosensor based on ENFET doped with SiO_2 nanoparticles, Sensors and Actuators B: Chemical. 97 (2–3) (2004) 249–255. doi:10.1016/j.snb.2003.08.024.

[222] W. Sant, M.L. Pourciel, J. Launay, T. Do Conto, A. Martinez, P. Temple-Boyer, Development of chemical field effect transistors for the detection of urea, Sensors and Actuators B: Chemical. 95 (2003) 309–314. doi:10.1016/S0925-4005(03)00430-1.

[223] M. Davidson, K. Kaufman, I. Mazor, F. Cohen, An Application Of Interference Microscopy To Integrated Circuit Inspection And Metrology, In: K.M. Monahan (Ed.), Proceedings of SPIE, vol. 775 Integrated Circuit Metrolology, Inspection, & Process Control, SPIE, 1987: p. 233. doi:10.1117/12.940433.

[224] V. Shpacovitch, V. Temchura, M. Matrosovich, J. Hamacher, J. Skolnik, P. Libuschewski, D. Siedhoff, F. Weichert, P. Marwedel, H. Müller, K. Überla, R. Hergenröder, A. Zybin, Application of surface plasmon resonance imaging technique for the detection of single spherical biological submicrometer particles, Analytical Biochemistry. 486 (2015) 62–69. doi:10.1016/j.ab.2015.06.022.

[225] S. Enoki, R. Iino, N. Morone, K. Kaihatsu, S. Sakakihara, N. Kato, H. Noji, Label-Free Single-Particle Imaging of the Influenza Virus by Objective-Type Total Internal Reflection Dark-Field Microscopy, PLoS One. 7 (2012) 1–7. doi:10.1371/journal.pone.0049208.

[226] S. Wang, X. Shan, U. Patel, X. Huang, J. Lu, J. Li, N. Tao, Label-free imaging,

detection, and mass measurement of single viruses by surface plasmon resonance, Proceedings of the National Academy of Sciences of the United States of America. 107 (2010) 16028–16032. doi:10.1073/pnas.1005264107.

[227] G. De Wit, J.S.H. Danial, P. Kukura, M.I. Wallace, Dynamic label-free imaging of lipid nanodomains, Proceedings of the National Academy of Sciences of the United States of America. 112 (2015) 12299–12303. doi:10.1073/pnas.1508483112.

[228] G.G. Daaboul, P. Gagni, L. Benussi, P. Bettotti, M. Ciani, M. Cretich, D.S. Freedman, R. Ghidoni, A.Y. Ozkumur, C. Piotto, D. Prosperi, B. Santini, M.S. Ünlü, M. Chiari, Digital Detection of Exosomes by Interferometric Imaging, Scientific Reports. 6 (2016). doi:10.1038/srep37246.

[229] S.M. Scherr, G.G. Daaboul, J. Trueb, D. Sevenler, H. Fawcett, B. Goldberg, J.H. Connor, M.S. Ünlü, Real-Time Capture and Visualization of Individual Viruses in Complex Media, ACS Nano. 10 (2016) 2827–2833. doi:10.1021/acsnano.5b07948.

[230] F. Vollmer, S. Arnold, Whispering-gallery-mode biosensing: Label-free detection down to single molecules, Nature Methods. 5 (2008) 591–596. doi:10.1038/nmeth.1221.

[231] H.K. Hunt, A.M. Armani, Bioconjugation strategies for label-free optical microcavity sensors, IEEE Journal of Selected Topics in Quantum Electronics. 20 (2014). doi:10.1109/JSTQE.2013.2272916.

[232] R. Méjard, H.J. Griesser, B. Thierry, Optical biosensing for label-free cellular studies, TrAC – Trends in Analytical Chemistry. 53 (2014) 178–186. doi:10.1016/j.trac.2013.08.012.

[233] M.C. Estevez, M.A. Otte, B. Sepulveda, L.M. Lechuga, Trends and challenges of refractometric nanoplasmonic biosensors: A review, Analytica Chimica Acta. 806 (2014) 55–73. doi:10.1016/j.aca.2013.10.048.

[234] S. Scarano, C. Scuffi, M. Mascini, M. Minunni, Surface plasmon resonance imaging (SPRi)-based sensing: A new approach in signal sampling and management, Biosensors & Bioelectronics 26 (2010) 1380–1385. doi:10.1016/j.bios.2010.07.056.

[235] M. Piliarik, J. Homola, Surface plasmon resonance (SPR) sensors: approaching their limits? Optics Express. 17 (2009) 16505. doi:10.1364/oe.17.016505.

[236] M.A. Eddings, J.W. Eckman, C.A. Arana, G.A. Papalia, J.E. Connolly, B.K. Gale, D.G. Myszka, “Spot and hop”: Internal referencing for surface plasmon resonance imaging using a three-dimensional microfluidic flow cell array, Analytical Biochemistry 385 (2009) 309–313. doi:10.1016/j.ab.2008.11.014.

[237] J. Liu, M.A. Eddings, A.R. Miles, R. Bukasov, B.K. Gale, J.S. Shumaker-Parry, In situ microarray fabrication and analysis using a microfluidic flow cell array integrated with surface plasmon resonance microscopy, Analytical Chemistry. 81 (2009) 4296–4301. doi:10.1021/ac900181f.

[238] E. Ouellet, C. Lausted, T. Lin, C.W.T. Yang, L. Hood, E.T. Lagally, Parallel microfluidic surface plasmon resonance imaging arrays, Lab on a Chip. 10 (2010) 581–588. doi:10.1039/b920589f.

[239] J.G. Quinn, S. O'Neill, A. Doyle, C. McAtamney, D. Diamond, B.D. MacCraith, R. O'Kennedy, Development and application of surface plasmon resonance-based biosensors for the detection of cell-ligand interactions, Analytical Biochemistry. 281 (2000) 135–143. doi:10.1006/abio.2000.4564.

[240] B. Rothenhäusler, W. Knoll, Surface-plasmon microscopy, Nature. 332 (1988) 615–617. doi:10.1038/332615a0.

[241] A. Zybin, V. Shpacovitch, J. Skolnik, R. Hergenröder, Optimal conditions for SPR-imaging of nano-objects, Sensors and Actuators, B: Chemical. 239 (2017) 338–342. doi:10.1016/j.snb.2016.07.124.

[242] H. Ueno, S. Nishikawa, R. Iino, K. V. Tabata, S. Sakakihara, T. Yanagida, H. Noji, Simple dark-field microscopy with nanometer spatial precision and microsecond temporal resolution, Biophysical Journal 98 (2010) 2014–2023. doi:10.1016/j.bpj.2010.01.011.

[243] F. Thoma, U. Langbein, S. Mittler-Neher, Waveguide scattering microscopy, Optics Communications. 134 (1997) 16–20. doi:10.1016/S0030-4018(96)00535-4.

[244] S. Ramachandran, D.A. Cohen, A.P. Quist, R. Lal, High performance, LED powered, waveguide based total internal reflection microscopy, Scientific Reports. 3 (2013) 2133. doi:10.1038/srep02133.

[245] B. Agnarsson, S. Ingthorsson, T. Gudjonsson, K. Leosson, Evanescent-wave fluorescence microscopy using symmetric planar waveguides, Optics Express. 17 (2009) 5075. doi:10.1364/oe.17.005075.

[246] B. Agnarsson, A. Lundgren, A. Gunnarsson, M. Rabe, A. Kunze, M. Mapar, L. Simonsson, M. Bally, V.P. Zhdanov, F. Höök, Evanescent Light-Scattering Microscopy for Label-Free Interfacial Imaging: From Single Sub-100 nm Vesicles to Live Cells, ACS Nano. 9 (2015) 11849–11862. doi:10.1021/acsnano.5b04168.

[247] L. Feuz, P. JÖnsson, M.P. Jonsson, F. HÖÖk, Improving the limit of detection of nanoscale sensors by directed binding to high-sensitivity areas, ACS Nano. 4 (2010) 2167–2177. doi:10.1021/nn901457f.

[248] G.G. Daaboul, C.A. Lopez, J. Chinnala, B.B. Goldberg, J.H. Connor, M. Selim Ünlü, Digital sensing and sizing of vesicular stomatitis virus pseudotypes in complex media: A model for ebola and marburg detection, ACS Nano. 8 (2014) 6047–6055. doi:10.1021/nn501312q.

[249] N.L. Ünlü, F.E. Kanik, E. Seymour, J.H. Connor, M.S. Ünlü, DNA-directed antibody immobilization for robust protein microarrays: Application to single particle detection 'DNA-directed antibody immobilization, In: Rasooly A., Prickril B. (eds.) Biosensors and Biodetection. Methods in Molecular Biology, vol. 1571. Humana Press, New York, NY. pp. 187–206. doi:10.1007/978-1-4939-6848-0_12.

[250] H. Ewers, V. Jacobsen, E. Klotzsch, A.E. Smith, A. Helenius, V. Sandoghdar, Label-free optical detection and tracking of single virions bound to their receptors in supported membrane bilayers, Nano Letters. 7 (2007) 2263–2266. doi:10.1021/nl070766y.

[251] J. Zhu, S.K. Ozdemir, Y.F. Xiao, L. Li, L. He, D.R. Chen, L. Yang, On-chip single nanoparticle detection and sizing by mode splitting in an ultrahigh-Q microresonator, Nature Photonics. 4 (2010) 46–49. doi:10.1038/nphoton.2009.237.

[252] A. Gupta, D. Akin, R. Bashir, Single virus particle mass detection using microresonators with nanoscale thickness, Applied Physics Letters. 84 (2004) 1976–1978. doi:10.1063/1.1667011.

[253] N.P. Wells, G.A. Lessard, P.M. Goodwin, M.E. Phipps, P.J. Cutler, D.S. Lidke, B.S. Wilson, J.H. Werner, Time-resolved three-dimensional molecular tracking in live cells, Nano Letters. 10 (2010) 4732–4737. doi:10.1021/nl103247v.

[254] T. Lu, H. Lee, T. Chen, S. Herchak, J.H. Kim, S.E. Fraser, R.C. Flagan, K. Vahala, High sensitivity nanoparticle detection using optical microcavities, Proceedings of the National Academy of Sciences of the United States of America. 108 (2011) 5976–5979. doi:10.1073/pnas.1017962108.

[255] Y. Zhi, X.-C. Yu, Q. Gong, L. Yang, Y.-F. Xiao, Single Nanoparticle Detection Using Optical Microcavities, Advanced Materials. 29 (2017) 1604920. doi:10.1002/adma.201604920.

[256] O. Avci, M.I. Campana, C. Yurdakul, M. Selim Ünlü, Pupil function engineering for enhanced nanoparticle visibility in wide-field interferometric microscopy, Optica. 4 (2017) 247. doi:10.1364/optica.4.000247.

9 CURRICULUM VITAE